

Elena Serebryakova

High-Power Comb-Line Filter Architectures for Switched-Mode RF Power Amplifier Systems

Dissertation

zur Erlangung des akademischen Grades

Doktoringenieur (Dr.-Ing.)

vorgelegt der Fakultät für Elektrotechnik und
Informationstechnik der Technischen Universität Ilmenau

von M.Sc. Elena Serebryakova,
geboren am 19. Januar 1984 in Atyrau, Kasachstan

vorgelegt am: 22.04.2012

Gutachter: Prof. Dr. rer. nat. habil. Matthias A. Hein (Betreuer)

Prof. Irina B. Vendik

Prof. Dr.-Ing. Georg Fischer

Verteidigung am: 25.10.2012

Verf.-Nr.: EI

urn:nbn:de:gbv:ilm1-2012000478

To Kurt

Acknowledgements

The present work is a part of the research project "HF-Modulator für Klasse-S-Verstärker: Signalbereitstellung im Zeit- und Frequenzbereich" (HMoS). The project and thus my position at the RF and Microwave Research Laboratory of the Ilmenau University of Technology were funded by the German Ministry of Education and Research within the class-S consortium of the focus program "Mobile-GaN" (Grant 01BU0603), for which I am very grateful: also for the contact it brought me with the partners in the Mobile-GaN project: EADS Deutschland GmbH, Alcatel-Lucent Deutschland AG, Ferdinand-Braun-Institut Leibniz-Institut für Höchstfrequenztechnik (FBH), Fraunhofer Institute Applied Solid-State Physics (IAF) and IHP GmbH in Frankfurt/Oder.

I thank the head of the laboratory, Prof. M. A. Hein, for the opportunity to work under his supervision and for his watchful eye over our group.

I am thankful to Dr. K. Blau for so many things: the regular scientific discussion, the non-stop encouragement, the constant availability and the warm friendship he has given to me and everybody in the group.

Thank you also, very sincerely, to: Prof. I. Vendik and Prof. G. Fischer for reviewing my thesis; my fellow-researcher Dipl.-Ing. Ch. Hartmann for fruitful discussions during the project; Dr. K. Blau, Mrs. S. Kubitz and Dr. J. Trabert for proofreading of my thesis; all the rest of my colleagues for the pleasant work climate.

I thank my family for their understanding and encouragement, especially over the last six years.

Elena Serebryakova,
Ilmenau, 7th May 2013

Abstract

This work has taken place in the context that a class-S power amplifier system with simplified transmitter architectures and increased power efficiency makes an attractive candidate for cellular phone base transceiver station applications [1].

The author describes the requirements for, and a number of successful implementations of, a reconstruction filter suitable for such an amplifier system. In a current-mode class-S power amplifier system, crucial to the maintenance of the rectangular shape of the drain current and thus to high efficiency are not only the tailoring of pass-band and stop-band, but also the specification of input impedance for different modes of excitation over a wide frequency range. Doubly and singly terminated filters are subjected to theoretical consideration, simulation, testing and measurement. The main focus of the research is on the design of the reconstruction filter.

It is found that the electrical and geometrical constraints for the design of a reconstruction filter are well satisfied by balanced input comb-line filters. Several filter architectures are proposed, experimentally investigated, and critically analysed in terms of differential and common mode impedances. This is the first complete analysis of reconstruction filters for current mode class-S power amplifier systems, as far as the author knows. Switched-mode power amplifier systems which include the proposed filters are also simulated and measured under different driving conditions. The maximum power efficiency of 65% to date in the switched-mode power amplifier systems can be attributed to the successful filter design.

Zusammenfassung

Die vorgelegte Arbeit behandelt die Analyse der Anforderungen, den schaltungstechnischen Entwurf, den Aufbau und die messtechnische Verifizierung von Rekonstruktionsfiltern für Leistungsschaltverstärker im Klasse-S Betrieb, die auf Grund ihres hohen Wirkungsgrades vorzugsweise in Mobilfunkbasisstationen Verwendung finden sollen. Die Brauchbarkeit des Entwurfes wird an Hand einer Reihe von Applikationsbeispielen anschaulich dargestellt.

Als Kernforderung einer derartigen Filterauslegung hat sich die Aufrechterhaltung der Rechteckzeitfunktion des Drain-Stromes für einen (im "Current Mode" arbeitenden) Schaltverstärker herausgestellt, weil sonst die damit erzielbare hohe Effizienz nicht erreicht werden kann. Darüber hinaus fließen in die Filterauslegung nicht nur die Fixierung des Filterdurchlass- und sperrbereiches ein, sondern auch die Festlegung der Eingangs- und Lastimpedanz bei unterschiedlichen Anregungsmoden über einen breiten Frequenzbereich. Doppel- und einzelterminierte Filter werden theoretisch betrachtet, simuliert, getestet und gemessen.

Es wurde herausgearbeitet, dass die schaltungstechnischen und geometrischen Anforderungen an einen derartigen Rekonstruktionsfilterentwurf gut durch symmetrisch gespeiste Kammlenitungsfilter erfüllt werden können. Verschiedene Filterarchitekturen werden im Hinblick auf ihr Gleich- und Gegentaktimpedanzverhalten vorgestellt, experimentell untersucht und kritisch analysiert. Soweit dem Autor bekannt ist, werden hier erstmalig Rekonstruktionsfilter für Klasse-S Leistungsverstärker im "Current Mode" komplett analysiert. Desweiteren wird die Funktionalität des Rekonstruktionsfilters an Hand anderer Typen von Leistungsschaltverstärkern simuliert und messtechnisch untersucht. Der maximale Wirkungsgrad von 65% bei Leistungsschaltverstärkersystemen lässt sich dem erfolgreichen Filterentwurf zuschreiben.

Contents

1	Introduction	1
1.1	State of the art of mobile communications	1
1.2	Green mobile communication	3
1.3	The class-S power amplifier as a highly efficient alternative	4
1.4	Organisation of the Dissertation	6
2	Class-S power amplifier systems	8
2.1	RF power amplifiers principles from class-A to class-S	8
2.2	State of the art of class-S power amplifiers	11
2.3	Architecture of class-S power amplifiers	13
2.3.1	Switching amplifiers	14
2.3.2	RF one-bit modulators	19
2.3.3	Reconstruction filters	23
2.4	Conclusion of the class-S power amplifier system concept	25
3	Requirements for reconstruction filters	27
3.1	Requirements for transmitter filters for wireless base stations	27
3.2	Input impedances for different excitation modes	29
3.3	Filter terminations	34
3.4	Singly terminated filters	43
3.4.1	Computation and measurement techniques	43
3.4.2	Impedance transformation	46
3.5	Specifications for a reconstruction filter	49
3.6	Conclusion of the requirements for reconstruction filters	49

4	Design and implementation of reconstruction filters	52
4.1	Filter technologies for wireless base stations	52
4.2	Coaxial comb-line filter design	55
4.2.1	Quality factor, transfer function and filter order	56
4.2.2	Simulation results	59
4.2.3	Measurement results	61
4.2.4	Frequency tunability	63
4.2.5	High power handling capability	65
4.3	Balanced input comb-line filter design	71
4.3.1	Architecture with a straight loop	71
4.3.2	Design with a pulse shaping network	78
4.3.3	Filters with an electrically-long input loop	83
4.3.4	Alternative design with an electrically-short input loop	92
4.4	Conclusion of the design and implementation of reconstruction filters	96
5	Influence of the reconstruction filter on the power amplifier performance	98
5.1	Simulation of reconstruction filters in class-D RF PA systems	98
5.1.1	Simulation engines in ADS software	99
5.1.2	Transistor model	99
5.1.3	Power characteristics	100
5.1.4	Impact of parasitic components in the GaN HEMTs	103
5.1.5	Effect of parasitic components in the filter	105
5.1.6	Influence of the filter termination	108
5.2	Simulation of reconstruction filters in class-S PA systems	109
5.2.1	Class-S system with a pulse-length modulator	111
5.2.2	Class-S system using a delta-sigma modulator	114
5.3	Overview of class-S demonstrators	116
5.3.1	Demonstrator for the TETRA frequency band	117
5.3.2	Demonstrators for the GSM frequency band	118
5.4	Measurement results	121

5.4.1	Demonstrator for the TETRA frequency band	122
5.4.2	Demonstrators for the GSM frequency band	123
5.5	Conclusion regarding implementation of switched-mode power amplifiers	128
6	Conclusions	130
	Publications	A
	Bibliography	C
	List of Symbols and Acronyms	Q

List of Figures

1.1.1	Evolution in data transmission rate [2].	1
2.3.1	Basic building blocks of a class-S PA system: a one-bit modulator, a switching amplifier and a reconstruction filter. Time signals (red curves) and spectra (blue curves) are shown at each building block.	14
2.3.2	Current-mode class-S PA system comprising a $\Delta\Sigma\text{M}$ or PLM, a push-pull transistor amplifier with biasing network (RF chokes L_{ch} and voltage supply V_{cc}), a parallel resonant circuit (L and C), and a load resistance R_l	15
2.3.3	Waveforms of drain currents (red curves) and drain voltages (blue curves) in a current-mode class-S PA system when driven by a PLM. The ADS simulation was carried out under the following conditions: $V_{cc} = 17.5$ V, $R_{dsON} = 3$ Ohms, $R_{lOpt class-S} = 65$ Ohms.	16
2.3.4	General topology (in panel a) and typical simulated power spectral density (in panel b) of a $\Delta\Sigma\text{M}$ [3].	20
2.3.5	Photograph of the $\Delta\Sigma\text{M}$ chip (in panel a) and the measured output spectrum (in panel b) [4] (Source: IHP GmbH in Frankfurt/Oder, Germany).	21
2.3.6	General topology (in panel a) and typical power spectral density (in panel b) of a PLM [5].	23

3.1.1	Illustrative diagram of spectrum emission mask for different classes of the UMTS BTSs defined by a level of output power of 31 dBm, 39 dBm and 43 dBm [6] where Δf_{max} is 12.5 MHz. . .	28
3.2.1	A CMCS PA including a second-order balanced input BPF. The differential port 2 can be excited in differential mode (orange curves) and in common mode of excitation (blue curves).	30
3.2.2	Definition of differential-mode and common-mode impedances [7].	31
3.3.1	Doubly and singly terminated filter structures. E_g denotes the electromotive force of the generator, e_i and i_i are the corresponding node potentials and currents, and y_i and z_i are the partial immittances of a reactive ladder network [8].	34
3.3.2	Input resistance (red curves), its first derivative as computed (blue solid curves) and as analytically derived (blue dotted curves) for a 4 th -order ST Butterworth filter.	40
3.3.3	Input impedance (red curves), its first derivative as computed (blue solid curves) and as analytically derived (blue dotted curves) for a 4 th -order DT Butterworth filter (in panel a) and a 5 th -order DT Chebyshev filter (in panel b).	42
3.4.1	Third-order ST and DT BPFs with admittance inverters.	43
3.4.2	Input resistances (in panel a) and reflection coefficients for a differential mode of excitation (in panel b) of the Butterworth third-order DT (blue curves) and ST filters (red curves). The filters on ideal elements are traced by solid lines, on real elements - by dotted lines. The frequencies marked on the Smith Chart are $f_1^{ST} = 0.915$ GHz, $f_2^{ST} = 0.885$ GHz, $f_1^{DT} = 0.917$ GHz, and $f_2^{DT} = 0.883$ GHz	45

3.4.3	Transmission coefficient of the third-order DT filter (blue curves) and ST filter (red lines) excited by a current source with a source resistance of $R_g = 50 \Omega$. The filters based on ideal elements are represented by solid curves and on real elements (including losses) by dotted curves.	45
3.4.4	The input resistance (in panel a) and transmission coefficient (in panel b) of the Butterworth ST filters with impedance transformation ratios of $r = 10$ (blue line), $\frac{1}{2}$ (green line) and $\frac{1}{20}$ (red line).	49
4.1.1	Photo of the 4-pole filter with two dielectric dual-mode resonators (in panel a) and measured spurious performance (in panel b) [9].	53
4.1.2	The third-order filter on metamaterials (in panel a) [10] and the duplex comb-line filter supplied by Alcatel-Lucent (in panel b) [11].	54
4.2.1	Schematic layout of a comb-line band-pass filter in stripline form [12].	55
4.2.2	Insertion loss as a function of the filter order for the DT filters (blue curves) and ST filters (red curves). The calculation with the Q-factor as computed is shown by solid lines and with the Q-factor as measured by dash lines.	58
4.2.3	ADS simulation results: input resistance (in panel a) and reflection coefficient (in panel b) of the third-order Butterworth DT CLF (blue curves) and the ST CLF (red curves).	60
4.2.4	ADS simulation results: reflection coefficients of third-order microstrip ST CLFs with impedance transformation ratios of 2 (red), 1 (blue) and $\frac{1}{2}$ (purple).	61
4.2.5	Layout of third-order ST microstrip CLFs with impedance transformation ratios of 2, 1 and $\frac{1}{2}$	62

4.2.6	Photograph (in panel a) and the measurement results (in panel b) of the coaxial third-order DT CLF. The inset shows the input resistance in-band.	63
4.2.7	Pass-bands of the mechanically tunable CLF for different tuning states (in panel a) and tuning functions (the frequency dependence of number of turns as a function of frequency) for the CLF resonators (in panel b).	65
4.2.8	Influence of the transmission line impedance of the distributed capacitance at the end of resonators on the coefficient $\chi(Z_{EC})$	68
4.2.9	Sketch of the CLF, laid out for high power handling (in panel a) and measured transmission coefficient (in panel b).	68
4.2.10	Measurement test setup including a signal generator, a power amplifier, a CLF, calibrated power meters, a high-power directional coupler, cables, a high-power load and a network analyser.	69
4.2.11	Results of the high-power measurements: blue curve and squares - original filter version, red curve and triangles - modified filter version (in panel a). Reflection coefficient of the CLF optimised for high-power operation versus input power (in panel b).	70
4.2.12	Results of an electrical breakdown occurred in the distributed capacitance at the end of the first resonator (in panel a) and the N-connector damaged through the thermal effect (in panel b).	70
4.3.1	Schematic of a third-order BICLF with a straight loop consisting of a CLF and a tunable shunt capacitor C_{SH}	72
4.3.2	The HFSS sketch of a coaxial third-order BICLF with a straight loop.	74
4.3.3	The 2D-visualisation of the electric field patterns on the port surface in differential mode (panel a) and common mode (panel b).	75
4.3.4	The measurement (solid lines) and EM simulation results (dotted lines) of the BICLF with a straight loop: S_{D1} - blue curve, S_{DD} - orange curve and S_{C1} - green curve.	75

4.3.5	The measurement (solid lines) and EM-simulation results (dotted lines) of the BICLF with a straight loop: differential-mode impedance (in panels a and b) and common-mode impedance (in panel c).	76
4.3.6	Photograph of the coaxial third-order BICLF with a straight loop (inside and top views).	77
4.3.7	Representation of the measurement results in the ADS software.	77
4.3.8	A BICLF with a pulse shaping network consisting of a BICLF with a straight loop (inside the dashed rectangle) and a lumped-element PSN for impedance matching, containing adjustable shunt and series capacitances.	78
4.3.9	Measurements (solid lines) and ADS simulations (dotted lines) of the BICLF with a PSN: S_{D1} - blue curve, S_{DD} - orange curve and S_{C1} - green curve.	80
4.3.10	The measurement results (solid lines) and ADS simulation results (dotted lines) of the BICLF with a PSN: real and imaginary parts of the differential-mode impedance (in different scaling in panels a and b) and common mode impedance (in panel c). . . .	81
4.3.11	Photograph of the BICLF with a PSN (top view with mounted test PCB and inside view).	82
4.3.12	A third-order BICLF with an electro-magnetic input loop consisting of a CLF and a tunable shunt capacitor.	84
4.3.13	The HFSS sketch of a coaxial third-order BICLF with an electrically-long input loop.	85
4.3.14	The HFSS sketch of a third-order BICLF with an electrically-long loop. There is a visualisation of the E-field strength pattern along the first resonator.	85
4.3.15	The measurement (solid lines) and EM-simulation results (dotted lines) of the BICLF with electrically long loop: S_{D1} - blue curve, S_{DD} - orange curve and S_{C1} - green curve.	86

4.3.16	The measurement (solid lines) and EM-simulation results (dotted lines) of the BICLF with an electrically-long loop: real and imaginary parts of the differential-mode impedance (in panels a and b) and common mode impedance (in panel c).	87
4.3.17	Photograph of the BICLF with an electrically-long loop (inside view).	88
4.3.18	The HFSS sketch (in panel a) and a photograph (in panel b) of the microstrip third-order ST BICLF with an electrically-long input loop.	89
4.3.19	The measurement (solid lines) and EM-simulation (dotted lines) results of the ST BICLF: S_{D1} - blue and S_{C1} - green curves.	90
4.3.20	The measurement (solid lines) and EM-simulation (dotted lines) results of the ST BICLF: real and imaginary parts of the differential-mode impedance (in panels a and b) and common mode impedance (in panel c).	91
4.3.21	A third-order BICLF with an electrically-short input loop consisting of a CLF with a tunable shunt capacitor. The electrically-short input loop is represented by its equivalent inductance L_{loop}	93
4.3.22	The HFSS sketch of a coaxial third-order BICLF with an electrically-short input loop.	93
4.3.23	Photograph of the BICLF with an electrically-short input loop (inside view).	94
4.3.24	The measurement results of the BICLF with an electrically-short loop: S_{D1} - blue, S_{DD} - orange and S_{C1} - green curves.	94
4.3.25	The measurement of the BICLF with an electrically-short input loop: real and imaginary parts of the differential-mode impedance (in panels a and b) and common-mode impedance (in panel c).	95
5.1.1	The simplified switch-based model of the GaN HEMT [3].	100

5.1.2	A CMCD PA system comprising a 50% duty cycle square wave generator, a push-pull amplifier on GaN transistor models, biasing network (RF chokes L_{ch} and voltage supply V_{cc}), a third-order lumped-element reconstruction BPF and a balun.	101
5.1.3	The simulated waveforms of the drain voltage and drain current in the CMCD PA system as shown in Fig. 5.1.2.	102
5.1.4	The shape of the drain current of the class-D PA in different driving conditions.	104
5.1.5	A balanced input BPF with parasitic capacitances to ground C_g at the filter input.	105
5.1.6	ADS simulation results of the balanced input BPF at 450 MHz with parasitic capacitances to ground: the magnitude of the input impedance for the common mode (in panel a) and the input resistance for the differential mode of excitation (in panel b). The common-mode input magnitude is infinite when $C_g = 0$ pF.	106
5.1.7	The ADS simulation results: change of the shape of the drain currents (shown by the arrows) when the capacitance to ground grows (the shape close to rectangular corresponds to $C_g = 0$).	107
5.1.8	The ADS simulation results of the CMCD PA system operating at 450 MHz (in panel a) and the CMCD PA system operating at 900 MHz: drain efficiency (red curve), output power (blue curve) and dissipating power in the switch, $\frac{1}{2}I_1^2R_{dsON}$, (green curve) as functions of the parasitic capacitance to ground C_g	108
5.1.9	ADS simulation results of the class-D PA with the ST filter (red curves) and the DT filter (blue curves) as functions of sweeping centre frequency: a) - scattering parameters, b) - Smith chart, c) - output power, d) - drain efficiency, e) - maximum drain voltage, f) - dissipating power in the switch, $\frac{1}{2}I_1^2R_{dsON}$	110

5.2.1	A CMCS PA system comprising a one-bit modulator, a push-pull amplifier on GaN transistor models, biasing network (RF chokes L_{ch} and voltage supply V_{cc}), a reconstruction band-pass filter, and a balun.	112
5.2.2	ADS simulation results: drain voltage and current of the CMCS PA when driven by the PLM one-tone signal.	113
5.2.3	The ADS simulation results: drain voltage and current of the CMCS PA when driven by the $\Delta\Sigma$ one-tone signal.	115
5.3.1	The schematic diagram (in panel a) and chip photograph of a 2-stage digital PA in $0.25\ \mu\text{m}$ gate length technology (in panel b) [13] (source: FBH, Berlin, Germany).	117
5.3.2	Photograph of the demonstrator of a CMCS PA for the TETRA frequency band. There are the high speed digital driver amplifiers, the GaN HEMT MMICs, the GaAs Schottky diodes, the biasing network, and the control circuitry. The BICLF with a PSN on the rear side serves as mounts for the PA circuitry [14]. .	118
5.3.3	The schematic diagram (in panel a) and chip photograph (half area of a symmetrical chip) of a 2-stage digital PA in $0.25\ \mu\text{m}$ gate length technology (in panel b) [15] (source: IAF, Freiburg, Germany).	119
5.3.4	Photograph of the demonstrator of a CMCS PA for the GSM frequency band (version 1). There are the high speed digital driver amplifiers, the GaN HEMT MMICs, the GaAs Schottky diodes, the biasing network, and the control circuitry. The BICLF with an electro-magnetic input loop on the rear side serves as mounts for the PA circuitry [16].	120
5.3.5	Photograph of the demonstrator of a CMCS PA for the GSM frequency band. There are the high speed digital driver amplifiers, the GaN HEMT MMICs, the GaAs Schottky diodes, the biasing network, the control circuitry, and the ST microstrip BICLF, which is mounted perpendicularly to the board.	121

5.4.1 Typical measurement results of the class-S PA with a DT reconstruction filter operating for test purposes in a class-D regime (driven by a 50% duty cycle square wave) [17]. 122

5.4.2 Typical result for the measured output power of the class-S PA with a DT reconstruction filter, operating for test purposes in a class-D regime (driven by a 50% duty cycle square wave) over the specified bandwidth around 900 MHz centre frequency. . . . 124

5.4.3 Typical measurement results of the class-D PA (a) and of the class-S PA (b) with a DT reconstruction filter [16]. There are output power (green curves), drain efficiency (red curves), and drain current (blue curves) as functions of the drain voltage. . . 125

5.4.4 Typical result for the measured output power of the class-S PA with a ST reconstruction filter, operating for test purposes in a class-D regime (driven by a 50% duty cycle square wave) over the specified bandwidth around 900 MHz centre frequency: for different biasing voltages of 2 V (red curve), 7 V (blue curve) and 15 V (light blue curve). 126

5.4.5 Measurement results of the class-S PA with a ST reconstruction filter, operating for test purposes in a class-D regime (driven by a 50% duty cycle square wave). There are output power (red curve), drain efficiency (blue curve), and drain current (green curve) as functions of the drain voltage. 127

5.4.6 Measurement results of the class-S PA with a ST reconstruction filter, which is driven by a BP-PLM QPSK signal. There are output power (red curve), drain efficiency (blue curve), and drain current (green curve) as functions of the drain voltage. 127

List of Tables

2.3.1 Modulation parameters, SNR, ACPR and coding efficiency of $\Delta\Sigma$ Ms.	22
2.3.2 Modulation parameters, and coding efficiency of a PLM and a BP-PLM [18].	24
3.2.1 Input impedance of a balanced input reconstruction filter for differential mode and common mode of excitation in and out of band.	32
3.3.1 Parameters of the DT and ST filter structures from Fig. 3.3.1 [8]. . .	38
3.4.1 Element values for the singly and doubly terminated third-order filters with a Butterworth transfer function for $\omega' = 1$ [12].	44
3.6.1 Specification for the reconstruction filter for a CMCS PA system, operating with the following transistors	51
5.1.1 The drain efficiency and output power of the CMCD PA system computed in different simulation engines.	103
5.1.2 ADS simulation results of the CMCD PA with different transistor models.	104
5.2.1 ADS simulation results: drain efficiency of the CMCS PA system when driven by the PLM.	114
5.2.2 ADS simulation results: drain efficiency of the CMCS PA system under a variety of driving conditions.	116

1 Introduction

1.1 State of the art of mobile communications

Since the first commercially automated cellular networks were launched in Japan (1979) and in Norway (1981), wireless mobile communications have developed rapidly and made growing demands on the data transfer rate, as illustrated in Fig. 1.1.1 [2]. The first generation (1G) systems used various standards which transmitted voice at the frequencies of 450/800 MHz and operated with analogue modulation. Since the 1990s they have been replaced by digital second generation (2G) systems using the Global System for Mobile Communications (GSM) standard in Europe. The GSM networks were designed for

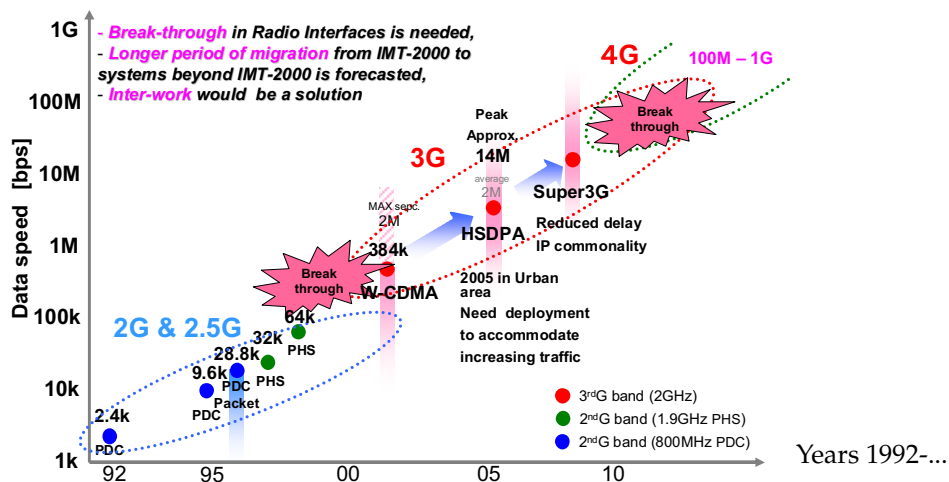


Figure 1.1.1: Evolution in data transmission rate [2].

data rates of up to 9.6 kbit/s using Gaussian Minimum Shift Keying modulation (GMSK) with an architecture based on Frequency Division Duplex (FDD) combined with Time Division Multiple Access (TDMA). Despite some modifications like the general packet radio service (GPRS) and the Enhanced Data rates for GSM Evolution (EDGE) with octagonal Phase Shift Keying (8-PSK) modulation, the data rate was still limited to 64 kbit/s. At present, GSM is the most common standard for cellular networks and covers more than 80% of the world's population in 219 countries [19].

3G mobile communications

Standardisation of the 3G Universal Mobile Telecommunications System (UMTS) was started by the 3G Partnership Project (3GPP) in 1992, but the first network was not launched until 2001. 3G networks were designed for data transfer rates of 2 Mbit/s, supporting a wide spectrum of application services including wide-area wireless voice telephone, mobile Internet access, and mobile TV, etc. The UMTS standard was used primarily in Europe at a frequency of 2.1 GHz, while the CDMA2000 systems were standardised by the 3GPP2 and predominated in the North America at frequencies of 1.7/1.9 GHz. Owing to Wideband Code Division Multiple Access (W-CDMA) in which one 5 MHz RF carrier is shared between several users, the 3G systems provide high spectral efficiency. Moreover, the UMTS networks employ Quadrature Phase Shift Keying (QPSK) and quadrature amplitude modulation techniques (16-QAM, 64-QAM), which can increase the data transfer rate and extend the network throughput [20]. High-Speed Packet Access (HSPA) and Evolved High-Speed Packet Access (HSPA+) innovations raised data transfer rates to 14 Mbit/s and 42 Mbit/s, respectively. However, in combination with Multiple Input Multiple Output (MIMO) technology and 8 carrier downlink operation it is theoretically possible for the data rate to reach 336 Mbit/s. Today there are more than 756 million UMTS-HSPA customers worldwide, representing 13% of the global wireless market [21]. 3G technologies are expected to increase their market share soon: "despite rapid UMTS deployment, market momentum means

that even now, most worldwide subscribers are still using GSM, although most new subscribers are taking advantage of UMTS. Only over many years, as subscribers upgrade their equipment, will most network usage migrate to UMTS" [22].

4G mobile communications

It was the idea of a global cellular network based on the Internet Protocol for video and voice with data rates of up to 100 Mbit/s which initiated the next generation mobile communications. The Long Term Evolution-Advanced (LTE-A) and IEEE 802.16m technologies were designed to meet requirements for 4G networks, but according to the current marketing designation some 3G technologies, e.g. HSPA+, LTE, and Worldwide Interoperability for Microwave Access (WiMAX), are already meeting this requirement [22]. Nevertheless, the 4G networks are designed to have high data rates and spectral efficiency enabled by utilisation of Orthogonal Frequency Division Multiplexing (OFDM), modulation schemes QPSK, 16-QAM, and 64-QAM and flexible channel bandwidths from 1.25/1.4 MHz up to 20 MHz. However, OFDM is characterised by a high Peak to Average Power Ratio (PAPR) of 12 dB demanding a Power Amplifier (PA) to operate in back-off. A traditional PA cannot provide high efficiency at back-off operation, which represents a challenge to novel amplifier systems for 4G networks [23]. Today the market share of the 4G systems constitutes only 1% of the global wireless market, but another 119 commercial LTE networks in 50 countries in operation are expected by the end of 2012 [24].

1.2 Green mobile communication

Today, because of the rapidly growing mobile industry and the extremely low power efficiency of the radio access networks, i.e. Base Transceiver Station (BTS), the energy efficiency of mobile communications has strategic priority. The total efficiency of the 3G BTSs (on LDMOS transistors and class-AB PA) is as low as or lower than 2%, which means that from about 6 kW of the total

power consumed only 120 W is available at the radio link [3]. The main cause is the inefficient class-AB PA (the theoretical maximum is 75.8%, but in practice it reaches only 4%), when it operated on average power at limited power efficiency (in the 3G systems the PAPR reaches 8 dB). A further cause resulting from growing power dissipation is the need for a cooling system. Considering that the PA and the cooling system consume the major part of the total BTS power applied [25], it is obvious that the improvement in the architecture of the PA systems themselves is the main challenge. Moreover, the growing mobile industry has a dramatic impact on greenhouse gas emissions, because of energy consumed by the network in operation, embedded emissions of the network equipment and emissions associated with buildings run by mobile operators [26]. The energy consumed can be reckoned in carbon dioxide (CO₂) emissions, whereby in 2002 the contribution of mobile communication networks was 64 Megatons of CO₂, and the expectation for 2020 is 178 Megatons [27]. It has been shown that enhancement of PA efficiency by up to 10% can result in 38% less power consumption and CO₂ emission [3], which can be further decreased by utilisation of alternative and renewable energy sources. A recent initiative on green mobile communications addresses the complex challenges of increasing PA efficiency for BTSs (Mobile-GaN research program [1, 14]), of improving 3G and 4G systems (EARTH project [25] and Green Touch consortium [28]), of making direct use of regenerative energy sources in BTSs [29], etc. However, much remains to be done, in order to reach the main goal in the European Union: the cutting of greenhouse gas emissions by 20% by 2020 and the improvement of energy efficiency by 20% [27].

1.3 The class-S power amplifier as a highly efficient alternative

In the Mobile-GaN research program (duration 01.08.2006-31.07.2009, consortium of eleven partners: Alcatel-Lucent Deutschland AG - Forschungszentrum ZFZ/OA; Fraunhofer-Institut fuer Angewandte Festkoerperphysik (IAF);

Lucent Technologies Network Systems GmbH; Technische Universitaet Ilmenau - Fakultae fuer Elektrotechnik und Informationstechnik - Institut Informationstechnik - Fachgebiet Hochfrequenz- und Mikrowellentechnik; IHP GmbH - Innovations for High Performance Microelectronics/Institut fuer innovative Mikroelektronik; Ferdinand-Braun-Institut fuer Hoechstfrequenztechnik (FBH) im Forschungsverbund Berlin e.V.; EADS Deutschland GmbH - Systems and Defence Electronics - Electronic Technical Operations; United Monolithic Semiconductors GmbH; MicroGaN GmbH; Rheinisch-Westfaelische Technische Hochschule Aachen - Lehrstuhl fuer Theoretische Elektrotechnik - Lehr- und Forschungsgebiet GaN-Bauelementtechnologie; Universitaet Kassel - Fachgebiet Hochfrequenztechnik), the goal was to develop a power amplifier system with enhanced power efficiency for BTS application [1]. For the research into and development and implementation of various amplifier systems operating in the Terrestrial Trunked Radio (TETRA), GSM and UMTS bands the choice of PA concept fell on class-S.

A class-S PA is a switched-mode power amplifier, theoretically with 100% power efficiency, which is achievable because the drain currents and the drain voltages do not overlap. The class-S amplifier employs two or more transistors as switches in voltage-mode or current-mode configuration. In contrast to a similarly configured class-D PA, it operates with compound signals conforming to the 3G and 4G mobile telecommunication standards and demands fourfold or higher oversampling of the RF signals. In the class-S PA, transmitter architecture is simple and, depending on the linearity of the one-bit modulators, will have high linearity.

In the Mobile-GaN research program, in following analysis of both types of configurations, the choice fell on the current-mode scheme. For the demonstrator designs, a pulse-length and a delta-sigma one-bit modulator were designed [4, 30]; several GaN HEMT Monolithic Microwave Integrated Circuits (MMICs) were developed [13, 15, 31]; and numerous reconstruction filter architectures were proposed. These reconstruction filter architectures are presented in this work. All these activities have been widely published in reports present-

ing practical implementations, integration aspects, simulation and measurement results.

1.4 Organisation of the Dissertation

This thesis is organised as follows:

Chapter 2, Class-S power amplifier system. The power efficiency of a PA for BTSs is a crucial parameter, but new standards of mobile communications demand that the power efficiency of the system be combined with high linearity. A class-S PA system offers both high power efficiency and high linearity. Its architecture and architecture requirements (particularly in respect of reconstruction filters) will be considered in this chapter.

Chapter 3, Requirements for reconstruction filters. A reconstruction filter as a part of the architecture of a class-S PA system has to fulfil numerous requirements: those set by BTS application, then those of the final stage configuration, those determining the type of RF one-bit modulator, and so on. All these requirements will be discussed and tabulated in the third chapter.

Chapter 4, Design and implementation of reconstruction filters. The challenges to reconstruction filter design are new and complex. The design algorithm with the priorities established will be presented in this chapter. Following a description of the design in ADS and HFSS software of several novel architectures for reconstruction filters and their subsequent measurement, these are critically analysed.

Chapter 5, Influence of the reconstruction filter on the power amplifier performance. As practice shows, the system blocks operate best when they are not connected to each other and are designed without reference to each other. The next challenging step is to assemble a complete PA system from such blocks.

In this chapter, the measurement results of class-S demonstrators will be discussed and the filter architectures will be analysed comprehensively. Finally, **Chapter 6, Conclusions** will give a summary and an outlook on possible future work.

2 Class-S power amplifier systems

There are numerous PA systems available for application in mobile communication, some of which will be discussed in this chapter in terms of power efficiency and linearity. A class-S PA will then be analysed in detail as an attractive amplifier system for BTS application offering simplified transmitter architectures and increased power efficiency. The class-S PA architecture and its building blocks will be considered, together with the issues and potential influences of each block on a reconstruction output filter. The chapter concludes by pointing out key issues for reconstruction filter design.

2.1 RF power amplifiers principles from class-A to class-S

The 3G and 4G systems have been designed for complex modulation techniques, such as QPSK, 16-QAM or 64-QAM, in which two quadrature components (I & Q) are modulated. Besides increased data rates, these modulations allow more efficient use of the frequency spectrum. On the other hand, they are associated with widely varying envelopes of the RF signals, which will imply a high PAPR, for example 8 dB for W-CDMA and 12 dB for OFDM. But in order to amplify these RF signals linearly, traditional amplifiers have to operate in back-off at low efficiency [23]. Consequently, the requirements for a PA for BTSs in terms of power efficiency and linearity will be more stringent. In the context of wireless applications the linearity can be expressed by an Adjacent Channel Power Ratio (ACPR) and an Error Vector Magnitude (EVM). For instance, the UMTS standard requires the ACPR to be at a level of -45 dB for

5 MHz offsets and -50 dB for 10 MHz offsets below the first or above the last carrier frequency used. The UMTS standard also demands that the EVM be not worse than 17.5%, when the base station is transmitting a composite signal using QPSK modulation, and 12.5% in the case of 16-QAM modulation [6]. It is important to analyse PAs in terms of both power efficiency and linearity at one and the same time.

The usual way of classifying RF PAs is by their mode of operation. The operation mode determines whether the RF power transistor acts as a high-resistance current source (traditional classes: A, B, AB, and C) or as a low-resistance switch (switched-mode PAs: class-D, E, F, and S). Besides operating in different modes, PAs with resistive load can be distinguished by their configuration: single-ended amplifier, push-pull voltage-switch or push-pull current-switch amplifiers [32]. The traditional RF PAs can be defined in terms of the conduction angle, indicating the part of the cycle of the RF input signal during which the transistor conduction occurs [32]:

- In a class-A PA the transistor is conducting all the time (conduction angle is equal to 2π), which provides high linearity and simplicity. But power dissipation in the transistor results in low power efficiency, theoretically reaching only $\eta_{max} = 50\%$.
- A class-B amplifier conducts for only half the time (conduction angle π). The price of this enhancement of the efficiency ($\eta_{max} = 78.5\%$) is deterioration in the linearity of the device.
- In a class-C PA transistors are ON for less than half of the time: the conduction angle is thus less than π . Theoretically, the efficiency is equal to 100% only when the output power is zero: an impractical situation.
- A class-AB is a compromise between the classes A and B in terms of efficiency ($\eta_{max} = 78.5\%$) and conduction angle (conduction angle $\in (\pi; 2\pi)$).

However, in all these cases, the maximum efficiency can be achieved only if the amplifier operates at the maximum power. In practice, the amplifiers will be

operating in back-off at low power and low efficiency. In order to enhance the efficiency, numerous techniques have been devised, e.g. the Doherty amplifier, the out-phasing Chireix amplifier, the Envelope Elimination and Restoration (EER) technique, and so on [33, 34].

Efficiency can also be enhanced to 100% if the active device operates as a switch. This type of PA is called a Switched-Mode Power Amplifier (SMPA). In SMPAs, the transistor acts in ON-state as a closed switch with a zero resistance, and in OFF-state as an open switch with an infinite resistance. Because there is no overlapping between the drain currents and voltages, the power dissipation in transitions is minimised. Some of the frequently used SMPAs are as follows [32].

- A class-E PA is based on one transistor driven as an ON-to-OFF switch. The load network provides either high drain voltage or high drain current at any instant. This minimises the power dissipation during the switching transitions, but the class-E PA suffers from nonlinearity.
- In order to shape the drain waveforms, a class-F PA employs a power transistor loaded by the harmonic resonators in the output network. The drain voltage contains only odd harmonics and has a square wave shape, while the drain current has a half-sine shape. An inverse class-F (F^{-1}) operates with a square wave current and half-sine voltage waveform. Depending on the number of harmonics, the power efficiency is given between 50% (a single harmonic, as in a class-A PA) and 100% (an ideal class-D PA) [35].
- A class-D PA employs two or more transistors as switches. There are two possible configurations of the class-D PA. In a Voltage-Mode Class-D configuration (VMCD), sinusoidal drain currents and 50% duty cycle square wave drain voltages are generated. Another configuration is a Current-Mode Class-D (CMCD) configuration, which operates with sinusoidal drain voltages and 50% duty cycle square wave drain currents. The switching transistors are driven by the constant envelope signals, e.g. FM and FSK signals. Theoretically, the power efficiency can reach 100%.

However, the SMPAs have the disadvantage of nonlinearity. In addition, numerous linearisation techniques, for example, analog and digital predistortion, feedforward and feedback techniques [33], have the effect of both decreasing power efficiency and introducing complexity and instability. For all these reasons, a class-S PA with simplified transmitter architectures, low harmonic distortion, and increased power efficiency becomes an interesting prospect for mobile communications.

2.2 State of the art of class-S power amplifiers

In some applications at audio frequencies, a class-S PA system is known as a class-D PA system. Such amplifiers are driven by a band-pass Delta-Sigma Modulator ($\Delta\Sigma\text{M}$) or by a Pulse-Length Modulator (PLM, or a pulse width modulator - PWM) [36–39]. Several demonstrators operating at a centre frequency of 10 MHz with high linearity and high drain efficiency (of 50%) have been presented [40, 41].

In 1998 Jayaraman proposed a class-S PA concept for wireless communication and showed (by simulation) a potential implementation for operation at 800 MHz [42]. Further investigations are being carried out worldwide by different research groups, e.g. in the University of California (USA) under the supervision of Prof. Asbeck [42, 43], in the Simon Fraser University (Canada) under Prof. Stapleton [44–48], in the National University of Ireland by Dr. Farrell [49–53]. Much work has been devoted to the study of a $\Delta\Sigma\text{M}$ and a RF VMCD PA from various different aspects, e.g. coding efficiency, optimum load impedance, output power, conducting losses, capacitive switching losses, drain efficiency, etc. There is an investigation of loss mechanisms in a class-S system reported in [54, 55], where the sources of losses pointed out: the odd harmonic leakage currents, the finite transition time of the transistors, the nonzero knee voltage of the transistors, and so on. In this study, the simulation results showed a drain efficiency of 52% with a 10 dB PAPR W-CDMA source signal at a centre frequency of 500 MHz [45]. But all the above reports present a VMCD configur-

ation, which assumes an ordinary two-port band-pass filter.

In 2006, several class-S demonstrators were presented by the National University of Ireland [53]. The demonstrators consisted of a CMCD bridge PA, resonant LC circuit, a lumped element balun, and an FPGA for implementation of modulated signal. Measured drain efficiency reached 65% when the system operated with a single tone signal at 930 MHz. However, because of the FPGA board, these demonstrators represented one specific case only.

There are some demonstrators described in [56]. They were based on an H-bridge VMCD PA with GaAs MESFETs driven by a $\Delta\Sigma$ M. Measurement results showed an output power of only 16 dBm and a drain efficiency of 8%, the effect of low-quality transistors, poor output impedance matching, and losses in the output filter (4 dB at the centre frequency of 170 MHz and 3 dB bandwidth of 3 MHz). This is the first time that the importance of the output circuit is mentioned in literature and some of the requirements discussed. Another H-bridge VMCD PA at a centre frequency of 800 MHz was implemented with 0.18 μ m CMOS devices [57]. Drain efficiency of 31% was achieved with an ACPR of -43 dBc for CDMA signals at an output power of only 15 dBm. The output circuit was realised off-chip. It consisted in a coaxial balun, two resonators (with unloaded quality factor of 6) and transmission lines, acting like impedance transformers.

The state of the art in class-S PAs has been presented in the context of work in the Mobile-GaN research program. For instance, a switch-mode amplifier set on a bit-pattern generator as a $\Delta\Sigma$ M but without filter was presented in [13]. The PA system provided a power added efficiency of 80% at an output power of 6.5 W. The design met none of the problems that had in other cases involved consideration of a reconstruction filter and of realistic modulators. The realisation of a reconstruction filter and its influence on amplifier performance are mentioned in articles of the Mobile-GaN working group supervised by Prof. Heinrich of the Ferdinand-Braun-Institut für Höchstfrequenztechnik. The group presents both voltage-mode and current-mode class-S PAs [58–64]. The theoretical foundation and a practical demonstration of a class-S PA are

covered in [3, 65–69]. The other class-S demonstrator, operating at 450 MHz, was presented in [70]. In this work, an FPGA board was used for generation of a $\Delta\Sigma$ sequence. In all the above mentioned work, the reconstruction filters were implemented on SMD components with a low quality factor, just to test a general idea. Several CMCS PAs have been assembled and experimentally investigated by partners in the Mobile-GaN research program [14,16,17,71]. Some of these results are presented in this work.

2.3 Architecture of class-S power amplifiers

A class-S PA is a switched-mode power amplifier with two or more transistors acting as switches. The class-S PA can be configured in voltage mode and in current mode. Its architecture in either mode is simple, consisting of the following three basic building blocks [42], which are shown in Fig. 2.3.1: 1. A one-bit modulator, e.g., a PLM or a $\Delta\Sigma$, maps the information contained in the high-frequency carrier signal into a stream of pulses of variable length but constant amplitude. 2. A switching amplifier, which may consist of two parts, a driver and a push-pull final stage, provides the necessary amplification by switching a bias source. 3. A band-pass filter serves to reconstruct the amplified signal and to match the final stage to an antenna. The time signals and spectra at each building block are presented in Fig. 2.3.1.

It is possible for the class-S PA system to operate with the compound signals utilised in the 3G and 4G mobile telecommunication networks. Since the final stage can be regarded as a linear stage for the modulated binary signal, the linearity of the amplifier is determined only by the modulator. Both modulators mentioned, PLM and $\Delta\Sigma$, can provide a high degree of linearity, with the result that the class-S amplifier can satisfy all requirements of modern communication systems. At the same time, as is typical of SMPAs, a class-S PA can be responsible for power efficiency of 100%.

Despite the simple architecture, the design and implementation of a class-S PA present certain challenges, mainly associated with parasitic elements in the

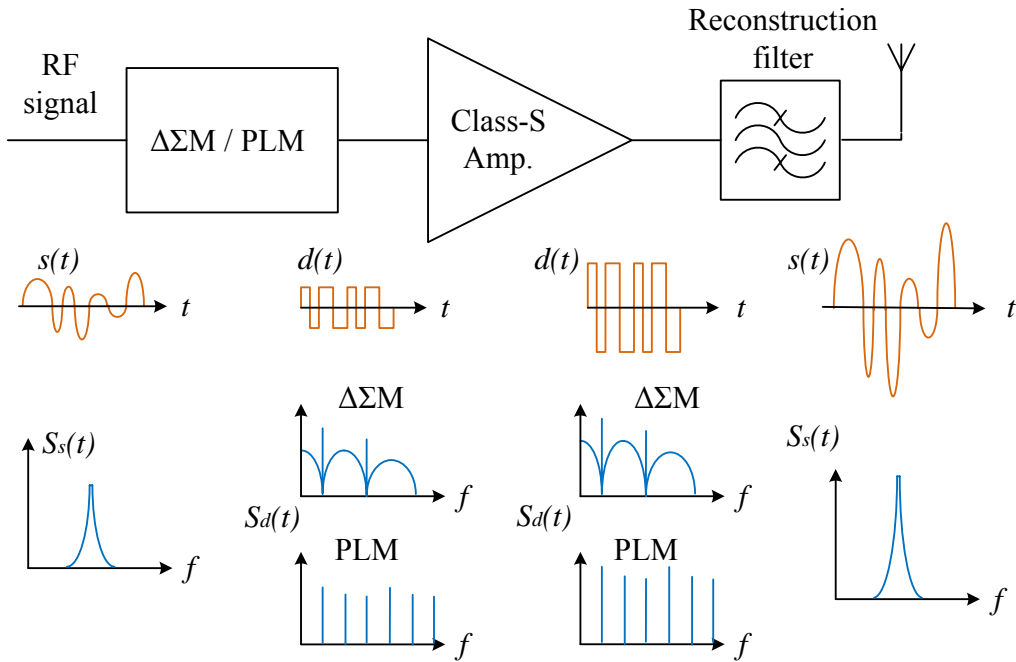


Figure 2.3.1: Basic building blocks of a class-S PA system: a one-bit modulator, a switching amplifier and a reconstruction filter. Time signals (red curves) and spectra (blue curves) are shown at each building block.

GaN HEMTs, poor coding efficiency of the modulators, critical heat sensitivity of MMICs, complications in pre-amplifier design and provision of the operation conditions of the final stage.

2.3.1 Switching amplifiers

To take the second building block first, the heart of a class-S PA system is a switching amplifier. In the present work the suitable types of switching amplifiers were limited by the fact that digital driving signals were non-periodic and broadband. When both configurations of the class-S PA had been analysed, the choice fell on a push-pull Current Mode Class-S (CMCS) configuration, because the both switching transistors can be mounted to a common ground, and this can also act as a heat sink. Moreover, a Voltage Mode Class-S (VMCS) configuration would make more stringent demands on transistors driving. Detailed analysis of both VMCS and CMCS PAs in terms of both coding and drain effi-

ciency has been presented in [3].

The simplified schematic of a CMCS PA consists of two transistors (Q_1 and Q_2), load resistance R_l , supply voltage V_{cc} , RF chokes L_{ch} , and a parallel LC circuit tuned to the fundamental frequency $\omega_0 = 1/\sqrt{L \cdot C}$ with insertion losses of L_0 (Fig. 2.3.2). The transistors are driven out-of-phase so that, assuming PLM or $\Delta\Sigma M$, there is alternating switching between the ON/OFF states. The supply voltage V_{cc} applied to the high-value RF choke results in constant current $I_0 = I_1/2 = I_2/2$. Here I_1 and I_2 are the maximum drain-source currents through the switches. The current I_0 is directly proportional to supply voltage, and inversely proportional to R_{dsON} , to load resistance and to peak amplitude coding efficiency. At any instant, the RF chokes (turned on and off by switches) act as current supplies. The time signals at the drains of a class-S PA system driven by a PLM are shown in Fig.2.3.3. The drain-source currents through the switches are described as:

$$\begin{aligned} i_1(\omega t) &= I_1 \cdot d_n(\omega t), \\ i_2(\omega t) &= I_2 \cdot \overline{d_n(\omega t)}, \end{aligned} \quad (2.3.1)$$

where $d_n(\omega t)$ and $\overline{d_n(\omega t)}$ defines the normalised two-level modulated signal and its inverse at the inputs of the switches. At the moment when the switch

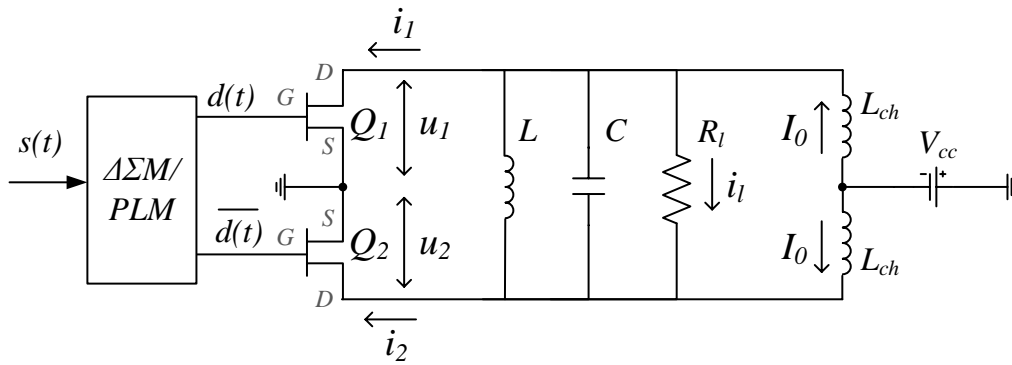


Figure 2.3.2: Current-mode class-S PA system comprising a $\Delta\Sigma M$ or PLM, a push-pull transistor amplifier with biasing network (RF chokes L_{ch} and voltage supply V_{cc}), a parallel resonant circuit (L and C), and a load resistance R_l .

Q_1 is turned on and Q_2 is turned off, the currents through the switches are:

$$\begin{aligned} i_1 &= I_1, \\ i_2 &= 0. \end{aligned} \tag{2.3.2}$$

The application of the odd-harmonic components of the rectangular drain current to the parallel LC circuit results in voltage across the load at fundamental frequency only. The voltage across and current through the load can be found

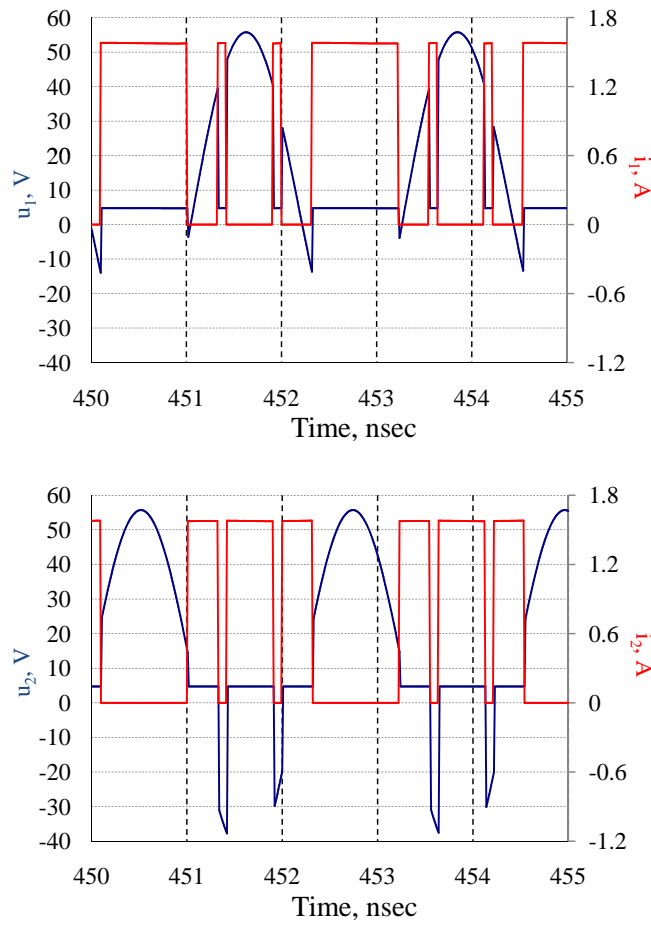


Figure 2.3.3: Waveforms of drain currents (red curves) and drain voltages (blue curves) in a current-mode class-S PA system when driven by a PLM. The ADS simulation was carried out under the following conditions:

$$V_{cc} = 17.5 \text{ V}, R_{dsON} = 3 \text{ Ohms}, R_{lOpt|class-S} = 65 \text{ Ohms}.$$

from the following equations:

$$\begin{aligned} i_l(\omega t) &= L_0 \cdot I_0 \cdot \eta_{pA} \cdot \sin(\omega t), \\ u_l(\omega t) &= L_0 \cdot R_l \cdot I_0 \cdot \eta_{pA} \cdot \sin(\omega t), \end{aligned} \quad (2.3.3)$$

where η_{pA} is peak amplitude coding efficiency and L_0 is insertion losses in the parallel LC circuit. The peak amplitude coding efficiency reflects the relations between currents in the PA system and is defined as the ratio between the Root Mean Square (RMS) value of the reconstructed signal and the RMS value of the modulated signal.

The voltages across the transistors Q_1 and Q_2 , because the ON-resistance is not zero, will be equal to:

$$\begin{aligned} u_1(\omega t) &= L_0 \cdot u_l \cdot \sin(\omega t) \cdot \overline{d_n(\omega t)} + R_{dsON} \cdot I_1, \\ u_2(\omega t) &= L_0 \cdot u_l \cdot \sin(\omega t) \cdot \overline{\overline{d_n(\omega t)}} + R_{dsON} \cdot I_2. \end{aligned} \quad (2.3.4)$$

At the moment when the switch Q_1 is turned on and Q_2 is turned off, the voltages across the switches are equal to:

$$\begin{aligned} u_1(\omega t) &= R_{dsON} \cdot I_1, \\ u_2(\omega t) &= L_0 \cdot R_l I_0 \eta_{pA} \cdot \sin(\omega t) + R_{dsON} \cdot I_2. \end{aligned} \quad (2.3.5)$$

At the optimum load, V_1 and V_2 can be replaced by the maximum available drain-source voltage swing V_{dmax} and I_1 and I_2 - by the maximum available drain-source current I_{dmax} . Eq. 2.3.3 can be used to find the optimal load:

$$R_{lOpt} = 2 \left(\frac{V_{dmax}}{I_{dmax}} - R_{dsON} \right). \quad (2.3.6)$$

However, statistical analysis can also be used, at least for a class-S PA driven by a $\Delta\Sigma M$. By this method, the optimum load is:

$$R_{lOpt|class-S} = 2.67 \dots 2.5 \cdot \frac{V_{dmax}}{I_{dmax}}, \quad (2.3.7)$$

and these results were employed in the study. The $R_{Opt|class-S}$ is 65Ω and 130Ω respectively for the 4 mm and 2 mm GaN HEMTs supplied by FBH (Berlin, Germany).

The most important power characteristics of any amplifier are drain efficiency η_D and output power P_{RFout} . The drain efficiency is defined as:

$$\eta_D = \frac{P_{RFout}}{P_{DCt}}, \quad (2.3.8)$$

where P_{DCt} is the DC power supplied to the transistors. The drain efficiency of the CMCS PA, with losses in the reconstruction filter and in the switches, can be found from the following equation [3]:

$$\eta_D = \frac{L_0^2 \cdot \eta_P}{\eta_P + 4 \cdot (R_{dsON}/R_l)'} \quad (2.3.9)$$

where L_0 is insertion losses in the reconstruction filter and η_P is the coding efficiency. The coding efficiency is defined as a ratio between the reconstructed load power and the total pulse train power. It shows how effectively the frequency spectrum is utilised and is defined by the modulator scheme, some of which are considered below. The coding efficiency is related to peak amplitude coding efficiency (η_{pA}) through the crest factor of the RF signal c_f , like:

$$\eta_P = \left(\frac{\eta_{pA}}{c_f} \right)^2. \quad (2.3.10)$$

The coding efficiency is a very important characteristic of the modulator scheme and should be increased as much as possible, in order to enhance spectrum use and total system efficiency. Eq. 2.3.9 shows the dramatic relation between drain efficiency and coding efficiency. The filter losses and ON-resistance in the switches have a significant impact on the PA performance as well. The non-zero ON-resistance aggravates the dramatic relation in Eq. 2.3.9 and reflects the GaN HEMT technology utilised.

One particular case in class-S PA systems is a class-D PA, similarly config-

urated: this will receive frequent mention in this work. The optimal impedance for a class-D PA system is:

$$R_{lOpt|class-D} = 1.57 \cdot \frac{V_{dmax}}{I_{dmax}}, \quad (2.3.11)$$

which is equal to 40Ω for the 4 mm GaN HEMTs. The drain efficiency of a CMCD PA driven by 50% duty cycle square wave can be found as [32]:

$$\eta_{D_{CMCD}} = \frac{P_{RF_{out}}}{P_{DC_t}} = \frac{L_0^2}{1 + \frac{\pi^2}{2}(R_{dsON}/R_l)}, \quad (2.3.12)$$

where L_0 is insertion losses in the reconstruction filter. This equation represents an "inaccessible upper limit" for the drain efficiency of a class-S PA system, because the coding efficiency of the one-bit modulators will always be less than 100%. It is important to notice that a class-D PA, also, suffers from the less-than-perfect coding efficiency, which can reach

$$\begin{aligned} \eta_{P_{class-D}} &= \frac{8}{\pi^2}, \\ \eta_{pA_{class-D}} &= \frac{4}{\pi} \end{aligned} \quad (2.3.13)$$

in theory: and (what might seem strange) represents value higher than unity for the peak amplitude coding efficiency. It would be logical to compare the RMS value of the reconstructed signal with the RMS value of the supply current, as a more usual reflection of the typical meaning of "efficiency". In this case the RMS of the reconstructed signal would, at $\frac{2}{\pi}$ of DC current, be lower than unity. In Eq. 2.3.13 the RMS value of the modulated signal is used, which is one half of the DC current, and explains the figure $\eta_{pA_{class-D}}$ (higher than 100%).

2.3.2 RF one-bit modulators

Analysis of the one-bit modulators as another of three main building blocks is important to the further design of the reconstruction filter, because

the drain currents or voltages (depending on the final stage configuration) have the same waveforms as the control signals. This is what will dictate the requirements for the filter input impedance out-of-band. The modulator scheme has not only to cope with compound signals, but also to ensure minimal switching losses in the power transistors. Two suitable modulator schemes are considered below.

A. Delta-sigma modulator

The concept of a $\Delta\Sigma$, as an analogue to digital converter based on quantised pulse lengths, was proposed as early as 1963. The basic architecture of a $\Delta\Sigma$, which includes a loop filter, a one-bit quantiser and a negative feedback loop with digital-to-analog converter, is shown in Fig. 2.3.4,a. The primary reason for using a $\Delta\Sigma$ is to move the quantisation noise outside of the desired signal band. The output signal of a $\Delta\Sigma$ exhibits noise-like behaviour (Fig. 2.3.4,b) [3], which after amplification has to be filtered by the reconstruction filter. The performance of a $\Delta\Sigma$ mainly depends on two parameters: the order of the modulator and the oversampling ratio of the input signal. The order will be a trade-off between low-in-band quantisation noise on one side and, on the other, high-out-of-band quantisation noise, increased implementation complexity and higher risk of instability. By oversampling ratio is meant the ratio of the

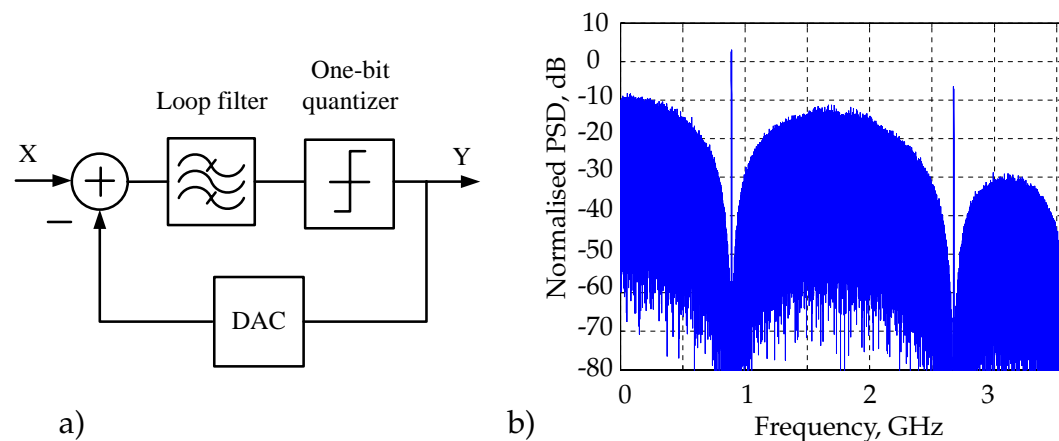


Figure 2.3.4: General topology (in panel a) and typical simulated power spectral density (in panel b) of a $\Delta\Sigma$ [3].

sampling frequency at twice the input signal bandwidth. In general, increasing the oversampling ratio decreases the level of the in-band noise.

A $\Delta\Sigma$ will have a high bit rate, which complicates the control of the transistors and contributes switching losses. Upon analysis of an $8 \times 250 \mu\text{m}$ GaN transistor model supplied by FBH in Berlin, a new concept of Quasi Low-pass $\Delta\Sigma$ Modulator with Manchester encoder (QL $\Delta\Sigma$ M) has been proposed [68]. This concept offers half the bit rate and more efficient transistor switching operation. However, it has more complex topology and creates more strict requirements for the reconstruction filter. According to Eq. 2.3.9, the drain efficiency of a class-S PA directly depends on the coding efficiency and claims priority attention. For this purpose, some particular cases were calculated in [3] and are presented in Table 2.3.1.

The state of the art in RF performance of a $\Delta\Sigma$ operating at 2 GHz was presented in [4]. The circuit was well suited to a class-S PA using a W-CDMA coding scheme. The architecture of modulator presented was fourth order. The chip, manufactured by a $0.25 \mu\text{m}$ SiGe BiCMOS process (with maximum transit frequency $f_T = 180 \text{ GHz}$), occupied an area of 1.4 mm^2 shown in Fig. 2.3.5,a. The

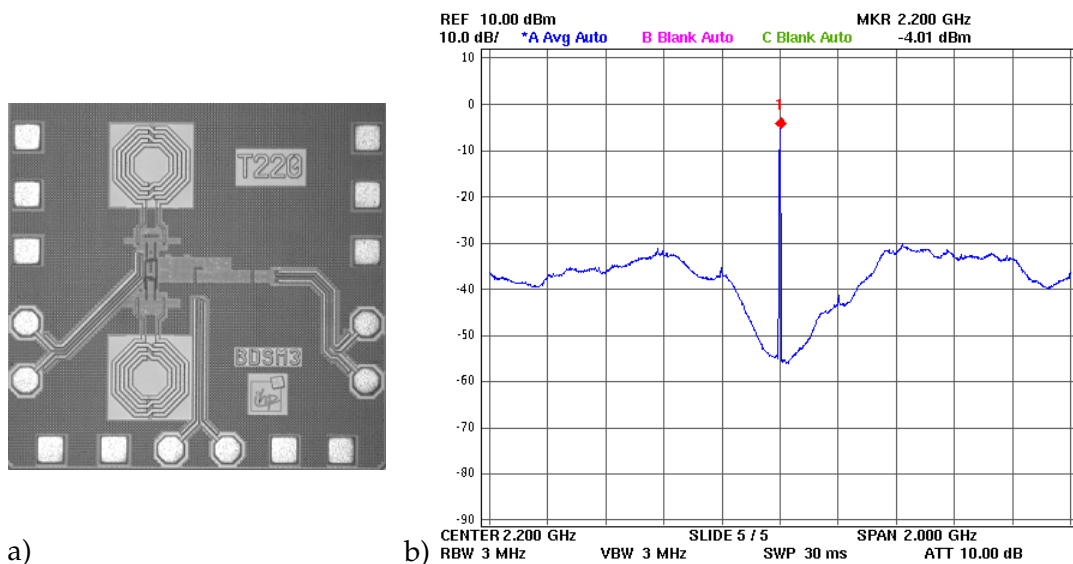


Figure 2.3.5: Photograph of the $\Delta\Sigma$ M chip (in panel a) and the measured output spectrum (in panel b) [4] (Source: IHP GmbH in Frankfurt/Oder, Germany).

$\Delta\Sigma\text{M}$ had lower than 2.3% EVM at input power of -30 dBm over the full tuning range. A normalised power spectrum density of the output signal is depicted in Fig. 2.3.5,b and shows increasing noise-level out-of-band and a dynamic range of 45 dB, referenced to a RBW of 3 MHz.

B. Pulse-length modulator

Another one-bit modulator suitable for a class-S PA system would be a PLM. The PLM generates a train of pulses, with widths varying according to the envelope of the input signal. A classic PLM (Fig. 2.3.6,a) consists in a comparator, which is driven at one input by a triangular reference signal and at the second input by the signal of interest. The spectrum of a PLM is shown in Fig. 2.3.6,b. It includes periodic parasitic harmonics above the centre frequency, which need to be filtered out by a reconstruction filter. Because the discrete spectrum is only located above the centre frequency, a PLM imposes less stringent requirements for a filter, than does a $\Delta\Sigma\text{M}$. A relatively simple architecture of a PLM was proposed for RF applications in 1973 [72], but its main disadvantage to date is extremely short pulses, which would necessitate very high operation frequency of the power transistors. An up-to-date implementation of a PLM without this disadvantage was proposed in [73]. But it was incompatible with a class-S PA system.

Another potential problem with PLMs is low coding efficiency. In theory, coding efficiency can reach 44.7% for a single-tone modulated signal. In case of modern digital signals, coding efficiency is dramatically impaired: some examples are presented in Table 2.3.2. Practical implementation of a PLM for a

Table 2.3.1: Modulation parameters, SNR, ACPR and coding efficiency of $\Delta\Sigma\text{Ms}$.

Modulator	SNR(dB)	ACPR(dB)	$\eta_{P_{\text{sinus}}}$ (%)	$\eta_{P_{\text{W-CDMA}}}$ (%)
$\Delta\Sigma\text{M}$	47.26	56.32	47.2	6.054
QL $\Delta\Sigma\text{M}$	49.9	55.34	26.11	3.212

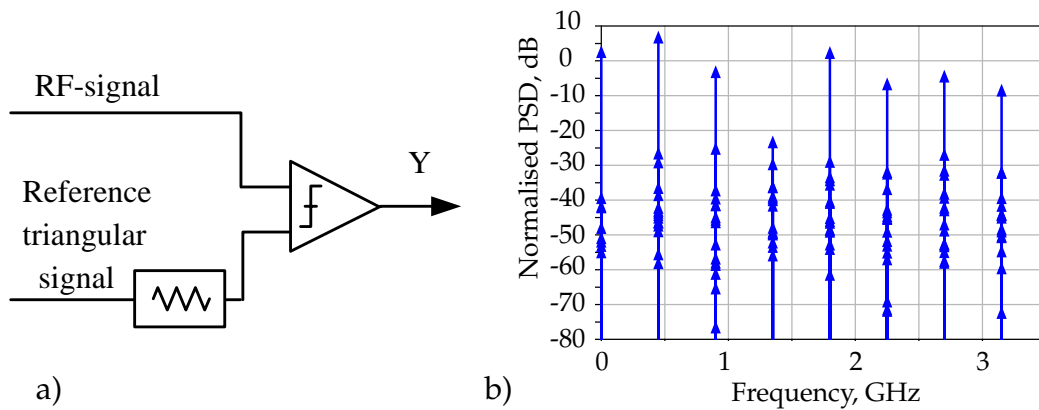


Figure 2.3.6: General topology (in panel a) and typical power spectral density (in panel b) of a PLM [5].

class-S PA operating at 450 MHz was presented in [30]. The PLM-chip was manufactured in a $0.25 \mu\text{m}$ SiGe BiCMOS process and is about 1 mm^2 in area. The measured EVM was less than 1% and ACPR less than -44.8 dB for a 64 QAM-test signal. The chip presented showed good results operating at a centre frequency of 800 MHz and a clock frequency of 3.2 GHz, but had poor EVM.

Another modulator concept suitable for a class-S PA would be a Band-Pass PLM (BP-PLM). In a BP-PLM, the modulated signal switches with the cycle of the carrier frequency. The spectrum of a BP-PLM includes harmonics at the DC and above the centre frequency. The design and successful implementation of a BP-PLM were presented in [18]. Measurement of the BP-PLM chip gave good results. A EVM of 1.4% for a QPSK-test signal and an ACPR of 41 dBc at 450 MHz were achieved. A BP-PLM is very promising in terms of coding efficiency: some particular cases are presented in Table 2.3.2.

2.3.3 Reconstruction filters

There are several different points of view from which to consider a reconstruction filter and these shed light on different aspects.

Application of the power amplifier system. A reconstruction filter has to fulfil the requirements for BTSs operating in 3G and 4G mobile networks: a major

Table 2.3.2: Modulation parameters, and coding efficiency of a PLM and a BP-PLM [18].

Modulator	$\eta_{P_{sinus}}$ (%)	$\eta_{P_{QPSK}}$ (%)	$\eta_{P_{16-QAM}}$ (%)
PLM	44.7	15.0	10.6
BP-PLM	45.0	39.0	29.7

priority. There must be a conformity with the emission masks, the power levels, and the various frequency bands in which modern mobile networks operate.

One-bit modulator. A second aspect is that the output signal of the final stage exhibits noise-like behaviour (in the case of a $\Delta\Sigma$ M in Fig. 2.3.4,b), or contains periodic parasitic harmonics (in the case of a PLM in Fig. 2.3.6,b). These frequency components require a reconstruction filter to filter them. At the same time, the filter has to pick up the fundamental frequency of the drain current and deliver it to the load. As a result, a band-pass reconstruction filter with a broad stop-band is the type required.

Final stage configuration. The choice of push-pull current mode final stage configuration demands a balanced input filter, or two BPFs with a balun to combine the signals. In a CMCS PA, the drain currents have a rectangular shape, while the drain voltages are cosine-shaped. As the rectangular shape of the drain currents should be maintained in order to sustain the high system efficiency, there will be some special requirements imposed on the filter input impedances in- and out-of-band for different modes of excitation.

Providing operation conditions for the power transistors. Fourthly, the filter is affected by the fact the GaN HEMT will operate at maximum available power only under the certain operating conditions, e.g. the maximum available drain current and voltage. These operating conditions depend on the optimal filter

impedance and on the filter termination, both of which will require definition and analysis.

Matching to antenna. Finally, a reconstruction filter, being an intermediate block between the final stage and an antenna, has to provide impedance transformation from the optimum impedance for the final stage to the $50\ \Omega$ of the antenna.

Thus, reconstruction filter design represents a challenge in view of the broadband spectra of the modulated signals and the actual GaN HEMTs with their numerous parasitic elements.

2.4 Conclusion of the class-S power amplifier system concept

This chapter has presented a class-S PA system, which can be described in summary as follows.

1. A class-S PA is an attractive candidate for wireless mobile communications because it offers high efficiency and high linearity and, at the same time, can operate with oversampled signals conforming to the 3G and 4G mobile communication standards.
2. When both configurations of the class-S PA had been analysed, the choice fell on a current-mode final stage configuration. The main advantage of this configuration is that both switching transistors are mounted on the common ground, which at the same time acts as a heat sink. This configuration will, however, require a reconstruction filter with a balanced input.
3. It is necessary for the reconstruction filter to fulfil the requirements for a modern BTS; to provide operating conditions for the final stage; and to conform to both modulation techniques, i.e. $\Delta\Sigma\text{M}$ and PLM.

2.4 Conclusion of the class-S power amplifier system concept

The requirements for reconstruction filters for class-S PA systems will be considered in detail in the following chapter.

3 Requirements for reconstruction filters

As mentioned in Chapter 2, there are numerous requirements for a reconstruction filter of a class-S PA system. The requirements of wireless BTSs for the 3G and 4G mobile telecommunication networks will here be considered first. The second section of this chapter will contain the requirements for the filter input impedances for different excitation modes. A comprehensive analysis of doubly and singly terminated filters will be presented in the third section and, moreover, it will be mathematically proven that only singly terminated filters can fulfil the requirements of current-mode power amplifiers. The last section explains in detail a novel approach for the impedance transformation of singly terminated filters design, a not insignificant issue for the current application.

3.1 Requirements for transmitter filters for wireless base stations

In BTSs, the transmitter and receiver filters are often combined in the duplexer, which has to fulfil requirements for the both filters. In this work, the requirements for transmitter filters will be considered in terms of:

- frequency selectivity complying with the 3GPP emission mask;
- reduced insertion loss;
- extended stop-band;
- power handling capability;
- frequency tunability.

3.1 Requirements for transmitter filters for wireless base stations

In the 3GPP specification there are four classes of BTSs [6]. They are defined by the coupling loss between a BTS and the user equipment. Each class is characterised by the out-of-band emission and the spurious emission. The out-of-band type results from the modulation process and non-linearity in the transmitter. This emission is specified in terms of a spectrum emission mask and ACPR. The spurious type is the combined results of harmonics emission, parasitic emission, intermodulation products and frequency conversion products [6]. The requirements for the spectrum emission mask for the BTSs with their different power levels are presented in Fig. 3.1.1. As can be seen, it is necessary for a transmitter filter to provide high suppression in stop-band (better than 27.5 dB) at offset of several MHz from the pass-band. Like any transmitter filter, the reconstruction filter has to comply with these emission masks. For the application envisaged, two pass-bands will be considered, i.e. 445 MHz to 455 MHz (TETRA) and 890 MHz to 910 MHz (GSM).

Because of the noise-like $\Delta\Sigma$ spectrum (Fig. 2.3.4) and periodic parasitic harmonics in the PLM spectrum (Fig. 2.3.6), a reconstruction filter has to

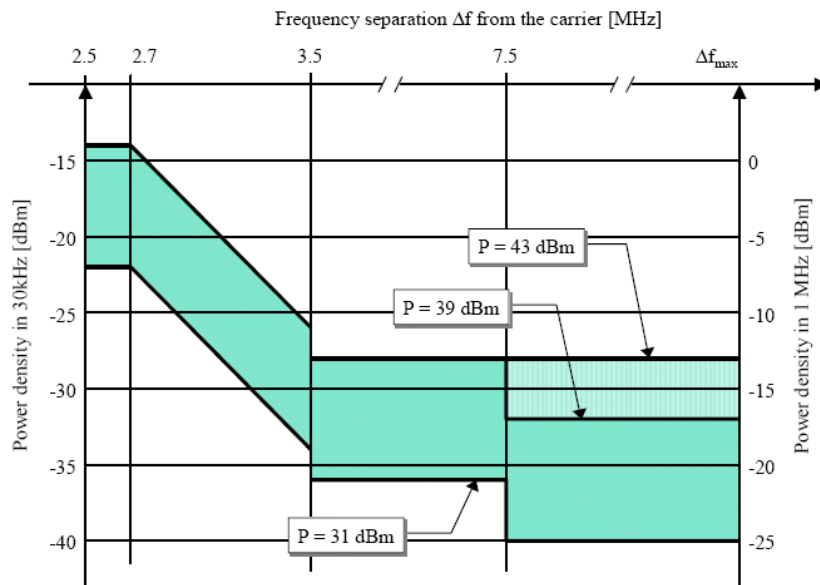


Figure 3.1.1: Illustrative diagram of spectrum emission mask for different classes of the UMTS BTSs defined by a level of output power of 31 dBm, 39 dBm and 43 dBm [6] where Δf_{max} is 12.5 MHz.

provide a broad stop-band. The second pass-band is required to be at least five times higher than the centre frequency. According to the emission mask, the filter has to provide high suppression in the stop-band. In the pass-band, low insertion loss is crucial, because it impacts the total efficiency of the amplifier system. (As example, the requirements for E-GSM 900 Alcatel-Lucent BTS are attenuation of 80 dB for RX-band and insertion losses of 1 dB in TX-band [10].) For significant progress to be achieved in amplifier efficiency, the insertion loss should be lower than 1 dB, which would, however, bring with it degradation of the overall efficiency by a factor of 0.8. Besides the aspects mentioned so far, there has to be a trade-off between the filter slopes, the insertion losses, the required bandwidth, broad stop-band, and the degree of miniaturisation.

Turning to the power handling capability, the basic parameter is that in BTSs for mobile communications, the power amplifiers operate at high-power levels up to 100 W. The reconstruction filter has to handle this power level, without degrading its selectivity characteristics. The high input power and finite insertion loss will result in growing power dissipation in the filter. It is of high importance, because of the critical heat sensitivity of the MMICs mounted on the filter body.

Finally, in order to cover the desired communication bands, a reconstruction filter should be tunable over more than one octave (for instance, TETRA and GSM frequency bands), which would significantly reduce system cost and complexity.

3.2 Input impedances for different excitation modes

As mentioned above, a CMCS configuration of the final stage necessitates a balun or a balanced input filter for combining the signals. Fig. 3.2.1 describes the reconstruction filter as a three-port device. The single-ended output port 1 is assumed to be connected to an unbalanced antenna. The input ports 2 and 3 are single-ended. Together they can be taken as a differential port (this

3.2 Input impedances for different excitation modes

combination is given the number 2). Differential port 2 can be excited by two different modes:

- *Differential mode* is the term used when the single-ended ports 2 and 3 are excited by two signals opposite in phase of equal magnitude.
- *Common mode* is the term used when the single-ended ports 2 and 3 are excited by two signals in-phase of equal magnitude.

The impedances of differential and common mode can be found from the following equations [7]:

$$Z_{diff} = (Z_2 + Z_3) \parallel \left(\frac{1}{Y_2} + \frac{1}{Y_3} \right), \quad (3.2.1)$$

$$Z_{com} = (Z_2) \parallel (Z_3 + \left(\frac{1}{Y_g} \right) \parallel (Y_2 + Y_3)),$$

where Y_2 , Y_3 and Y_g are the admittances to ground, shown in Fig. 3.2.2. Eq. 3.2.1 describes an ideal matching circuit with symmetrical filter pins $Z_2 = Z_3$ and $Y_2 = Y_3$. There is no differential voltage across the admittance Y_g , which constitutes an additional issue for the filter design, as "hot points" must be avoided. In contrast, common-mode impedance depends on all components. To take one example, if the port impedance of a single-ended measurement system is Z_0 ,

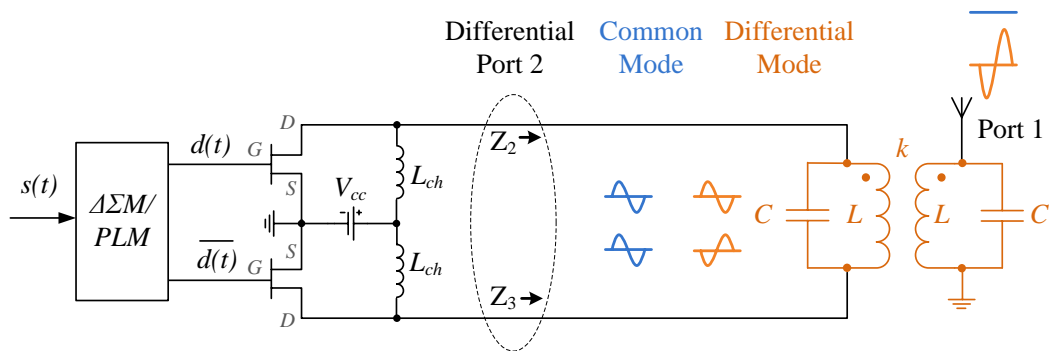


Figure 3.2.1: A CMCS PA including a second-order balanced input BPF. The differential port 2 can be excited in differential mode (orange curves) and in common mode of excitation (blue curves).

3.2 Input impedances for different excitation modes

the input impedances would be $Z_{diff} = 2 \cdot Z_0$ and $Z_{com} = \frac{1}{2} \cdot Z_0$, assuming $Z_2 = Z_3 = Z_0$, $Y_2 = Y_3 = 0$ and $Y_g = \infty$. In the case of a floating device without any connection to ground ($Z_2 = Z_3 = Z_0$, $Y_2 = Y_3 = Y_g = 0$), the differential and common mode impedances take the values of $Z_{diff} = 2 \cdot Z_0$ and $Z_{com} = \infty$. At the same time any balanced device can be completely described by the mixed-mode scattering parameters S^M . These parameters can be computed from the usual single-ended S-parameters S_{ij} , according to the following equation [7]:

$$S^M = \begin{pmatrix} S_{11} & S_{1D} & S_{1C} \\ S_{D1} & S_{DD} & S_{DC} \\ S_{C1} & S_{CD} & S_{CC} \end{pmatrix} \quad (3.2.2)$$

$$= \frac{1}{2} \begin{pmatrix} 2 \cdot S_{11} & \sqrt{2}(S_{12} - S_{13}) & \sqrt{2}(S_{12} + S_{13}) \\ \sqrt{2}(S_{21} - S_{31}) & (S_{22} - S_{23} - S_{32} + S_{33}) & (S_{22} + S_{23} - S_{32} - S_{33}) \\ \sqrt{2}(S_{21} + S_{31}) & (S_{22} - S_{23} + S_{32} - S_{33}) & (S_{22} + S_{23} + S_{32} + S_{33}) \end{pmatrix},$$

where the subscripts C and D denote the common and differential modes respectively. A balanced device should convert single-ended signals into the differential mode without losses and reject the common mode. The common-mode rejection ratio S_{1D}/S_{1C} expresses a ratio of the targeted circuit response compared to the unwanted response. This ratio can be improved with zero or infinity common-mode impedance, but high-ohmic common-mode impedance is preferable, as it does not affect the differential-mode impedance.

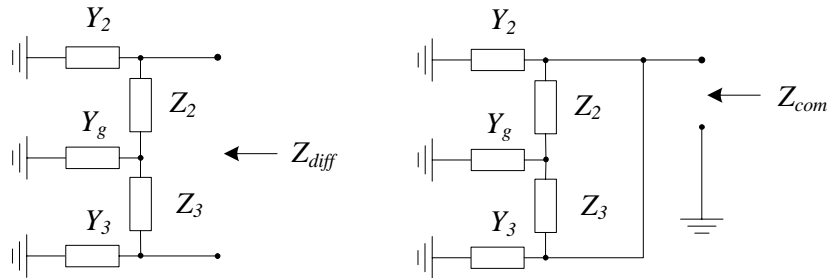


Figure 3.2.2: Definition of differential-mode and common-mode impedances [7].

3.2 Input impedances for different excitation modes

Because the final stage operates in current mode, the balanced input filter has to exhibit optimal impedance (see Eq. 2.3.7) for the differential mode of excitation, thereby providing the maximum available drain currents and voltages. At the same time, the single-ended impedances at the filter input, Z_2 and Z_3 , have to be equal, or there will be asymmetry at the filter input. As a result, the following must apply:

$$f \in \left[f_0 - \frac{\Delta f}{2}; f_0 + \frac{\Delta f}{2} \right] : \quad \begin{aligned} Z_{diff} &= R_{lOpt|class-S} \\ Z_2 = Z_3 &= \frac{R_{lOpt|class-S}}{2} \end{aligned} \quad (3.2.3)$$

The common mode of excitation in band requires suppression in order to eliminate any short to ground. This issue can be described in terms of either the common-mode impedance, or the admittances to ground at the filter input, Y_2 and Y_3 , as:

$$f \in \left[f_0 - \frac{\Delta f}{2}; f_0 + \frac{\Delta f}{2} \right] : \quad \begin{aligned} Z_{com} &= \infty \\ Y_2 = Y_3 &= 0 \end{aligned} \quad (3.2.4)$$

In summary, an ideal lossless filter, which is matched at both ports and perfectly suppresses common mode of excitation, can be described by the *in-band* input impedances in Table 3.2.1 or by the mixed-mode S^M -matrix:

$$S^M = \begin{pmatrix} 0 & 1 & 0 \\ 1 & 0 & 0 \\ 0 & 0 & 1 \end{pmatrix}. \quad (3.2.5)$$

Table 3.2.1: Input impedance of a balanced input reconstruction filter for differential mode and common mode of excitation in and out of band.

Frequency range	Z_{diff}	Z_{com}
$f \in \left[f_0 - \frac{\Delta f}{2}; f_0 + \frac{\Delta f}{2} \right]$	$R_{lOpt class-S}$	∞
$f \notin \left[f_0 - \frac{\Delta f_{SH}}{2}; f_0 + \frac{\Delta f_{SH}}{2} \right]$	0	∞

In order to sustain the rectangular shape of the drain current, and thus a high efficiency, the reconstruction filter has to provide a short-circuit out of band for the spectrum of a one-bit modulator, which will, at the filter input, demand an optimal load in pass-band and a short for all other frequencies from DC to infinity. The lumped-element filter LC in Fig. 2.3.2 can be considered as an ideal output circuit for the CMCS PA driven by a $\Delta\Sigma M$. The frequency spectrum of the drain current lying above f_0 is shorted by a shunt capacitor, and below f_0 - by a shunt inductor. A similarly configured current mode class-D PA demands short-circuiting for only high-order odd harmonics of the drain currents [55]. In practice this means that a class-S PA can be tested in a class-D regime without exchanging the reconstruction filter.

Because of the leakage current through realistic circuit elements, perfect short conditions are impossible to achieve. A value of $|S_{23}| \geq 0.9$ was specified as a sufficient short-circuit, which can be recalculated into limitation of the differential-mode impedance out-of-band as a tenth of differential-mode impedance in-band (Eq. 3.2.6). Ideally, these conditions should be reached at an offset of Δf , but in reality the offset was extended up to $\Delta f_{SH} = 200$ MHz in the case of a centre frequency of 450 MHz and 300 MHz for that of 900 MHz. These out-of-band requirements can be formulated as:

$$f \notin \left[f_0 - \frac{\Delta f_{SH}}{2}; f_0 + \frac{\Delta f_{SH}}{2} \right] : \quad \begin{aligned} Z_{diff} &\leq 0.1 \cdot Z_{diff}(f_0) \\ Z_2 &= Z_3 \end{aligned} \quad (3.2.6)$$

But at the same time the out-of-band common-mode impedance has to be equal to infinity:

$$f \notin \left[f_0 - \frac{\Delta f_{SH}}{2}; f_0 + \frac{\Delta f_{SH}}{2} \right] : \quad \begin{aligned} Z_{com} &= \infty \\ Y_2 &= Y_3 = 0 \end{aligned} \quad (3.2.7)$$

An ideal lossless filter, providing ideal short-circuiting between the filter pins, can be described by *out-of-band* input impedances in Table 3.2.1 or by the fol-

lowing S^M -matrix:

$$S^M = \begin{pmatrix} 1 & 0 & 0 \\ 0 & -1 & 0 \\ 0 & 0 & 1 \end{pmatrix}. \quad (3.2.8)$$

In this section the constraints on the reconstruction filter impedances have been described in and out of band, in order to provide optimal operating conditions for the MMICs and to keep the rectangular form of the drain currents. The analysis presented here is essential to the maintenance of a high system efficiency. The requirements mentioned above concern only to a current mode class-S configuration. For a voltage mode configuration, a two-port reconstruction filter is appropriate, the requirements for which need to be specified, so that the rectangular shape of the drain voltages is maintained. These requirements can be found by the duality principle.

3.3 Filter terminations

Turning to the in-band behaviour: as mentioned above, the RF choke being, as it is, under the supply voltage acts like current sources. In these circumstances, the reconstruction filter has to be Singly Terminated (ST) with resistor termination on the antenna side and infinite internal impedance current generator on the final stage side. Any two-port filter can be easily turned to a

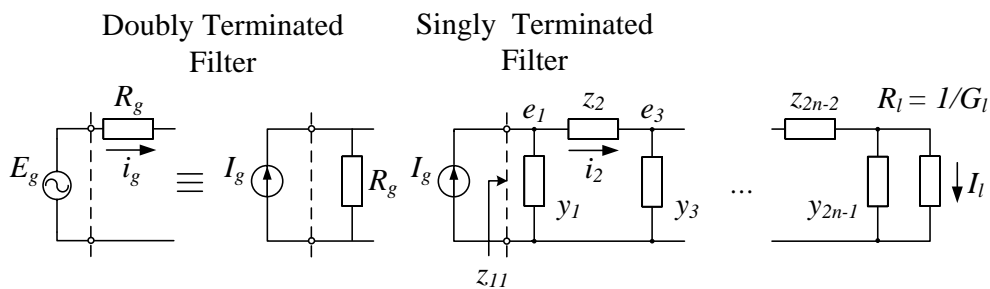


Figure 3.3.1: Doubly and singly terminated filter structures. E_g denotes the electromotive force of the generator, e_i and i_i are the corresponding node potentials and currents, and y_i and z_i are the partial immittances of a reactive ladder network [8].

four-port device as shown in Fig. 3.4.1 (or to a three-port filter by employing a transformer). For this reason, generalised structures of ST and DT (Doubly Terminated) filters with the order $N = 2n - 1$, where n is a positive integer, can be considered here, as depicted in Fig. 3.3.1. Firstly, an input impedance z_{11} is analysed: in the case of balanced filters this will be replaced by a differential-mode input impedance Z_{diff} .

The DT filter design based on power matching ($R_g = R_l$) cannot be used for ST structures, because of the zero impedance of a voltage source (or infinite impedance of a current source). In other words, the input reflection coefficient of ST filter structures would be $\Gamma = \pm 1$, which would obviously lead to the interpretation that no power could be delivered to the load. The impact of a single termination on the design of filters was therefore investigated. The element values of ST low-pass prototype LC ladders, obtained by the network synthesis method (Darlington's synthesis method) are described in [74] and tabulated in [12]. As opposed to DT filters, where half of the generator power is absorbed in the load R_l and the other half is dissipated in the internal generator resistance R_g , in ST filters (assumed to be lossless), the total generator power is absorbed in the load:

$$\begin{aligned} P_l &= P_g, \\ |I_l|^2 \cdot R_l &= |I_g|^2 \cdot \text{Re}(z_{11}), \end{aligned} \quad (3.3.1)$$

where I_g and I_l are the amplitudes of input and load currents respectively, and z_{11} denotes the complex-valued input impedance of the ladder network, as defined in Fig. 3.3.1 [12]. Eq. 3.3.1 illustrates that the output power is determined entirely by z_{11} , the frequency dependence of which reflects the desired filter transmission characteristics, e.g., Butterworth, Chebyshev, etc. The power transfer function representing the insertion losses (L_0) in an ST filter can be expressed like [12]:

$$L_0 = 20 \cdot \log_{10} \left| \frac{I_l}{I_g} \cdot \sqrt{\frac{R_l}{\text{Re}(z_{11})}} \right|. \quad (3.3.2)$$

In order to analyse ST and DT filters, the network parameters are described using a symbolic algorithm - the cumulant (also known as continuant) [8]. It is important to point out that normalised Laplace and Fourier transforms are applied here. The Laplace transform can be mapped onto the Fourier transform by replacing the complex frequency p by $p = j \cdot \omega$, or in case of normalised frequencies by:

$$P = j \cdot \Omega, \quad (3.3.3)$$

where $\Omega = \frac{\omega}{\omega_0}$ and consequently $P = \frac{p}{\omega_0}$.

The ST ladder structure in Fig. 3.3.1 was described in [8] by Kirchhoff's circuit laws

$$\begin{cases} I_g = e_1 \cdot y_1 + i_2 \\ 0 = -e_1 + i_2 \cdot z_2 + e_3 \\ 0 = 0 - i_2 + e_3 \cdot y_2 + i_4 \\ \vdots \\ 0 = \dots 0 - i_{2n-2} + e_{2n-1} \cdot (y_{2n-1} + G_l), \end{cases} \quad (3.3.4)$$

where i_i and e_i are current and voltage across the element i , and the coefficients z_i, y_i are the partial immittances. The partial immittances can be calculated for a low-pass filter as $z_i = L_i \cdot P$ and $y_i = C_i \cdot P$. The solution of the linear set of equations in Eq. 3.3.4 results in a tridiagonal matrix with a determinant Δ :

$$\Delta = \begin{vmatrix} y_1 & 1 & 0 & \dots & 0 & 0 \\ -1 & z_2 & 1 & \dots & 0 & 0 \\ 0 & -1 & y_3 & \dots & 0 & 0 \\ \vdots & \vdots & \vdots & \ddots & \vdots & \vdots \\ 0 & 0 & 0 & \dots & -1 & G_l \end{vmatrix} = (y_1, \dots, G_l), \quad (3.3.5)$$

which is entirely defined by the elements standing in the principal diagonal. The determinant in Eq. 3.3.5 can be represented as the cumulant (y_1, \dots, G_l) . In order to find the z-parameters, the voltages across the filter input and output have to be determined from the ratios of the associated minors to the determin-

ant:

$$\begin{aligned}
 \Delta_1 &= \begin{vmatrix} I_g & 1 & 0 & \cdots & 0 & 0 \\ 0 & z_2 & 1 & \cdots & 0 & 0 \\ 0 & -1 & y_3 & \cdots & 0 & 0 \\ \vdots & \vdots & \vdots & \ddots & \vdots & \vdots \\ 0 & 0 & 0 & \cdots & -1 & G_l \end{vmatrix} = I_g \cdot (z_2, \cdots G_l), \\
 e_1 &= \frac{\Delta_1}{\Delta} = \frac{I_g \cdot (z_2, \cdots G_l)}{(y_1, \cdots G_l)}, \\
 \Delta_{2n-1} &= \begin{vmatrix} y_1 & 1 & 0 & \cdots & 0 & I_g \\ -1 & z_2 & 1 & \cdots & 0 & 0 \\ 0 & -1 & y_3 & \cdots & 0 & 0 \\ \vdots & \vdots & \vdots & \ddots & \vdots & \vdots \\ 0 & 0 & 0 & \cdots & -1 & 0 \end{vmatrix} = I_g, \\
 e_{2n-1} &= \frac{\Delta_{2n-1}}{\Delta} = \frac{I_g}{(y_1, \cdots G_l)}.
 \end{aligned} \tag{3.3.6}$$

The z-parameters - the input and transfer impedances z_{11} and z_{12} are sufficient for the synthesis of a symmetrical filter - and the voltage gain g_{12} can be found from Eq. 3.3.6:

$$\begin{aligned}
 z_{11} &= \frac{e_1}{I_g} = \frac{(z_2, \cdots G_l)}{(y_1, \cdots G_l)}, \\
 z_{12} &= \frac{e_{2n-1}}{I_g} = \frac{1}{(y_1, \cdots G_l)}, \\
 g_{12} &= \frac{e_{2n-1}}{e_1} = \frac{1}{(z_2, \cdots G_l)}.
 \end{aligned} \tag{3.3.7}$$

In the same way, the characteristics of the DT filter have been expressed in terms of cumulants and presented in Table 3.3.1. Clearly, all the parameters listed in Table 3.3.1 are frequency dependent.

Table 3.3.1: Parameters of the DT and ST filter structures from Fig. 3.3.1 [8].

ST filter	DT filter
$g_{12}^{ST} = \frac{1}{(z_2, \dots, G_l)}$	$g_{12}^{DT} = \frac{1}{(R_g, \dots, G_l)}$
$z_{11}^{ST} = \frac{(z_2, \dots, G_l)}{(y_1, \dots, G_l)}$	$z_{11}^{DT} = \frac{(R_g, \dots, G_l)}{(y_1, \dots, G_l)}$
$z_{12}^{ST} = \frac{1}{(y_1, \dots, G_l)}$	$z_{12}^{DT} = \frac{1}{(y_1, \dots, G_l)}$

Turning now to the analysis of the input impedances, both ST and DT filters will be considered in their general form. In order to exclude the resistive load element G_l , the input impedance z_{11}^{ST} from Eq. 3.3.7 can be expanded by the last term into the following form [8]:

$$z_{11}^{ST}(P) = \frac{(z_2, \dots, G_l)}{(y_1, \dots, G_l)} = \frac{(z_2, \dots, y_{2n-1}) + (z_2, \dots, z_{2n-2})}{(y_1, \dots, y_{2n-1}) + (y_1, \dots, z_{2n-2})}, \quad (3.3.8)$$

where

$$\begin{aligned} (z_2, \dots, y_{2n-1}) &= E_n(P) \text{ is an even part of the numerator,} \\ (z_2, \dots, z_{2n-2}) &= O_n(P) \text{ is an odd part of the numerator,} \\ (y_1, \dots, z_{2n-2}) &= E_d(P) \text{ is an even part of the denominator,} \\ (y_1, \dots, y_{2n-1}) &= O_d(P) \text{ is an odd part of the denominator.} \end{aligned} \quad (3.3.9)$$

After replacing the cumulants according to Eq. 3.3.9, the input impedance from Eq. 3.3.8 can be reduced to:

$$z_{11}^{ST}(P) = \frac{[E_n(P) + O_n(P)] \cdot [E_d(P) - O_d(P)]}{E_d^2(P) - O_d^2(P)}. \quad (3.3.10)$$

According to Eq. 3.3.1, the real part of the input impedance is of our main interest and can be calculated from Eq. 3.3.10 like:

$$\operatorname{Re} \left[z_{11}^{ST}(P) \right] = \frac{E_n(P) \cdot E_d(P) - O_n(P) \cdot O_d(P)}{E_d^2(P) - O_d^2(P)}. \quad (3.3.11)$$

According to the general calculus of cumulants [8], the numerator of Eq. 3.3.11 will take the value of ± 1 :

$$E_n(P) \cdot E_d(P) - O_n(P) \cdot O_d(P) = (-1)^{n+1}. \quad (3.3.12)$$

The denominator in Eq. 3.3.11 presents the inverse of the squared transfer impedance and can be expressed in terms of the characteristic transfer function $F(P)$ as:

$$\frac{1}{|z_{12}^{ST}(P)|^2} = E_d^2(P) - O_d^2(P) = 1 - \epsilon^2 F^2(P), \quad (3.3.13)$$

where ϵ is the ripple factor. Switching to the Fourier transform, according to Eq. 3.3.3, the real part of the input impedance can be written as:

$$\operatorname{Re} \left[z_{11}^{ST}(\Omega) \right] = \frac{(-1)^{n+1}}{1 + \epsilon^2 F^2(\Omega)}, \quad (3.3.14)$$

or, for $\Omega \leq 1$, can be approximated by:

$$\operatorname{Re} \left[z_{11}^{ST}(\Omega) \right] \approx (-1)^{n+1}. \quad (3.3.15)$$

Local extrema of the function $\operatorname{Re} \left[z_{11}^{ST}(\Omega) \right]$ can be found by Fermat's theorem [75]. The first derivative of the function in Eq. 3.3.15 is identically zero over the entire pass-band, meaning that the input impedance of an ST filter keeps the constant value of unity and displays no maxima at all. These assertions can be proved on the design of an ST filter. The computed results are presented in Fig. 3.3.2: input resistance (red solid curves), its first derivative (blue solid curves), and analytically derived results (blue dotted curves) for a 4th-order Butterworth low-pass filter [76]. As expected, the filter has a constant in-band

input resistance smoothly decreasing at the edges of the pass-band. Both the computed and the analytically derived first derivatives are consistent with a single broad maximum of $Re [z_{11}^{ST}(\Omega)]$.

A similar analysis can be applied to DT filters. As z_{11}^{DT} from Table 3.3.1 depends on both parameters R_g and G_l , the technique used for Eq. 3.3.8-3.3.10 becomes so complicated as to be unreasonable. Instead the element values g_i can be computed from the following equation, coupling the cumulant and the characteristic transfer function $F(P)$ [8]:

$$(-R_g + y_1, \dots, G_l) = -\frac{\epsilon F(P)}{K}, \quad (3.3.16)$$

where $K = \frac{1}{\sqrt{4R_g G_l}}$ takes into account the power transfer between generator and load; and ϵ is the ripple factor. In the particular case of maximum power transfer, when $R_g = G_l = 1$, and $K = 1/2$, expanding the cumulant on the left-hand side of Eq. 3.3.16 to first order gives

$$-(y_1, \dots, 1) + (z_2, \dots, 1) = -2 \cdot \epsilon F(P). \quad (3.3.17)$$

In the same way, the voltage gain can be decomposed by its first term into:

$$(y_1, \dots, 1) + (z_2, \dots, 1) = \frac{1}{g_{12}^{DT}(P)}. \quad (3.3.18)$$

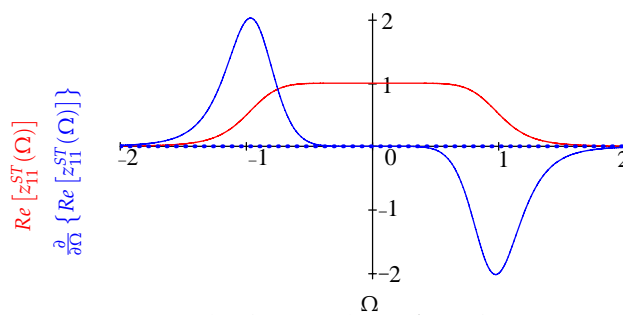


Figure 3.3.2: Input resistance (red curves), its first derivative as computed (blue solid curves) and as analytically derived (blue dotted curves) for a 4th-order ST Butterworth filter.

According to the definitions given in Table 3.3.1 and Eqs. 3.3.18-3.3.17, the input impedance of an DT filter can be expressed as:

$$z_{11}^{DT}(P) = 2 \left[1 - z_{12}^{DT}(P) \cdot \epsilon F(P) \right]. \quad (3.3.19)$$

The transfer impedance $z_{12}^{DT}(P)$, expanded by its last term, can be expressed by its even $E(P)$ and odd $O(P)$ parts:

$$\frac{1}{z_{12}^{DT}(P)} = (y_1, \dots, y_{2n-1}) + (y_1, \dots, z_{2n-2}) = E(P) + O(P). \quad (3.3.20)$$

According to Eq. 3.3.13, the input impedance Eq. 3.3.19 can be presented as:

$$z_{11}^{DT}(P) = 2 \left\{ 1 - \frac{\epsilon F(P) \cdot [E(P) - O(P)]}{\sqrt{1 - \epsilon^2 F^2(P)}} \right\}. \quad (3.3.21)$$

Switching to the Fourier transform, Eq. 3.3.21 can be approximated, $\Omega \leq 1$, by:

$$z_{11}^{DT}(\Omega) \approx 2 \{ 1 - \epsilon F(\Omega) \cdot [E(\Omega) - O(\Omega)] \}. \quad (3.3.22)$$

The local extrema of the function $z_{11}^{DT}(\Omega)$ can be found by

$$\begin{aligned} \frac{\partial}{\partial \Omega} \left\{ \text{Re} \left[z_{11}^{DT}(\Omega) \right] \right\} &\approx \frac{\partial}{\partial \Omega} [\epsilon F(\Omega) \cdot O(\Omega)] = 0 \text{ if } n \text{ is odd,} \\ \frac{\partial}{\partial \Omega} \left\{ \text{Re} \left[z_{11}^{DT}(\Omega) \right] \right\} &\approx \frac{\partial}{\partial \Omega} [\epsilon F(\Omega) \cdot E(\Omega)] = 0 \text{ if } n \text{ is even.} \end{aligned} \quad (3.3.23)$$

The analysis of the polynomial equation Eq. 3.3.23 shows that [76]:

1. Eq. 3.3.23 can be adopted for any type of transfer function, e.g., Butterworth, Chebyshev.
2. The polynomial is of order $2n - 1$.
3. All $(2n - 1)$ roots of the polynomial are real numbers.
4. For a Butterworth transfer function, at least $(n - 1)$ roots will be different from zero.

5. The input impedance $Re [z_{11}^{DT}(\Omega)]$ is a non-constant function of Ω and displays maxima in the pass-band.

Applying Eq. 3.3.23 to the design of an DT filter, the computed results are presented in Fig. 3.3.3: Input resistance (red solid curves), its first derivative (blue solid curves), and analytically derived functions (blue dotted curves) for a 4th-order Butterworth (in panel a) and a 5th-order Chebyshev filter with 0.01 dB ripple (in panel b). The analytically derived result agrees well with the computed values. Most importantly, both curves display identical crossings of the Ω -axis. As expected, the filter with Butterworth transfer function has four non-vanishing roots, half of which are a mirror image in the negative frequency range, while the other five roots are equal to zero. These non-vanishing roots result in in-band ripples and maxima at the borders of the pass-band. The Chebyshev filter shows the designed pass-band ripple, which manifests itself also in the input impedance, but also significant maxima at the edges of the pass-band. From the analysis and, especially a comparison of Fig. 3.3.2 and Fig. 3.3.3, it can be generalised that the tendency of these maxima in the input resistance at the pass-band borders is typical of DT filters. Moreover, calculations showed that the location of the maxima depends on the filter order and the specific type of transfer function. For example, for a 5th-order Butterworth

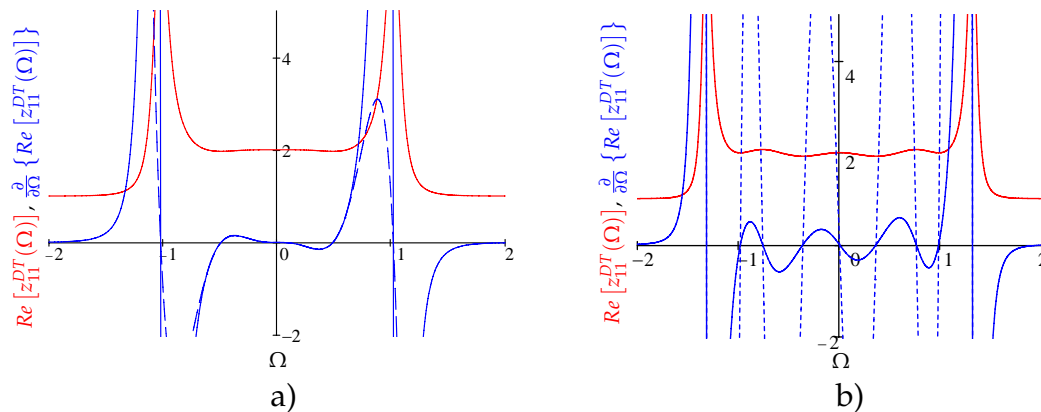


Figure 3.3.3: Input impedance (red curves), its first derivative as computed (blue solid curves) and as analytically derived (blue dotted curves) for a 4th-order DT Butterworth filter (in panel a) and a 5th-order DT Chebyshev filter (in panel b).

filter, the pronounced maximum appears at $\Omega = 1.18$, while for the Chebyshev filter it is shifted to $\Omega = 1.31$. Another feature of this calculation method is a vertical offset by unity in the input resistances in Fig. 3.3.3, which can be explained by the reference plane of measuring z_{11} in Fig. 3.3.1, which is shifted before R_g . This offset will not be observed in test measurements, because the reference plane is usually placed behind R_g .

3.4 Singly terminated filters

3.4.1 Computation and measurement techniques

The ST filters which are considered in this study are of the type synthesised for the current source with infinite impedance. It is not possible to measure the transmission characteristics of such filters without some degree of uncertainty with a typical network analyser, because its inner impedance is finite, $R_g = 50 \Omega$. However, a network analyser can be employed for measuring the input impedance of the ST filters:

$$z_{11} = R_g \frac{1 + \Gamma_{11}}{1 - \Gamma_{11}}, \tag{3.4.1}$$

where Γ_{11} is an input reflection coefficient. In order to determine the measurement technique for the ST filters, it is necessary to analyse both ST and DT filters at the same time. For this purpose, two ST and DT third-order BPFs

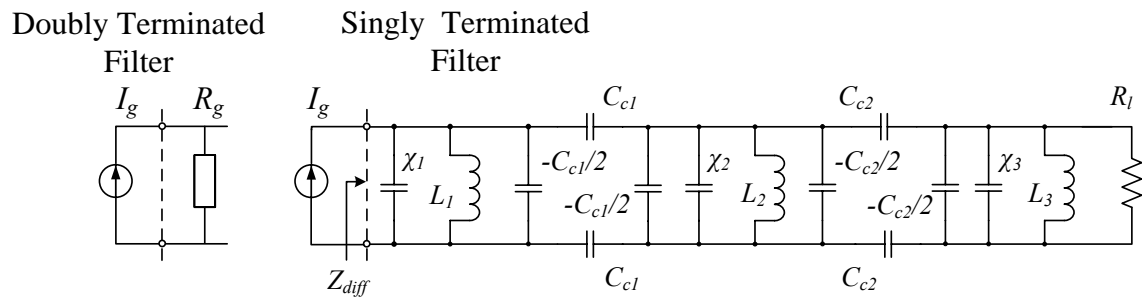


Figure 3.4.1: Third-order ST and DT BPFs with admittance inverters.

with a Butterworth transfer function were designed, as shown in Fig. 3.4.1. The g-elements for their low-pass prototypes are listed in Table 3.4.1 [12]. After frequency transformation ($f_0 = 900$ MHz and $\Delta f = 26$ MHz) and impedance scaling ($R_g = R_l = 50 \Omega$ for the DT filter and $Re(Z_{diff}(\omega_0)) = R_l = 50 \Omega$ for the ST filter), the LC elements for both filters can be found from [12]:

$$\begin{aligned}
 R_0 &= \frac{R_l}{R_l'} \\
 \chi_i &= \frac{1}{\Delta\omega} \frac{g_i}{R_0'} \\
 L_i &= \frac{1}{\omega_0 \cdot \chi_i}, \\
 C_{ci} &= 2 \cdot \frac{\Delta\omega}{\omega_0} \sqrt{\frac{\chi_i \cdot \chi_{i+1}}{g_i \cdot g_{i+1}}}, \\
 C_i &= \chi_i - C_{ci}/2 - C_{c(i-1)}/2.
 \end{aligned} \tag{3.4.2}$$

For the inductors L_i , being the most critical circuit elements, the S-parameter blocks of the Coilcraft components were used [77]. Both filters were simulated in Agilent's Advanced Design System (ADS) software, firstly with their ideal elements and then with the realistic S-parameter blocks. The simulation results

Table 3.4.1: Element values for the singly and doubly terminated third-order filters with a Butterworth transfer function for $\omega' = 1$ [12].

g_i	ST filter	DT filter
g_0	∞	1
g_1	1.5	1
g_2	1.333	2
g_3	0.5	1
g_4	1	1

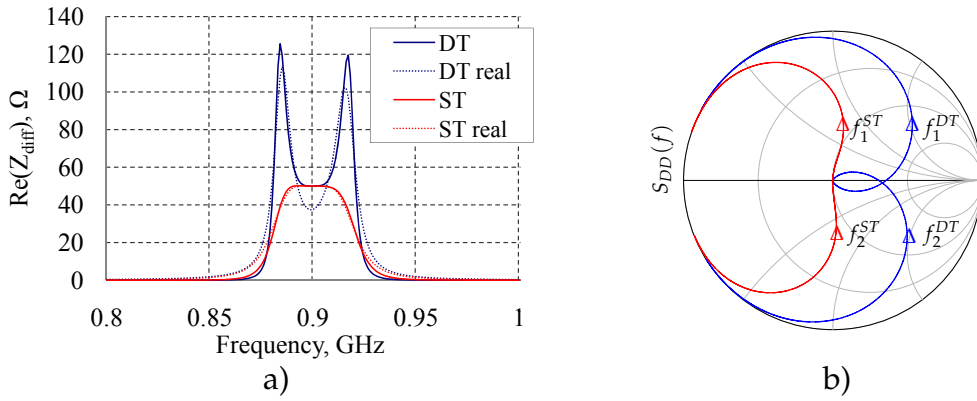


Figure 3.4.2: Input resistances (in panel a) and reflection coefficients for a differential mode of excitation (in panel b) of the Butterworth third-order DT (blue curves) and ST filters (red curves). The filters on ideal elements are traced by solid lines, on real elements - by dotted lines. The frequencies marked on the Smith Chart are $f_1^{ST} = 0.915$ GHz, $f_2^{ST} = 0.885$ GHz, $f_1^{DT} = 0.917$ GHz, and $f_2^{DT} = 0.883$ GHz

are presented in Fig. 3.4.2. The input resistance (see Fig. 3.4.2,a) of the DT filter is equal to 50 Ω at the centre frequency only, and rises sharply to 120 Ω at the pass-band edges. In contrast, the ST filter displays constant input impedance of 50 Ω over the whole pass-band. This result was expected, and is explained by the filter termination. In order to analyse an input reactance, the filter responses are plotted in the Smith Chart, shown in Fig. 3.4.2,b. Over the pass-band, the

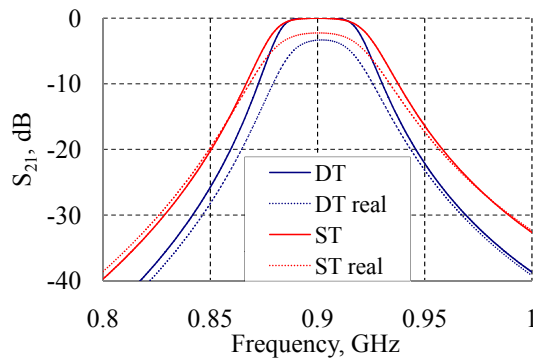


Figure 3.4.3: Transmission coefficient of the third-order DT filter (blue curves) and ST filter (red lines) excited by a current source with a source resistance of $R_g = 50 \Omega$. The filters based on ideal elements are represented by solid curves and on real elements (including losses) by dotted curves.

reflection coefficient of the ST filter moves on the circuit of $Re(z) = 1$, crossing a reference line of $Im(z) = 0$, but out-of-band, the input reactance rises slightly. In the DT filter, the input reactance behaves similarly, with the difference that it has higher values out-of-band, which may result in high reactive currents and voltages at the transistors. The filters were driven by a current generator with an R_g of 50Ω , in order to simulate a realistic network analyser. Both filters have maximally flat filter response over the different bandwidths, as illustrated in Fig. 3.4.3. As had been intended, the DT filter proved to have a 3 dB bandwidth of 26 MHz. The ST filter, similarly designed, provided a 15 % broader bandwidth, 30 MHz. The broadening of the bandwidth in the ST filter was observed in all the ADS simulation and on actual measurement. The uncertainty of both the simulation and the measurement conditions is the explanation.

The comparative analysis of ST and DT types presented shows that the filter termination is crucial for the performance of a switching amplifier. It is possible for ST filters to have constant input resistance in-band and, consequently, to provide constant output power of a current mode class-S PA system. In contrast, DT filters are characterised by pronounced maxima of their input impedance, which can result in the high drain voltages, potentially damaging the switching transistors. This assertion was proven by simulation. A typical network analyser can be employed for measuring input impedance of the ST filters. However, it is so far impossible to measure the transmission response of the ST filters without any uncertainty. The bandwidth here will be broader than measured for current or voltage transmission.

3.4.2 Impedance transformation

It has been made clear above that in order to provide the optimal power conditions for the GaN HEMTs it is necessary for a reconstruction filter to have optimal input impedance in-band and to transform it to an antenna. This necessitates an ST reconstruction filter with impedance transformation. The impedance transforming DT filters can be synthesised using general synthesis methods. The g-elements for these filters were obtained in [78] and tabulated

in [79, 80]. The g -elements for the impedance transforming ST filters can also be found using general synthesis [8], but each particular case has to be recalculated from the DT filter (or from the ST filters without impedance transformation). Another approach assumes the use of the J- and K-inverters as impedance transformers [81]. However, it is necessary to investigate such structures in terms of input impedances in-band. Thus, there is no simple calculation method which can be applied to the impedance transforming ST filters. In this section, an approach based on impedance scaling for such filters will be proposed.

To take again the ST filter from Fig. 3.3.1: it can be also described by its input and transfer admittances, y_{11} and y_{12} , and gain voltage, g_{12} , [8] as:

$$\begin{aligned} g_{12}^{ST} &= \frac{1}{(z_2, \dots, G_l)',} \\ y_{12}^{ST} &= \frac{1}{(z_2, \dots, z_{2n-2})',} \\ y_{11}^{ST} &= \frac{(y_1, \dots, z_{2n-2})}{(z_2, \dots, y_{2n-1})}. \end{aligned} \quad (3.4.3)$$

As can be seen, both LC circuit characteristics, y_{12}^{ST} and g_{12}^{ST} , are independent on y_1 . This effect is explained by the fact that the circuit is driven by an ideal voltage source - this is described in [12] - and the parallel first resonator is shorted by zero impedance of the generator. At the same time, the input admittance is defined by y_1 , which can be tuned without destruction of the other filter characteristics. However, if such a ST filter is driven by an ideal current source, the first parallel element y_1 can be taken as inner impedance of this source. Thus, if impedance transformation is to be achieved, impedance scaling will be necessary. This study proposes an approach in which the g_i -elements for ST prototypes (tabulated in [82]) are used, and the following impedance scaling is to be utilised:

$$R_1 = Re(Z_{diff}(\omega_0)), \quad R_{i|i>1} = R_l. \quad (3.4.4)$$

In this piece of research, the first resonator will have an impedance of $R_{|Opt|_{class-s}}$ while the others will be scaled to the 50Ω of an antenna. Using the calculation technique from the previous section, the lumped elements of an ST filter are:

$$\begin{aligned}\chi_i &= \frac{1}{\Delta\omega} \frac{g_i}{R_i}, \\ L_i &= \frac{1}{\omega_0 \cdot \chi_i}, \\ C_{ci} &= 2 \cdot \frac{\Delta\omega}{\omega_0} \sqrt{\frac{\chi_i \cdot \chi_{i+1}}{g_i \cdot g_{i+1}}}, \\ C_i &= \chi_i - C_{ci}/2 - C_{c(i-1)}/2,\end{aligned}\tag{3.4.5}$$

which show that the impedance scaling applied affects only the element values of the first resonator and the first admittance inverter, which constitutes an advantage enabling the ST filter design to have tunable input impedance.

In order to verify the calculation method proposed, three lossless Butterworth ST filters were designed and simulated. The filters transform their input impedances of 5Ω , 100Ω and $1 \text{ k}\Omega$ to the 50Ω of an antenna, corresponding to transformation ratios of $r = 10, \frac{1}{2}$ and $\frac{1}{20}$, respectively. The element values of the filters were calculated using Eq. 3.4.5. The filters designed were simulated under different driving conditions. Firstly, an ideal current source, with infinite inner impedance, was applied. It is important to note that ADS simulation whether with an ideal current source or with an ideal voltage source gives the same results. Measured input impedances are presented in Fig. 3.4.4,a. The filters have constant input impedances, which are identical in shape, but scaled to different levels. Secondly, in order to estimate the bandwidths, the respective filters were driven by the power source with R_g of 5Ω , 100Ω and $1 \text{ k}\Omega$. These simulation results are presented in Fig. 3.4.4,b. Because the filters were matched, they have perfect transmission over the identical pass-bands. The bandwidth of the filters is 47 MHz and broader than had been built in to the calculations.

This section has presented a novel approach for ST filter design with impedance transformation. It uses known g-parameters for conventional ST filters and necessitates special impedance scaling. As the method proposed has been

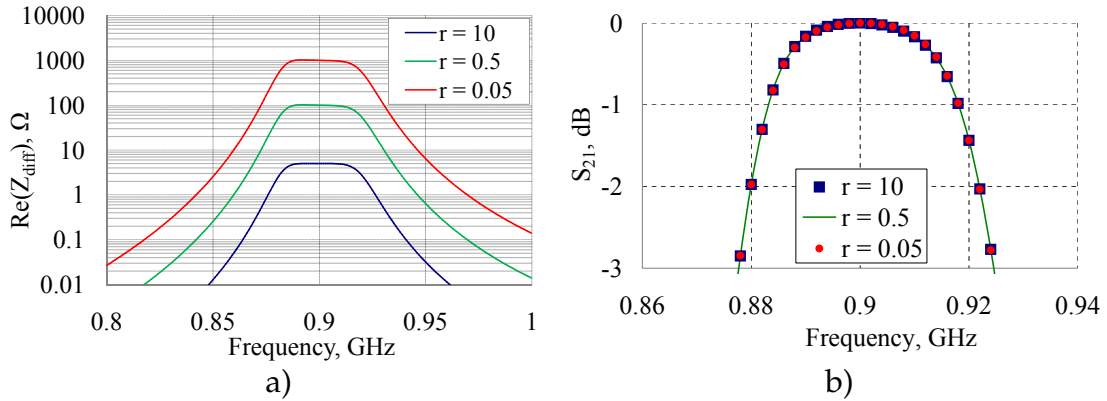


Figure 3.4.4: The input resistance (in panel a) and transmission coefficient (in panel b) of the Butterworth ST filters with impedance transformation ratios of $r = 10$ (blue line), $\frac{1}{2}$ (green line) and $\frac{1}{20}$ (red line).

verified in ADS simulation and shows good results, it will be used in the following chapters.

3.5 Specifications for a reconstruction filter

For the GaN HEMTs with 2 mm and 4 mm gate (supplied by FBH in Berlin, Germany), the specifications are presented in Table 3.6.1.

3.6 Conclusion of the requirements for reconstruction filters

The requirements for a reconstruction filter for a CMCS PA system have been the subject of this chapter can be described in summary as follows.

1. Because it operates in modern BTSs, it is necessary for the reconstruction filter to have low insertion loss, to handle peak power of 100 W, and to comply with an emission mask defined by the 3GPP standard. In order to shape the noise-like $\Delta\Sigma$ spectrum or periodic parasitic harmonics in the PLM spectrum, the filter is required to have wide stop-band. Moreover,

significant reduction in the cost and complexity of the whole system will be possible if the reconstruction filter is tunable between the operating frequency bands.

2. For a CMCS PA system, a reconstruction filter with a balanced input is required. This balanced input can be excited either by differential mode or by common mode. In order to sustain the rectangular shape of the drain current, and, with it, high efficiency, the reconstruction filter should have low-ohmic, out-of-band input impedance for the differential mode and high-ohmic for the common mode.
3. Because the final stage of CMCS PAs acts like a current source with infinite internal impedance, a singly terminated filter is required. Only the ST filter can have a constant in-band input resistance and, consequently, provide constant output power of the whole system. Under the same driving conditions an DT filter will have pronounced maxima in its input resistance, which can result in high drain voltages, potentially damaging the switching transistors.
4. To measure the input impedance of ST filters, a typical network analyser with finite internal impedance can be employed. In all the other measurements, it will, however, give inaccurate results.
5. For the GaN HEMTs to have optimal power conditions, it is necessary for a reconstruction filter to have an optimal input impedance in-band and to transform it to an antenna. Here, an ST filter with impedance transformation is required. A novel approach for these filters has been proposed and vindicated in ADS simulation.

In order to fulfil the requirements summarised above, several novel architectures for the reconstruction filters and their subsequent measurement will be presented in the following chapter.

3.6 Conclusion of the requirements for reconstruction filters

Table 3.6.1: Specification for the reconstruction filter for a CMCS PA system, operating with the following transistors

Filter Parameter	-	GaN 4 mm	GaN 2 mm
Centre frequency	f_0	450 MHz	900 MHz
3-dB bandwidth	Δf	10 MHz	20 MHz
Second pass-band	f_{SPB}	$\geq 5 \cdot f_0$	$\geq 5 \cdot f_0$
Insertion loss	L_0	≤ 1 dB	≤ 1 dB
Power handling	$\hat{P}_{RF_{in}}$	100 W	100 W
Antenna port impedance	R_l	$(50 + 0j) \Omega$	$(50 + 0j) \Omega$
Input impedance in-band for the differential mode of excitation	Z_{diff}	$(65 + 0j) \Omega$	$(130 + 0j) \Omega$
Input impedance out-of-band for the differential mode of excitation	Z_{diff}	$(6.5 + 0j) \Omega$	$(13 + 0j) \Omega$
Input impedance in-band for the common mode of excitation	Z_{com}	∞	∞
Input impedance out-of-band for the common mode of excitation	Z_{com}	∞	∞
Offset to achieve short out-of-band	Δf_{SH}	200 MHz	300 MHz

4 Design and implementation of reconstruction filters

This chapter presents the design and implementation of reconstruction filters, so that they fulfil all the requirements mentioned in the previous chapter. The filter technologies for wireless base stations will first be analysed and then a tunable high-power coaxial comb-line filter, which serves as a basis for the further design, will be presented. The third section will propose several alternative architectures of a balanced input comb-line filter, all of which successfully combine the properties of a balun and a comb-line filter, and are compatible with the $\Delta\Sigma$ -modulated signals. The measurement results are given for all the architectures and a critical analysis follows.

4.1 Filter technologies for wireless base stations

The microwave filters employed for application in BTSs can be divided into a number of main categories [83]: coaxial filters with cavity resonators and filters with dielectric resonators. There is also some potential for microwave filters using metamaterials. In order to make a choice, it is necessary to analyse all these technologies.

Dielectric resonators, proposed as early as 1960, are today temperature-stable and commercially available at a reasonable price. Because the dielectric losses grow with frequency, the product $Q \times f$ is a basic property of each dielectric material (Q is here quality-factor of the resonator). In dielectric filter design, there is a trade-off between insertion loss and compactness, associated with dielectric permittivity ϵ_r and loss tangent $\tan(\delta)$. However, these filters

have the disadvantage of spurious resonances close to the centre frequency, a significant issue for the current application. The state of the art in the dielectric filters has been presented in [9], where the dielectric filter with dual-mode resonators had an unloaded quality factor of 10,000, and a compact structure measuring $40\text{ mm} \times 40\text{ mm} \times 80\text{ mm}$ in size (see Fig. 4.1.1,a). However, in this instance the first spurious resonance appears already at 2.5 GHz, as shown in Fig. 4.1.1,b. It is possible to apply a special technique to improve the spurious features, giving a spurious-free window of 600 MHz for a centre frequency of 2.7 GHz [84], but again this is not enough for the current application.

Because they have unusual properties otherwise unavailable, the *microwave filters made of metamaterials* have attracted great interest to date. The theory of metamaterials was expounded in the 1960's by Prof. Veselago, who made an assumption that there were materials with both negative permittivity and permeability [85]. Today many research groups world-wide are working in this area, creating "super-lenses" and "invisible materials". As an example, a third-order BPF on high Q-factor suspended stripline designed for BTS application [10] is shown in Fig. 4.1.2,a. The filter has insertion losses of 0.76 dB at a centre frequency of 932.5 MHz and a 3-dB bandwidth of 50 MHz. The filter was far from compact, measuring $330\text{ mm} \times 370\text{ mm} \times 40\text{ mm}$ in size, and cumbersome to manufacture, both in its housing technology and in the complexity of the hybrid elements used.

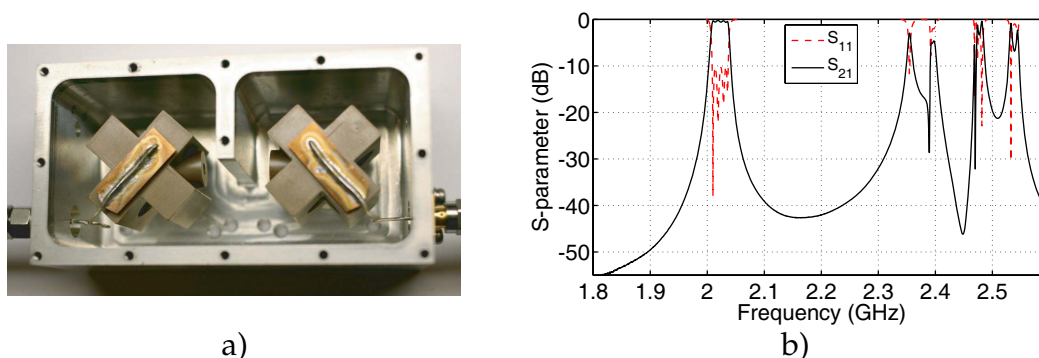


Figure 4.1.1: Photo of the 4-pole filter with two dielectric dual-mode resonators (in panel a) and measured spurious performance (in panel b) [9].

Microwave filters with cavity resonators, e.g. comb-line filters or interdigital filters, are frequently used for BTS application because they have a high quality factor and their manufacture is simple and cheap. To achieve homogeneous current density and, consequently, lower insertion loss, coaxial structures are to be preferred to planar ones. To take the interdigital filter first: this is usually employed for applications, in which it is necessary for the filter to have a wide bandwidth. Its resonators consist of quarter-wavelength TEM elements, which are short-circuited at the one end and open at the other. In contrast, the comb-line filter (CLF) is attractive for applications which demand a filter type with a wide stop-band. As it is possible to manufacture both filters from a single metal block without any support material, it has the advantages of both low insertion loss and low cost. As an example, the typical duplex tenth-order CLF for the E-GSM 900 Alcatel-Lucent BTS, presented in [10], is shown in Fig. 4.1.2,b. The silver plated resonators have a high Q-factor of 5,000, but here, again, the filter was relatively cumbersome, measuring $360\text{ mm} \times 240\text{ mm} \times 50\text{ mm}$ in size. However, for this reconstruction filter it is possible to reduce the geometrical constraints and, at the same time, the electrical constraints, by employing a coaxial CLF, with its shortened resonators and broad stop-band. This type of microwave filter will be considered in detail in the following section.

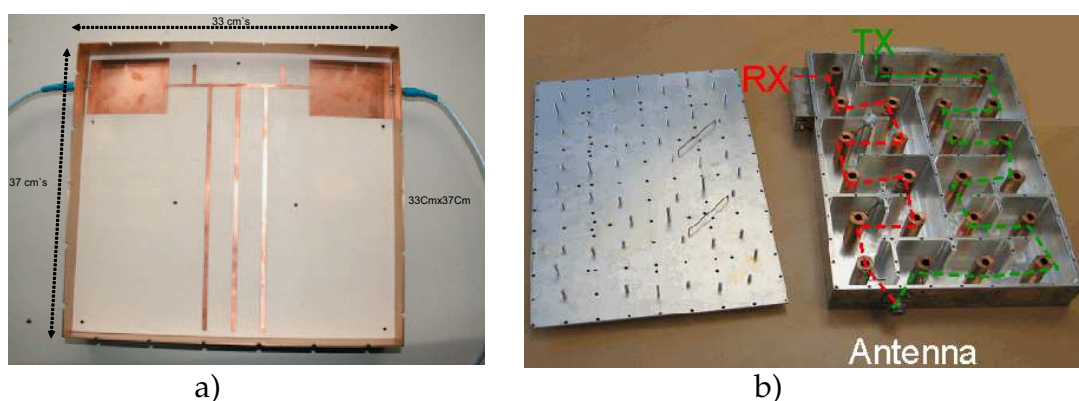


Figure 4.1.2: The third-order filter on metamaterials (in panel a) [10] and the duplex comb-line filter supplied by Alcatel-Lucent (in panel b) [11].

4.2 Coaxial comb-line filter design

Comb-line band-pass filters are well-known as a type [12]. A planar implementation of a CLF with distributed capacitances is also known as a stepped-impedance resonators filter. Fig. 4.2.1 is a general illustration of the resonators of a CLF, $1 \dots N$, consisting of TEM-mode transmission line elements with a physical length l and an electrical length $\theta_0 = 2\pi l/\lambda_0$. They are short-circuited at one end and have lumped capacitances, $C_1 \dots C_N$, between the other ends and ground. The coupling between the resonators is achieved by a fringing field between the TEM elements. The input and output lines, 0 and $N + 1$, can provide impedance matching to the first and last resonators. Because of the lumped capacitors at the ends of the resonators $C_1 \dots C_N$, it is possible for the TEM elements to be shorter than $\lambda_0/4$ at the centre frequency, and for a CLF to be very compact. Moreover, the second pass-band f_{SPB} occurs at the frequency where an electrical length of the TEM elements is somewhat longer than half of wavelength:

$$f_{SPB} = f_0 \cdot \lambda_0 / (2 \cdot l). \quad (4.2.1)$$

Thus, it is possible to design a CLF with a very broad stop-band. In order to achieve both compactness and broad stop-band, it would be logical for the TEM elements to be as short as possible. Another advantage of a CLF is low insertion loss. This be achieved if the CLF is fabricated without use of dielectric support material. What is used in this study is an equivalent circuit of a CLF (shown in

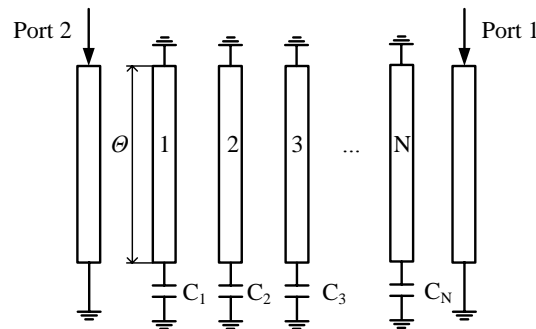


Figure 4.2.1: Schematic layout of a comb-line band-pass filter in stripline form [12].

Fig. 3.4.1), the lumped elements of which can be found by the technique presented in [12].

4.2.1 Quality factor, transfer function and filter order

It is known that the microwave filters derive their transmission characteristics from the lumped-element, low-pass prototypes used in their design. A variety of prototypes has been proposed for the microwave filter application, e.g. Butterworth, Chebyshev, Gaussian and so on [12]. Each prototype has its typical filter response. The choice will be dictated by the priorities for the reconstruction filter design. As has been mentioned, the major priority is a high degree of linearity of the PA system as a whole and of the filter in particular. In mobile communications, linearity is characterised by the EVM and can be approximated as the root sum of squares of the transmission coefficient magnitude and phase contributions [86]:

$$EVM \approx \sqrt{\langle (Mag(S_{D1}) - 1)^2 \rangle + \langle (Arg(S_{D1}) - \omega\tau_0 - \phi_0)^2 \rangle}, \quad (4.2.2)$$

where S_{D1} is a transmission coefficient of a differential mode of excitation, τ_0 is the fixed phase offset of the signal before filtering, ϕ_0 is the fixed delay value and the angle brackets denote the average values over the bandwidth of the signal. As seen, it is necessary for both the magnitude and the phase of the prototype to be constant in-band. There are two known prototypes with either maximally flat attenuation or with maximally flat time-delay. When both these prototypes had been analysed, the choice fell on the Butterworth filter with maximally flat frequency response.

It is also necessary for the filter to have a sharp rate of cutoff, which will be defined by the filter order. The filter order, in its turn, depends on both the filter used prototype and the Q-factor of the resonators (if insertion losses are limited). The Q-factor characterises the resonator's energy storage capability (the total energy stored in the resonator relative to the dissipated power per cycle). The unloaded quality factor Q_{UL} describes the power dissipated only

in the resonator per cycle and independent on coupling. Various methods of evaluating the unloaded quality factor have been proposed by Matthai, Levy, Snyder, and others [12, 87, 88]. For air-filled silver-plated coaxial resonators, all these methods will give numerically quite similar results, deviating only by about 20 %. For example, Levy established the quality factor of any normal (nonsuperconducting) metallic RF cavity as [87]:

$$Q_{UL} = \frac{\kappa \cdot b}{\sqrt{f_0}}, \quad (4.2.3)$$

where b is a linear dimension of the cavity in inches, f_0 is the resonant frequency in gigahertz, and κ is usually constant for any given type of cavities resonator of the order 1500 .. 3600. For example, for a comb-line silver-plated resonator, κ is recommended to be 1600, and for an interdigital resonator 2300. For experimental investigation in the present study, an air-filled coaxial $\lambda_0/2$ -resonator with a copper conductor ($b = 0.91$ inch) was designed for a centre frequency of 900 MHz. The unloaded Q-factor was measured by grapho-numerical method [89] and is equal to 1380. Under the same conditions, the unloaded quality factor was computed using Eq. 4.2.3 and is equal to around 1550, which is very close to the measured value. It is important to note that Eq. 4.2.3 does not consider any impact of an electrical length of the resonator, which was in the focus of discussion in [90]. Kurzrok proposed here that shortening of the TEM element will degrade unloaded quality factor and increase insertion loss: for CLF resonators with constant cross section, the effective unloaded Q-factor of the shortened resonator was found empirically:

$$Q_{UL-eff} \cong \sin^2(\theta_0) \cdot Q_{UL}, \quad (4.2.4)$$

where Q_{UL} is the unloaded Q-factor of the corresponding quarter-wavelength interdigital resonator. Eq. 4.2.4 has been criticised as giving an erroneously low result, but current study suggests that it can be taken as lower limit, enabling optimal filter design with both low losses and broad stop-band to be found from

the normalised factor $QS(\theta)$:

$$QS(\theta) = \frac{Q_{UL-eff}}{Q_{UL}} \cdot \frac{f_{SPB}}{f_0} \cong \sin^2(\theta) \cdot \frac{\pi}{\theta}. \quad (4.2.5)$$

This factor will be at its maximum if θ is 1.165 (or 67°), but because the second pass-band has been already specified in Table 3.6.1, the electrical length of resonators will be:

$$\begin{aligned} \theta_0 &= 30^\circ, \\ Q_{UL-eff} &\approx 0.25 \cdot Q_{UL}, \end{aligned} \quad (4.2.6)$$

so that the effective quality factor $Q_{UL-eff} = 345$ as measured.

Because the unloaded Q-factor of the resonators is finite, the insertion loss in a CLF will rise [91]:

$$L_0 = 4.343 \cdot \frac{f_0}{\Delta f} \cdot \sum_{i=1}^N \frac{g_i}{Q_{UL-eff}}, \quad (4.2.7)$$

where g_i are the normalised element values of the low-pass Butterworth prototype. In the present study, the insertion loss was calculated for a number of filter orders first with the Q-factor as measured and then with the Q-factor as computed. The calculation results for DT and ST filters are presented in Fig. 4.2.2. As seen, the ST filters have lower insertion loss than DT filters, a fact due to the

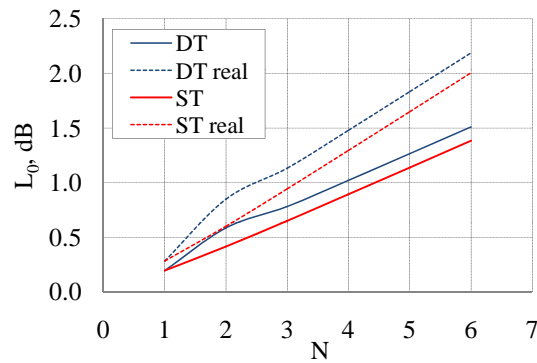


Figure 4.2.2: Insertion loss as a function of the filter order for the DT filters (blue curves) and ST filters (red curves). The calculation with the Q-factor as computed is shown by solid lines and with the Q-factor as measured by dash lines.

difference in g-parameters. From the analysis depicted in the figure, it can be concluded that both ST and DT third-order CLF with shorted resonators (30°) can have an insertion loss of less than 1 dB.

4.2.2 Simulation results

The choice of LPF prototype, filter type, and filter order now having been made, it is necessary for the purposes of the current study to relate the design parameters to the dimensions of the filter structure. The technique from [12] offers an initial possibility. It is based on foundation of both mutual capacitances to ground and mutual capacitances between neighboring lines. This calculation technique gives a first approximation for the filter dimensions, but the results are quite inaccurate for DT filters and cannot be used for ST filters at all, because the internal impedance of the current generator is infinite. For the ST filters, it is necessary to use a finite g_0'' , which was defined in [12]:

$$g_0'' = \frac{10^{\frac{L_{Ar}}{20}}}{g_{N+1}}, \quad (4.2.8)$$

where L_{Ar} is maximum attenuation in-band in a LPF with Chebyshev response (and is zero in LPFs with Butterworth response). The technique is that already defined for the adaptation of typical filter design to an ST filter type. For ST filters it is thus necessary to substitute $g_0'' = 1$ for $g_0 = \infty$ in Table 3.4.1. It was done in the next step of the filter design, when ADS software was used in the design of CLFs. In ADS software, it is possible to approximate coaxial coupled lines by planar striplines representing a multi-layer substrate. The copper conductors are placed in the middle between the ground layers. The TEM elements of the resonators, with a physical length of $l = 54 \text{ mm}$ and a thickness of 3 mm , are located at a distance of 11.5 mm from the ground planes. The ADS simulation results are presented in Fig. 4.2.3. It is only at the centre frequency that the resistance of the DT CLF is equal to 50Ω and there are significant maxima in-band, shown in Fig. 4.2.3,a. In contrast, the ST CLF provides relatively constant

input resistance over the whole pass-band, as shown in Fig. 4.2.3,a. In the Smith chart, there is rotation of the reflection coefficient of both filters, which is caused by a phase delay in the input line. This phase delay can result in a high reactance at the filter input and, consequently, in high reactive currents and voltages at the transistors. Moreover, as this phase delay will insert asymmetry at the filter input, it is necessary to minimise it.

In order to realise an impedance transformation in ST CLFs, it is necessary to apply the approach, proposed in the section 3.4.2, where it was shown that it is necessary for the first resonator to have the desired input impedance, and for the other resonators to maintain their impedances. Because the present design of a CLF has an input line, this input line should have the same impedance as the first resonator. To establish whether there are restrictions to this approach, three ST impedance-transforming CLFs were designed. The impedance transformation ratios 1, 2 and $\frac{1}{2}$ were realised, representing absolute impedances of 50 Ω , 100 Ω and 25 Ω . The layouts designed are presented in Fig. 4.2.5. Except for the first resonator and the input line, the geometry of each filter is absolutely identical and offers a considerable advantage in the design of filters with tunable input impedance. The simulated reflection coefficients are depicted in Smith Chart in Fig. 4.2.4. Though the impedance has been scaled to different

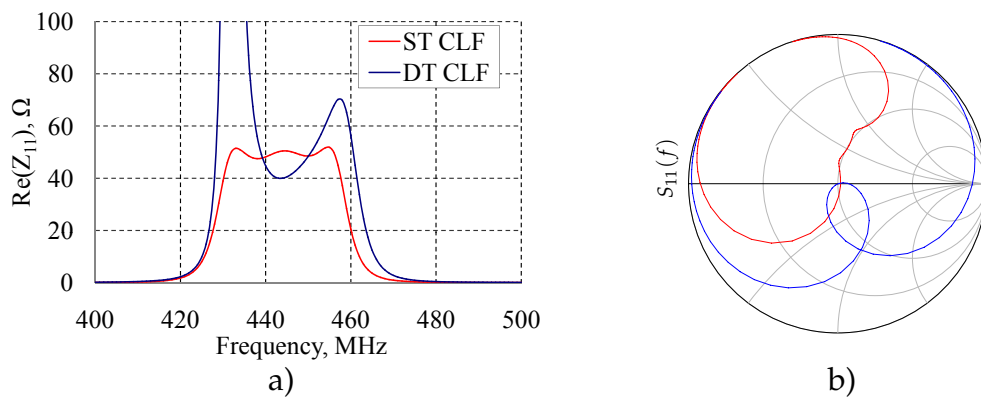


Figure 4.2.3: ADS simulation results: input resistance (in panel a) and reflection coefficient (in panel b) of the third-order Butterworth DT CLF (blue curves) and the ST CLF (red curves).

levels, the characteristics of all the filters are identical in shape. Because the input lines are identical in length, the rotation in the Smith Chart is through the same angle.

Although it is theoretically possible to apply the approach to any filter type and to any impedance level, as was indicated by the simulation reported in section 3, the normal physical limitations apply. For example, very low impedance will require the use of dielectric material; very high impedance would posit extremely narrow conductor strip. Nonetheless, the method has the great advantage of simplicity in that the only features requiring modification are the first resonator and the input line of a CLF.

4.2.3 Measurement results

The dimensions of the filter structure having been found by means of computer simulation, it was necessary for the purposes of the current study to manufacture and experimentally investigate such a filter. A coaxial third-order DT CLF operating at $f_0 = 450$ MHz, and without impedance transformation, was therefore fabricated. The resonators, with an electrical length of 30° or a physical length of 54 mm, were short-circuited at one end and had distributed capacitances between the other ends and ground. In order to reduce the phase shift in the distributed capacitances, these were implemented as electrically short very-low-impedance coaxial lines. The resonators, input line

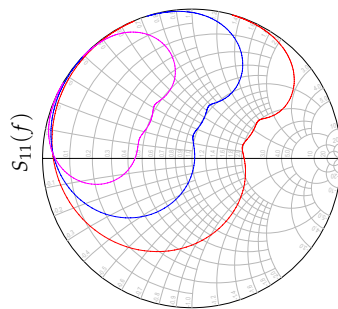


Figure 4.2.4: ADS simulation results: reflection coefficients of third-order microstrip ST CLFs with impedance transformation ratios of 2 (red), 1 (blue) and $\frac{1}{2}$ (purple).

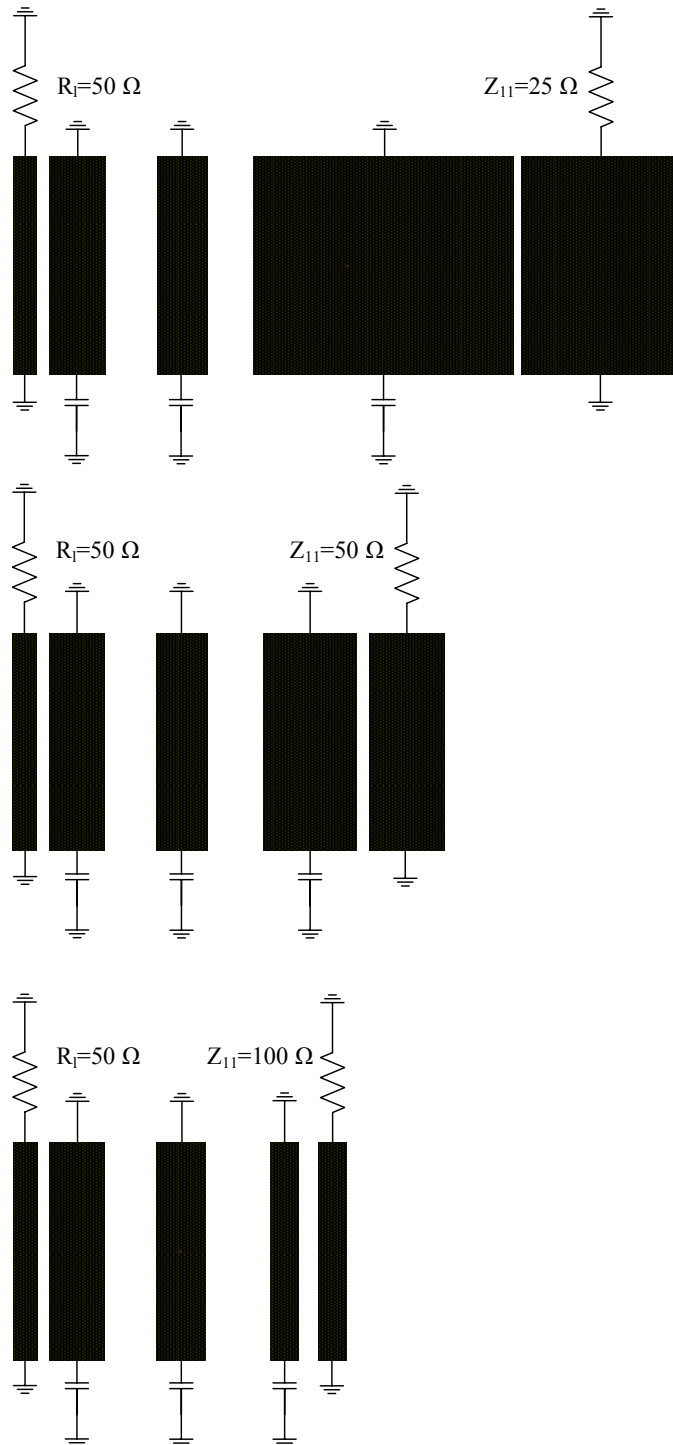


Figure 4.2.5: Layout of third-order ST microstrip CLFs with impedance transformation ratios of 2, 1 and $\frac{1}{2}$.

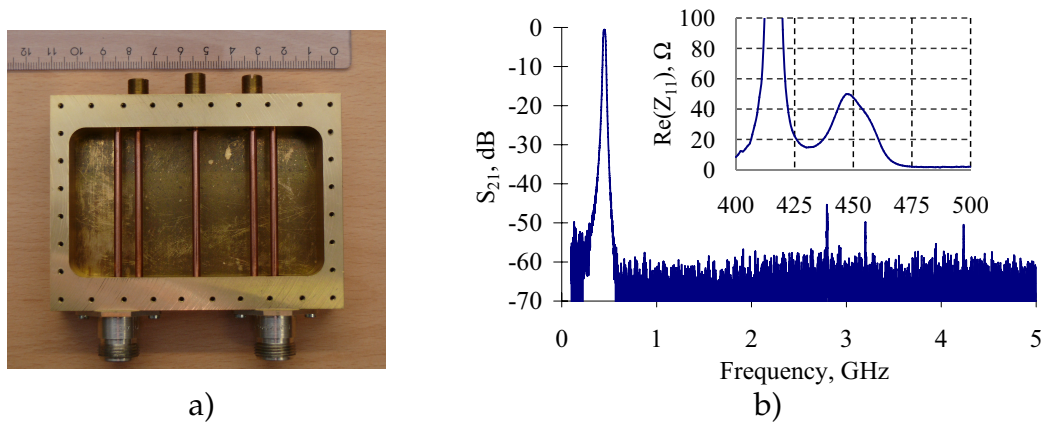


Figure 4.2.6: Photograph (in panel a) and the measurement results (in panel b) of the coaxial third-order DT CLF. The inset shows the input resistance in-band.

and output line were copper rods with a radius of 1.5 mm . The device measured $105 \text{ mm} \times 78 \text{ mm} \times 30 \text{ mm}$ in size (or in fractions of λ : $0.16 \times 0.12 \times 0.05$). Fig. 4.2.6 shows a photograph of the filter as manufactured and a graph of the filter characteristics as measured. The filter has measured insertion loss of less than 0.55 dB , a 3-dB-bandwidth of 26 MHz , and a second pass-band at about 2.8 GHz with suppression of 45 dB [92]. Although the measured bandwidth is slightly broader than it was in simulation, the measurement and simulation results agree quite well. As the filter was doubly terminated, the input resistance is equal to 50Ω at the centre frequency only, and rises sharply at a frequency of 416 MHz (inset diagram in Fig. 4.2.6,b). There is only one maximum in-band, because the input line inserts a phase delay and rotates the Smith Chart so that the second maximum disappears. This experimental setup and its analysis demonstrated that the shape of the input impedance is strongly affected not only by the filter termination, but also by the a phase delay at the filter input.

4.2.4 Frequency tunability

As has been mentioned, if reduction in the cost and complexity of the whole PA system are to be achieved, it will be necessary for the reconstruction

filter to be tunable between the operating frequency bands. There are various tuning techniques for microwave filters proposed in [12], e.g. magnetically tunable filters (ferromagnetic resonance filters, magneto-static wave filters, evanescent waveguide filters, E-plane printed circuit filters), electronically tunable filters, and mechanically tunable filters. It was shown in [93] that if both high power handling capability and low insertion loss are required, it is possible to tune filters either mechanically or magnetically. In the current study, the choice fell on the mechanical tunability, because it is also necessary for the reconstruction filter to have a broad stop-band. There is an example of a mechanically-tunable, coaxial filter in which the tuning was accomplished by sliding the round centre conductor back and forth through the short-circuiting region at the lower end of each resonators [12]. This tuning technique exhibited some difficulties in practice, because it was necessary for the resonators to slide freely and, at the same time, to have good short-circuiting at their ends. Moreover, the stop-band behaviour of this filter depends on the electrical length of the TEM elements and is not always optimal over the entire tuning range.

It is also possible to tune a CLF using the distributed capacitances at the ends of the resonators, which can be screwed in and out, changing their values. It is an advantage of this method that the second pass-band is not affected by tuning, because it is determined only by the electrical length of the TEM elements, which maintain their lengths. For the current application, such mechanical tunability presents the optimum trade-off between low insertion loss, high power-handling capability, and a wide stop-band. Also, if the frequency is to increase, the insertion loss will diminish. This effect can be explained by the physical length of the TEM elements, which corresponds now to an extended electrical length at the new frequency. It is also easy to extend the tuning range as this depends on the difference between the minimum and the maximum capacitance values.

In order to investigate this tuning technique experimentally, the coaxial CLF presented in the previous section was mechanically tuned. Fig. 4.2.7 shows the measured transmission coefficients over a tuning range from 320 MHz to

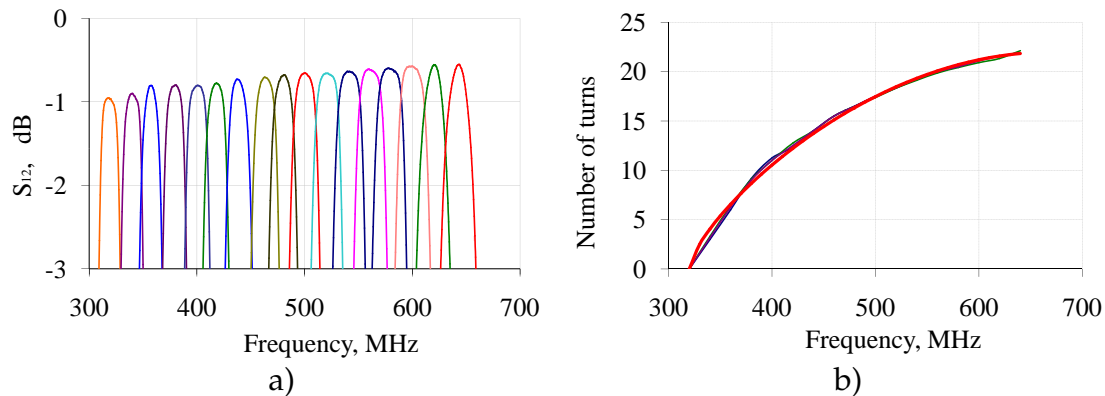


Figure 4.2.7: Pass-bands of the mechanically tunable CLF for different tuning states (in panel a) and tuning functions (the frequency dependence of number of turns as a function of frequency) for the CLF resonators (in panel b).

640 MHz (one octave) [94]. Over the entire tuning range, the filter has an insertion loss of less than 1 dB (Fig. 4.2.7), and a second pass-band occurring at 2.8 GHz (not seen in the figure). As was expected, the measured insertion loss drops as frequency rises. As it is necessary to tune the filter only for the first adjustment of the BTSs, high tuning speed is not required and the tunability can be realised with digitally controlled stepper motors, which also provide high repeatability and reliability. The tuning function in which the frequency change reflects the number of turns is presented in Fig. 4.2.7,b. For all resonators, the tuning functions are sinusoidal in shape.

4.2.5 High power handling capability

In addition to having all the properties discussed above, it is necessary for the reconstruction filter to handle a power level of 100 W. The power-handling capability of the filter is limited by electrical breakdown, which can occur in the regions with high electric field concentration. There is an extensive study of gaseous breakdown phenomena, where a number of interdependent factors affecting when critical strength occurs have been determined [95]:

1. the composition and the pressure of the air or other gaseous medium filling the device;

2. the operating frequency;
3. the size and the shape of the region where the electric field approaches its maximum;
4. the presence of nearby conducting surfaces, their shapes, and spacing;
5. the duration, shape, and repetition frequency of applied pulses.

In dry air under atmospheric pressure the breakdown will occur if the peak electric field strength \hat{E}_{air} reaches 2.9 MV/m, which will arise if the maximum possible power is applied to the filter input:

$$\hat{P}_{RF_{in}} = P_{RF_{in}} \cdot \left(\frac{\hat{E}_{air}}{\hat{E}_{sim-air}} \right)^2, \quad (4.2.9)$$

where $\hat{E}_{sim-air}$ is the peak of electrical field strength occurring in the filter at the level $P_{RF_{in}}$ of the input power. In order to estimate the power handling capability of the CLF (shown in Fig. 4.2.6,a), the numerical simulation was carried out. It was found that the critical position with the highest electrical field strength is in the narrow gap of 200 μm in the distributed capacitances at the ends of the resonators. The calculated maximum input power (before breakdown occurs) was estimated at 66 W, a level undesirably lower than the required level of 100 W.

It is critical to prevent electrical breakdown in the design of the filters intended for high-power applications. Cohn reviewed the requirements of high-power filters and discussed various design approaches [95]. Vogelman and Whinnery proposed varying impedance waveguides and coaxial structures, where changes of the cross sections of the wave guiding structures were tapered rather than abrupt [96, 97]. In all the above high-power filter designs, it was necessary to round all corners, to smooth and polish all surfaces, and to eliminate any contaminations and irregularities. On the basis of these guidelines, an improved version of the coaxial CLF meeting the required power-handling capability was devised. In the present instance, the maximum tolerable power

was increased by minimising the electric field gradients in the following ways:

1. all the corners in the impedance-step areas and, especially, at the ends of the resonators were smoothed,
2. the air gaps along the distributed capacitances were filled with PTFE dielectric material ($\epsilon_r = 2.1$ and $\tan(\delta) = 0.0004$), of which the maximum electrical field strength before breakdown is 60 MV/m.

It being necessary, as stated, to modify the distributed capacitances at the ends of the resonators, which have an influence not only on the power-handling capability and the insertion loss, but also on the stop-band, it is logical for these capacitances to utilise high-ohmic transmission lines with a high Q-factor. On the other hand, in order to provide the desired capacitance values, it will be necessary to use electrically-long transmission lines, which may shift the second pass-band to the lower frequencies, because of their high parasitic inductance. This behaviour can be described by the coefficient $\chi(Z_{EC})$, which depends on the line impedance of this distributed capacitance, Z_{EC} :

$$\chi(Z_{EC}) = \frac{f_{SPB-sim}(Z_{EC}) - f_{SPB}}{f_{SPB}} \cdot Q_{UL}(Z_{EC}) \cdot P_{aver}(Z_{EC}), \quad (4.2.10)$$

where $f_{SPB-sim}(Z_{EC})$ is the simulated result for the second pass-band, $Q_{UL}(Z_{EC})$ is an unloaded Q-factor of the transmission line from Eq. 4.2.3, and $P_{aver}(Z_{EC})$ is the normalised average power, which can be handled by a matched transmission line [12]:

$$P_{aver}(Z_{EC}) = \frac{\hat{E}_{sim-air}}{480} \cdot \frac{D^2 \cdot \ln D/d}{D/d^2}, \quad (4.2.11)$$

where D and d are the outer and inner diameters of the coaxial line in mm. Fig. 4.2.8 illustrates the function $\chi(Z_{EC})$. This is at its maximum if $Z_{EC} = 19 \Omega$, which indicates the optimum and was incorporated as optimal line impedance into an improved filter design. Fig. 4.2.9 shows the cross-section of the capacitances at the ends of the resonators. The PTFE material (magenta color in the figure) does not only cover the ends of the resonators, but also extends into

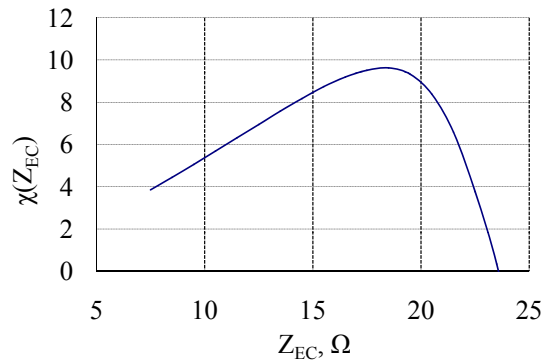


Figure 4.2.8: Influence of the transmission line impedance of the distributed capacitance at the end of resonators on the coefficient $\chi(Z_{EC})$.

the resonant sections, as an additional protection against electrical breakdown. It was established that the radii of irregularities were small compared to the wavelength and the manufactured new filter therefore had the same geometrical dimensions as before. As is shown in Fig. 4.2.9, the filter provides a measured insertion loss of about 0.37 dB, a 3-dB-bandwidth of 27 MHz, a second pass-band at 2.8 GHz with suppression of better than 65 dB, and a third pass-band at 5.4 GHz. As a result of the insertion of the dielectric filling, the critical position of the highest electric field strength moved to a location between the input line and the first resonator, where the distance is about 20 times higher than in the original design. According to the results of numerical simulation, the

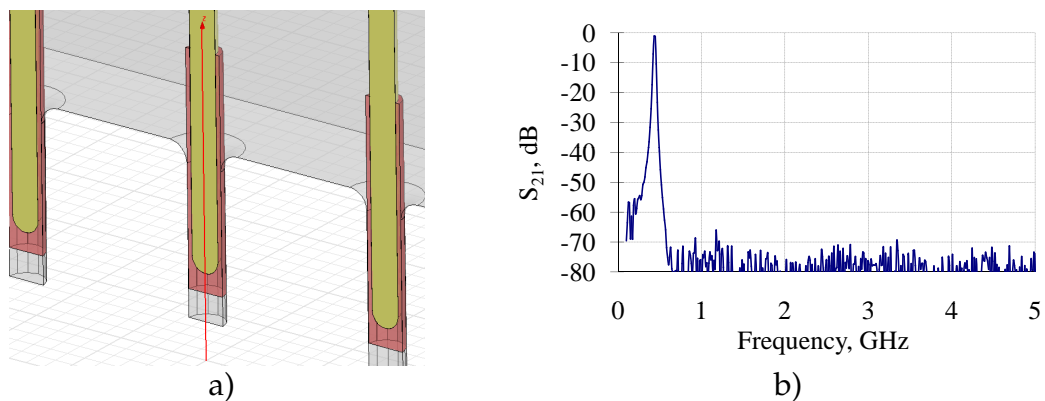


Figure 4.2.9: Sketch of the CLF, laid out for high power handling (in panel a) and measured transmission coefficient (in panel b).

maximum theoretical input power before breakdown expected from Eq. 4.2.9 amounts to 6 kW. In practice, achieving such high power levels may be prevented by the limited power-handling capability of other filter constituents, e.g., the connectors. In the current study, the power handling capability of both filters was experimentally investigated. Accurate measurements made using both CLFs, calibrated power meters, high-power directional coupler, cables, high-power load and a network analyser are shown in Fig. 4.2.10. The filters were excited by sinusoidal signals of 430 MHz, amplified in the case of the original filter at between 5 W and 65 W, and in the case of the modified high-power version at up to 320 W (limited only by the amplifier). As part of the input power is forwarded within the directional coupler to the network analyser through the attenuators, the difference between the RF-signals measured before and after filtering is the insertion loss in the CLF. The measurement results in Fig. 4.2.11 show a constant low insertion loss up to power levels of 54 W for the original filter (this drop insertion loss is caused by the electrical breakdown, which occurred at the end capacitance of the first resonator, shown in Fig. 4.2.12,a) and up to more than 300 W for the novel filter, with even lower losses [98]. This difference between the original and the modified filter demonstrates the efficiency of the measures undertaken to improve the power-handling capability. Also, when the reflected power at the input of the filter was evaluated using

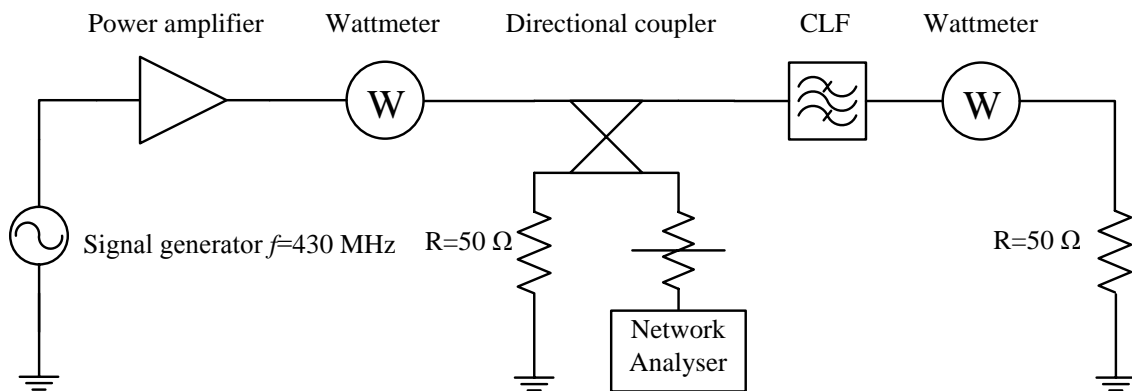


Figure 4.2.10: Measurement test setup including a signal generator, a power amplifier, a CLF, calibrated power meters, a high-power directional coupler, cables, a high-power load and a network analyser.

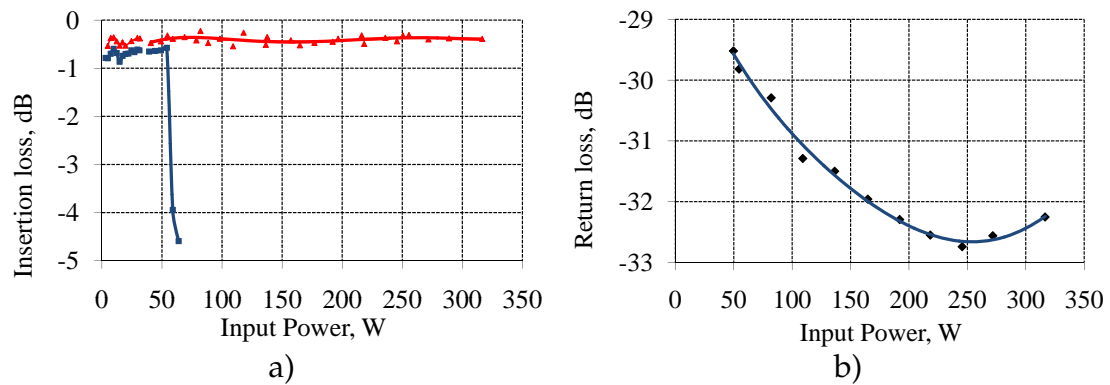
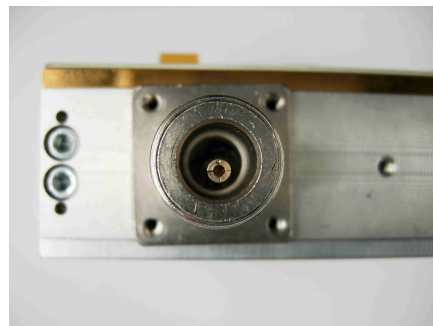


Figure 4.2.11: Results of the high-power measurements: blue curve and squares - original filter version, red curve and triangles - modified filter version (in panel a). Reflection coefficient of the CLF optimised for high-power operation versus input power (in panel b).

a network analyser, the input matching was found to be about or better than 30 dB for both filters. It was in the nature of the measurement process that every measurement point took some seconds to read and that there was low RF input power at the start. As a result, the high-power filter (with a weight of 1.2 kg) warmed up to about 30 degrees Celsius at maximum RF power which resulted in a dissipation loss of about 30 W. Fig. 4.2.11,b indicates a marginal degree of dependence of the reflection coefficient on the RF input power for the novel CLF; this could be caused by thermal effects. For instance, during long



a)



b)

Figure 4.2.12: Results of an electrical breakdown occurred in the distributed capacitance at the end of the first resonator (in panel a) and the N-connector damaged through the thermal effect (in panel b).

measuring sessions the temperature of the filter rose to 150 degrees Celsius, which caused thermal damaging of the N-connectors, as shown in Fig. 4.2.12,b. Nonetheless, the filter performance did not deteriorate even with a hold-time of three minutes at maximum RF power of the amplifier.

4.3 Balanced input comb-line filter design

It has been made clear above that a CMCS PA system demands a balanced input reconstruction filter, which can be designed on the basis of the tunable high-power coaxial CLF presented in the previous section. The necessary balanced input is achieved in various known microwave filter designs, such as the use of a LPF and a HPF in the signal paths [99]; or of a balun (or a directional coupler with phase shifting circuits) [100, 101]; or of a centre-loaded, half-wavelength resonator [102]; and so on. In the Mobile-GaN research program, a balanced-input, lumped-element reconstruction filter utilising a commercial balun was presented in [58], for which it was, however, still necessary to improve some of the filter characteristics, for example, out-of-band impedances, insertion loss, and selectivity. This section will present four alternative architectures for balanced input reconstruction filters: a Balanced Input CLF (BICLF) with a straight loop, a BILCF with a pulse shaping network, a BICLF with an electrically long input loop and a BICLF with an electrically short input loop [103–105].

4.3.1 Architecture with a straight loop

To take a BICLF with a straight loop first: this is illustrated in Fig. 4.3.1 and consists of a CLF and a shunt capacitor C_{SH} . The architecture can also be considered as a balun with a filter property. For example, it would be possible to use a Marchand balun with reduced electrical length of TEM-elements ($\leq \lambda/2$) [101, 106], and then to enhance its selectivity by the technique in [107]. However, as it is necessary in the present study to ensure the properties of a

CLF are kept, (low losses, compactness, and broad stop-band), the approach taken in this section is to consider the BICLF with a straight loop as a modified CLF.

In order to organise balanced input into a CLF, it is necessary to split its input line at the centre and thereby to form two single-ended input ports, which are connected to the final stage by the $50\ \Omega$ coupled line. Firstly, this architecture will be analysed in terms of input impedances in-band. Because the field distribution along the first resonator determines the electrical currents through the input lines, the phase shift between the filter pins is around 180° . Such excitation is associated with a differential mode, which has input impedance of $50\ \Omega$, because the input impedance of both the coupled line and the original filter were also $50\ \Omega$. At the same time, the other ends of the input lines are connected to the filter housing, which should be isolated from the common ground. Because the input line is parallel to the first asymmetrical resonator, it may provide the desired suppression of the common-mode of excitation. Secondly, it is necessary to analyse this architecture in terms of input impedances out of band. In the present instance, in order to provide the short for the higher harmonics of the drain current, the SMD shunt capacitor C_{SH} was mounted between the filter pins. For the lower frequencies, it is possible to realise the short-circuiting through the filter housing, because the filter and the final stage have no common ground, and there is a floating node in DC. Such an

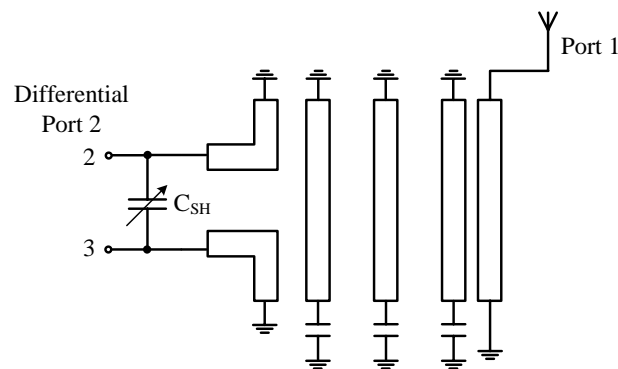


Figure 4.3.1: Schematic of a third-order BICLF with a straight loop consisting of a CLF and a tunable shunt capacitor C_{SH} .

isolated connection can be described by the common-mode input impedances $Z_{com} = \infty$, because of $Y_2 = Y_3 = Y_g = 0$ in Eq. 3.2.1. This will perfectly fulfil the requirements for the common-mode input impedance in and out of band, expressed by Eqs. 3.2.4, 3.2.7. In theory, the main advantages of this architecture will be relative simplicity, compactness, and obviation of the need for additional devices.

The CLF having been successfully designed, the next step was to modify it as described above. In the current study, the BICLF for a centre frequency of 450 MHz and input impedance of 50Ω was designed with the aid of Ansoft HFSS software, which enables 3D full-wave electromagnetic field simulation. Fig. 4.3.2 shows an HFSS sketch of the BICLF with a straight loop. The input line was split at its centre and connected to the final stage through a PTFE window in the top wall by the $50\text{-}\Omega$ coupled line (German patent pending [108]). In HFSS software, the filter housing was presented by a vacuum box surrounded by perfectly conducting walls. The resonators and PTFE elements were implemented as volumetric elements, subtracted from the vacuum volume. In the present design, the BICLF has almost the same geometry as the original filter; the only features requiring modification are the input line and coupling between it and the first resonator. The capacitor $C_{SH} = 3.3 \text{ pF}$ was simulated as a lumped RLC boundary between the filter pins. To model the coupling between the two strips in one port face accurately, it was necessary to analyse the differential port in the "driven terminal" simulation type, which enables multiple modes of excitation to be analysed. In general, if there are M disconnected conductors in the port cross-section, at least $(M - 1)$ modes are required for an accurate solution results. In the present design, the port consists of two adjacent striplines surrounded by a conducting enclosure, $M = 3$; therefore for the simulation at least two modes should be defined on the port (differential and common modes). Moreover, in "driven terminal" solution type it is also possible to analyse the filter structure with separate identification of each terminal. The 2D-visualisation of the electric field patterns on the port surface in differential and common mode is shown in Fig. 4.3.3. If the port is excited in differential mode, the electrical cur-

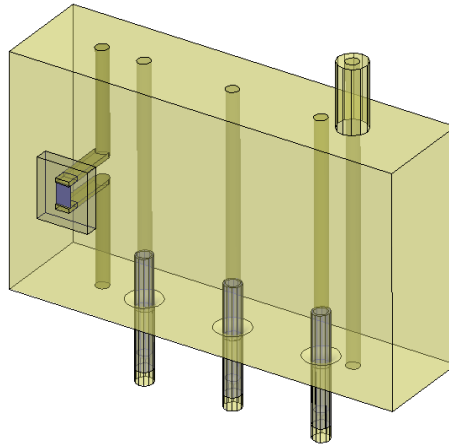


Figure 4.3.2: The HFSS sketch of a coaxial third-order BICLF with a straight loop.

rents are flowing through the filter pins in opposite directions, as illustrated in Fig. 4.3.3,a. In contrast, the electrical currents are co-directional if the port is excited by common mode, as shown Fig. 4.3.3,b.

The EM simulation results in-band are presented in Fig. 4.3.4. The filter has insertion loss of less than 0.3 dB over a 3 dB-bandwidth of 28 MHz, return loss better than 30 dB, and a common mode with suppression of better than 20 dB. This result thus approximates very closely to the mixed-mode S-matrix of Eq. 3.2.5. Because of the parallel capacitor C_{SH} , out-of-band differential-mode input impedance maintains low-ohmic level over the frequency ranges from 1 GHz up to 3 GHz (dotted curves in Fig. 4.3.5,a-b). The simulation indicated that low-ohmic impedance at frequencies less than 1 GHz would not be feasible because of the resonance at 560 MHz, probably caused by the parallel resonance circuit built by the shunt capacitor C_{SH} and the input lines. There are also pronounced maxima in differential-mode impedance in-band shown in Fig. 4.3.5,a, which are explained by the fact that the BICLF was doubly terminated.

The BICLF as designed up to this point was manufactured and experimentally investigated. The filter housing was fabricated from aluminum, measuring $105\text{ mm} \times 78\text{ mm} \times 30\text{ mm}$ in size, inside and top views of which are shown in Fig. 4.3.6. The input and output lines, and three resonators were copper rods with a radius of 1.5 mm. PTFE material was utilised in both the dielectric win-

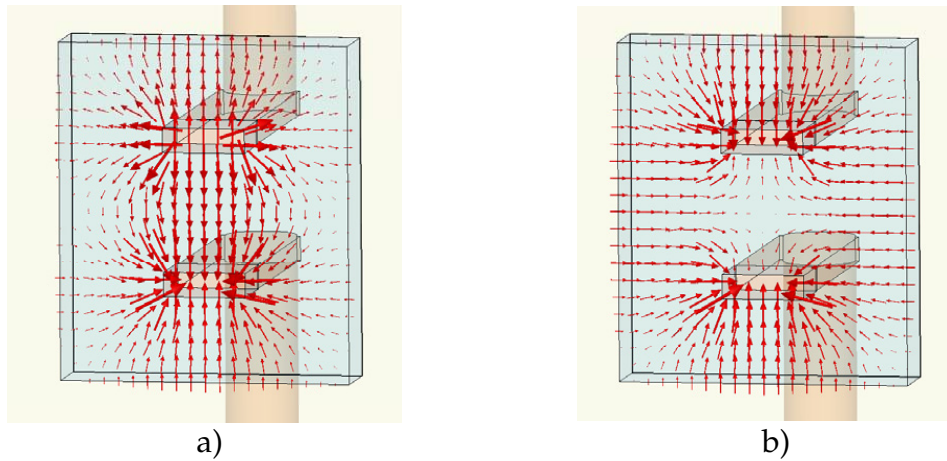


Figure 4.3.3: The 2D-visualisation of the electric field patterns on the port surface in differential mode (panel a) and common mode (panel b).

dow in the top wall and the isolating rings at the ends of the resonators. To measure this BICLF it is necessary to employ a 4-port network analyser, but to calibrate it at only three of its ports (two of which form the differential port). The BICLF has insertion loss of 0.7 dB, a 3 dB-bandwidth of 27 MHz located around a centre frequency of 450 MHz, when common mode is suppressed by 35 dB, as shown in Fig. 4.3.4 [103]. The measured differential-mode input impedance is $(32 - j \cdot 6.5)\Omega$, somewhat less than it was in simulation. Out-of-band, the measured results agree with EM-simulation results and show low-ohmic values over

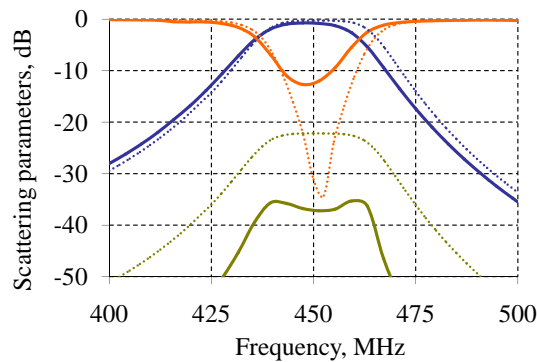


Figure 4.3.4: The measurement (solid lines) and EM simulation results (dotted lines) of the BICLF with a straight loop: S_{D1} - blue curve, S_{DD} - orange curve and S_{C1} - green curve.

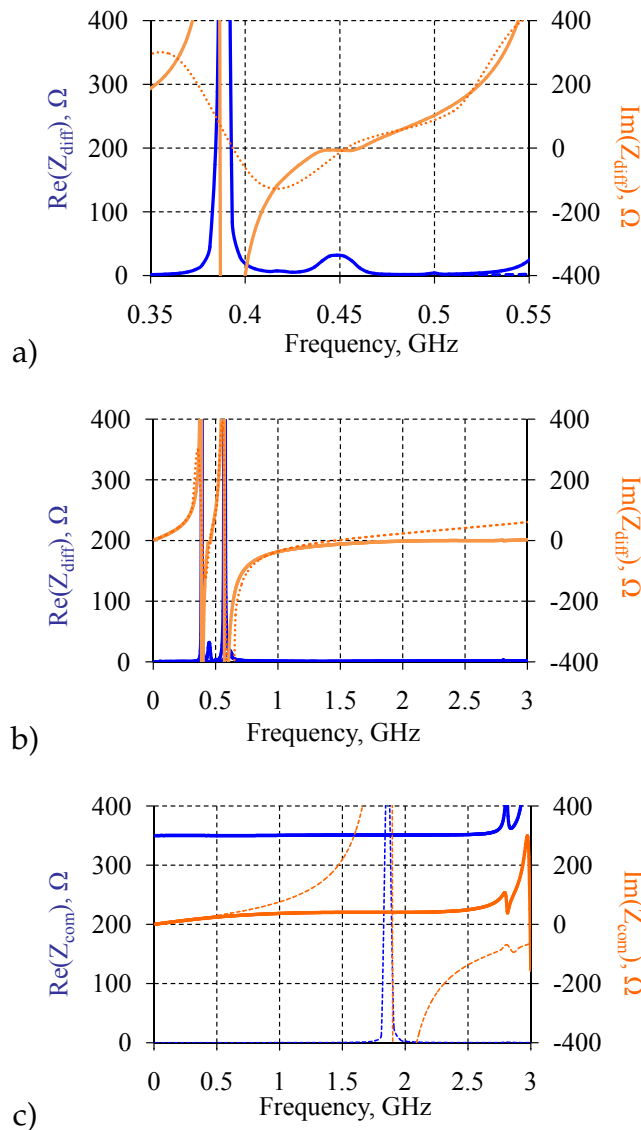


Figure 4.3.5: The measurement (solid lines) and EM-simulation results (dotted lines) of the BICLF with a straight loop: differential-mode impedance (in panels a and b) and common-mode impedance (in panel c).

the frequency range from 1 GHz up to 3 GHz, as shown in Fig. 4.3.5,b. As seen, the second pass-band appears only at 2.8 GHz. Thus, in-band and out-of-band the measurement and simulation results agree quite well.

As the HFSS software did not offer the option of galvanically isolating the filter body from the common ground, it was not possible to simulate the

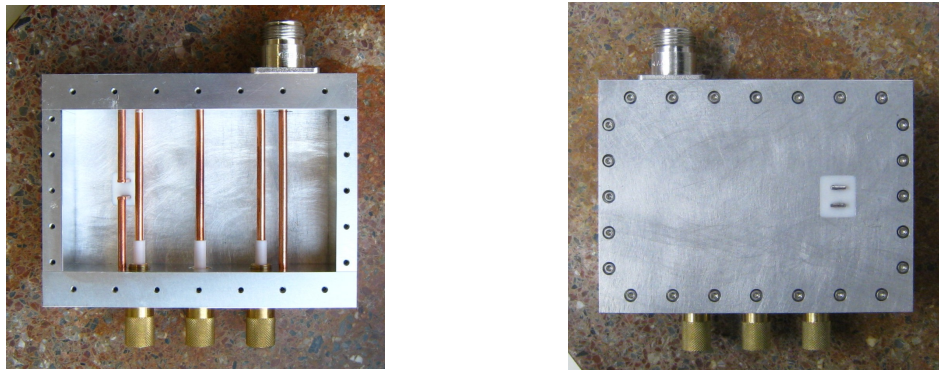


Figure 4.3.6: Photograph of the coaxial third-order BICLF with a straight loop (inside and top views).

common mode impedance correctly. The same challenge was met during the 4-port measurement in respect of the unbalanced S-parameters as measured and the mixed-mode S-parameters as calculated. ADS software is the only option for isolating the BICLF. Here, the measured data can be represented by the 4-port data block with an additional reference port operating in non-grounded mode, as shown in Fig. 4.3.7. The degree of isolation will depend on the resistor between the filter and the common ground, which is $R_1 = 350 \Omega$ in ADS simulation, as illustrated in Fig. 4.3.7. Therefore there is an offset by 350Ω in the common mode impedance, as shown Fig. 4.3.5,c. In theory, this isolation resistor can take even higher values, depending on the degree of galvanical isolation of the filter housing; the requirements for the common-mode suppression will be the deciding factor. However, because the filter housing may produce

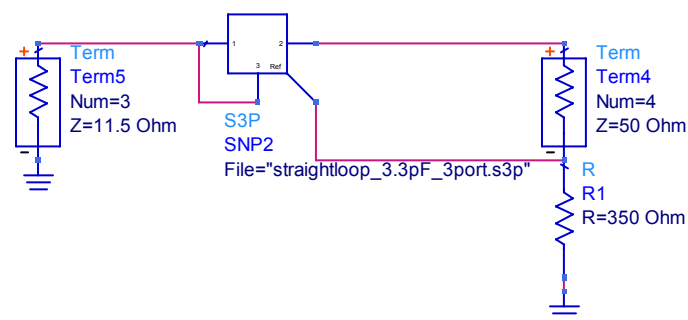


Figure 4.3.7: Representation of the measurement results in the ADS software.

the electromagnetic radiation, there it may be problematic to use this architecture in practice, which requires further investigation.

This section has presented the BICLF with a straight loop, successfully combining the properties of a CLF and a balun. From the analysis carried out, it can be concluded that this architecture will fulfil all the requirements for a CMCS PA system. Although the BICLF has low losses, broad stop-band, and low-ohmic differential-mode input impedance out of band, there is some room for further improvements so as to avoid the need for galvanic isolation.

4.3.2 Design with a pulse shaping network

As the previous filter had the disadvantage of the necessity for galvanic isolation, a Pulse Shaping Network (PSN) was developed for the next architecture to be investigated. In Fig. 4.3.8 a BICLF with a PSN is illustrated. This is a BICLF with a straight loop and a lumped-element PSN. The pulse shaping network, formerly named a predistortion network [104], is a second-order BPF from [64]. It is necessary for the PSN to provide the impedance conditions out of band, under which the drain currents keep their shape. These conditions can be achieved if the PSN consists in short-circuiting for the differential mode

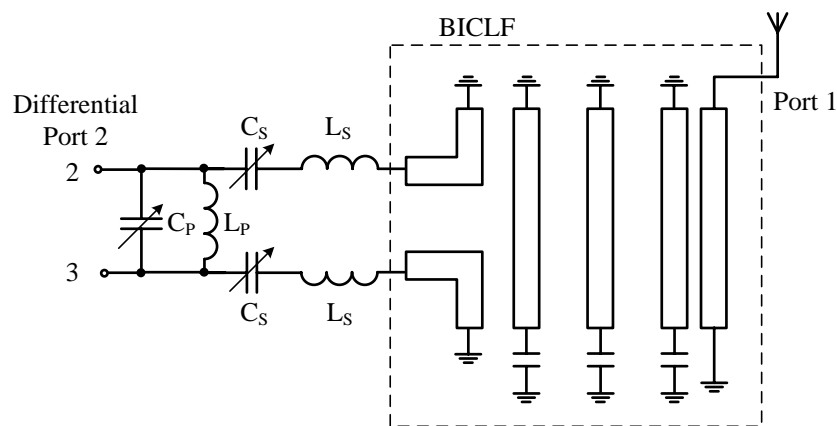


Figure 4.3.8: A BICLF with a pulse shaping network consisting of a BICLF with a straight loop (inside the dashed rectangle) and a lumped-element PSN for impedance matching, containing adjustable shunt and series capacitances.

out of band, and open-circuiting for the common mode out of band. For the present case, in order to provide high-ohmic common-mode impedance, two series circuits, with high-value inductors L_s and adjustable capacitors C_s , were employed; to achieve the short-circuiting out of band, the parallel resonant circuit $L_p C_p$ was utilised.

To simulate the BICLF with a PSN in ADS software, it was possible to use the measurement results of the BICLF with a straight loop from the previous section. For the PSN the S-parameter blocks of the Coilcraft inductors (limited by frequency of 2.2 GHz) and ideal capacitances were used. The element values were adjusted to approximate the piece-wise requirements:

$$\begin{aligned} f = f_0 \pm \Delta f/2 : \quad & Z_p = 2 \cdot Z_0 \wedge Z_s \ll Z_0 \wedge Z_{diff} = (65 + j \cdot 0)\Omega, \\ f \neq f_0 \pm \Delta f/2 : \quad & Z_p \ll Z_0 \wedge Z_s \gg Z_0 \wedge Z_{diff} < (6.5 + j \cdot 0)\Omega, \end{aligned} \quad (4.3.1)$$

where Z_0 is the impedance of the input port, Z_p is the shunt impedances of the PSN, and Z_s are the series impedances of the PSN. Meeting the constraints of Eq. 4.3.1 with real elements brings with it two challenges:

1. the losses of lumped-element capacitors and inductors limit the overall quality factor of the filter;
2. it is sufficient for conditions matching Eq. 4.3.1 to stay within limits of Δf_{SH} rather than Δf .

Moreover, the PSN matches in-band impedance of the final stage 50Ω to the BICLF with a straight loop impedance of 65Ω . The ADS simulation results in-band are presented in Figs. 4.3.9- 4.3.10,a. The device has insertion loss of 0.95 dB at a centre frequency of 450 MHz, a 3-dB bandwidth of 24 MHz and a wide stop-band up to 2.8 GHz (not seen in figures). At the centre frequency, the BICLF has differential input impedance of $(64+15j) \Omega$, and a common mode with suppression of 15 dB. Because the PSN represents a second-order doubly-terminated BPF, there are two resonance peaks at frequencies of 390 MHz and 520 MHz in the differential-mode impedance in Fig. 4.3.10,a. The ADS simulation results out of band are presented in Figs. 4.3.10,b-c. As seen,

the differential-mode input impedance out-of-band is zero from DC and up to 3 GHz, except for the frequency range around the centre frequency, $(f_0 - \frac{\Delta f_{SH}}{2}; f_0 + \frac{\Delta f_{SH}}{2})$ with $\Delta f_{SH} = 200$ MHz. At the same time, the common mode reactance takes high-ohmic values over the same frequency range. These filter characteristics are a close approximation to the mixed-mode S-matrix in Eq. 3.2.5.

For experimental investigation in the present study, the BICLF with a PSN was manufactured, as shown in Fig. 4.3.11. In order to position the shunt resonator as close as possible to the final stage, its elements were mounted on the top wall of the filter housing. The series circuits of the PSN were implemented inside the filter body, so that the size of the filter was unchanged at $105\text{mm} \times 78\text{mm} \times 30\text{mm}$. In this arrangement, it is possible to minimise parasitic capacitances against ground. Another possible realisation would be to print both the first resonator and the PSN on the printed circuit board, which might simplify the adjustment process. For the current study, high-voltage multi-layer DLI capacitors (C06-CF) and high-quality Coilcraft inductors (0906-4GL and 1812SMS-39N) were employed. In order to minimise the mutual coupling, it was necessary to mount the inductors of the series circuits in opposite directions. For the final tuning, high-quality Tecelec trimmers (27281SL) for both series and parallel circuits were used. The measurement results are presented in Figs. 4.3.9-4.3.10. The filter has an insertion loss of 1 dB, including a half dB

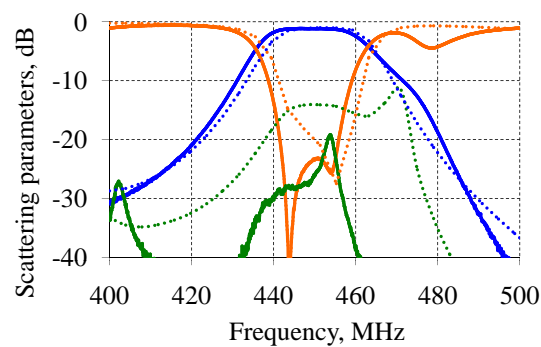


Figure 4.3.9: Measurements (solid lines) and ADS simulations (dotted lines) of the BICLF with a PSN: S_{D1} - blue curve, S_{DD} - orange curve and S_{C1} - green curve.

of losses in the PSN (caused mainly by the inductors). Over a 3 dB bandwidth of 450 ± 13.5 MHz, the resulting BICLF has differential-mode input impedance of $(55 + 2j)\Omega$. The common mode S_{C1} was suppressed by 20 dB, as shown by green curve in Fig. 4.3.9 [104]. From the broadband measurements (shown in Fig. 4.3.10,b), it is seen that the differential mode resistance is less than 6.5Ω

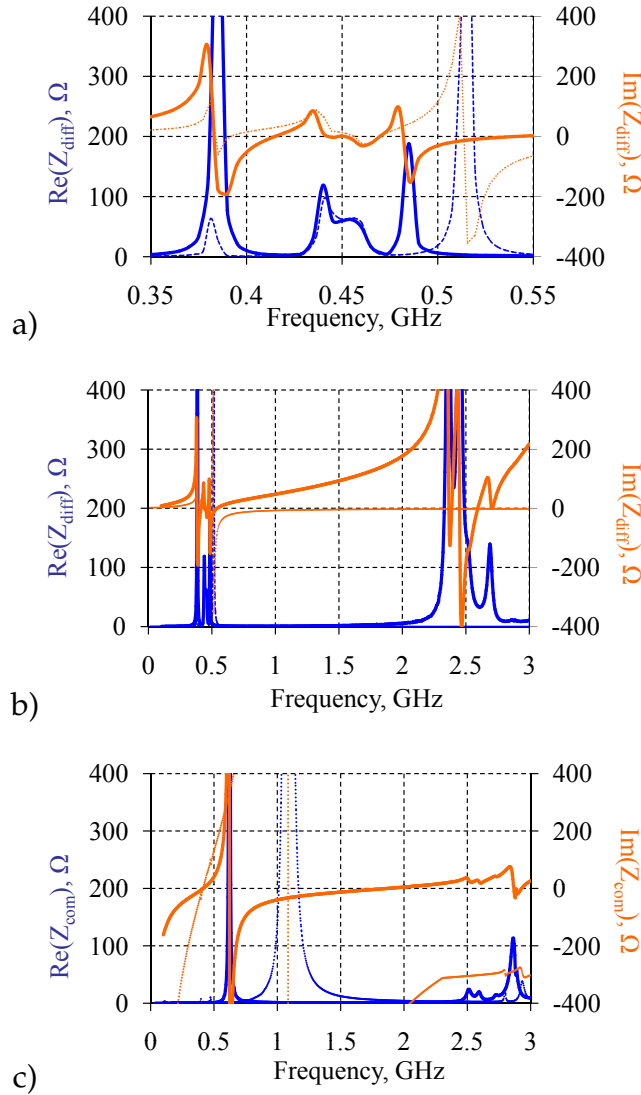


Figure 4.3.10: The measurement results (solid lines) and ADS simulation results (dotted lines) of the BICLF with a PSN: real and imaginary parts of the differential-mode impedance (in different scaling in panels a and b) and common mode impedance (in panel c).

over the frequency range from DC up to 2 GHz, excluding that around the centre frequency ($f_0 - \frac{\Delta f_{SH}}{2}; f_0 + \frac{\Delta f_{SH}}{2}$) with $\Delta f_{SH} = 200$ MHz. The differential mode reactance, however, grows as frequency rises, inserting some phase shift between the filter pins. Another disadvantage of this architecture is the complicated adjustment process, because the filter has six degrees of freedom - three tunable distributed capacitance at the ends of resonators and three trimmers. This design also suffers from low-ohmic common-mode impedance. This degradation may be caused by self-resonances in the lumped elements (most probably in the commercial inductors) and would require further improvement to out-of-band behaviour, which could be achieved by use of PSN elements with better performance.

This section has presented the BICLF with a PSN, which combines the features of a CLF and a balun. Because the PSN will provide galvanic isolation of the filter input from the filter housing, it is possible to mount both the BICLF and the final stage on the common ground, which makes this architecture an attractive candidate for a reconstruction filter for a CMCS PA system. Although the design of the filter has good characteristics in-band, there is some room for further improvements to the out-of-band behaviour, also to the somewhat complicated tuning process.

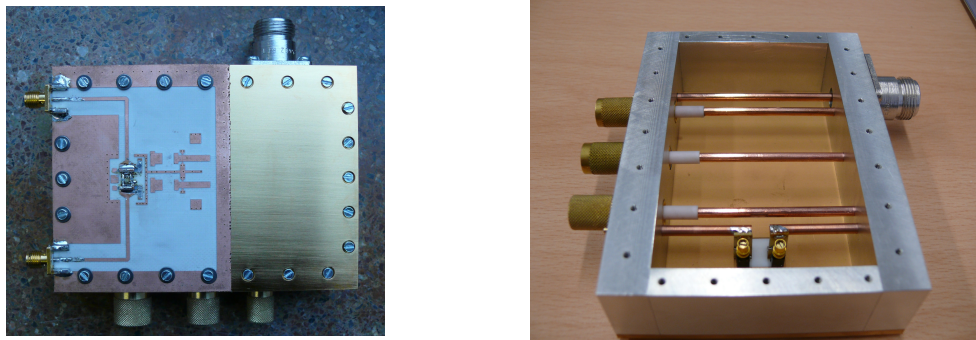


Figure 4.3.11: Photograph of the BICLF with a PSN (top view with mounted test PCB and inside view).

4.3.3 Filters with an electrically-long input loop

It has been made clear that it is necessary to isolate the filter input from the common ground; a second means of doing this would be to employ a floating electro-magnetic input loop: this novel architecture is proposed in the following section and an implementation, doubly and singly terminated, is then presented.

A. DT BICLF with an electrically-long input loop

The schematic layout of a BICLF with an electrically-long input loop is shown in Fig. 4.3.12. It consists of a CLF and a parallel capacitor C_{SH} . Because the input loop is now electrically isolated, the PSN can be reduced to one single element, the parallel capacitor C_{SH} . Another advantage of the architecture is that it is possible to supply DC power to the transistors through the floating input loop, as was shown by the present author in [103], who suggested connecting the DC power supply to the input loop through a suitable DC filter. In order to enhance suppression of the common mode, it was found to be necessary to position the DC filter 5 mm below the physical middle of the loop. However, because of the possibility that the DC filter may affect the filter characteristics out-of-band, the current study is restricted to the BICLF without DC supply.

In-band, because in this architecture the field distribution along the first resonator determines the electrical currents through the input loop, a phase shift of 180° is possible between the filter pins, constituting differential excitation. The input impedance of this mode will depend on both the line impedance and the electrical length of the input loop, which will act as an impedance transformer. The impedance transformation effect of the electrically-long input loop can be estimated if the loop is first described as a short-circuited coupled transmission line with the input impedance:

$$z(\omega) = jZ_{loop} \cdot \tan \left[\gamma(\omega) \frac{l_{loop}}{2} \right], \quad (4.3.2)$$

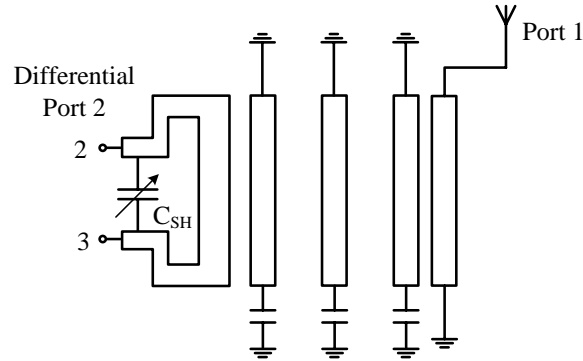


Figure 4.3.12: A third-order BICLF with an electro-magnetic input loop consisting of a CLF and a tunable shunt capacitor.

where Z_{loop} is the characteristic impedance, depending on the line geometry, l_{loop} is the physical length, and $\gamma(\omega)$ is the complex propagation constant of the transmission line. The phase delay in the input loop may also affect suppression of the common mode, which is already aggravated by the ungrounded construction of the input loop.

Out-of-band, the short-circuiting can be realised through the floating input loop for the lower frequencies. The short for the harmonics of the drain current at the higher frequencies involves designing the input loop so that it will short them discretely. As can be seen from Eq. 4.3.2, the electrically-long input loop will have self-resonances at the frequencies where its electrical length is equal to $(\frac{\lambda}{4} + 2\pi n)$. For example, an input loop with a physical length of $l_{loop} = 134 \text{ mm}$ will have self-resonances at frequencies of 1.12 GHz, 3.36 GHz, and so on. If the shunt capacitor C_{SH} is tuned, it will be possible to shift all these self-resonances to the lower frequencies and to keep their periodicity. The result is that a BICLF with an electrically-long input loop can fulfil the requirements of a CMCS PA system if driven by signals with discrete spectra, e.g., a PLM or a BP-PLM; but not if driven by a $\Delta\Sigma\text{M}$.

In order to evaluate insertion losses, parasitic coupling, and reflection loss due to impedance mismatches, it is necessary to use Ansoft HFSS software for the design and simulation. The tunable high-power coaxial CLF presented in the previous section (and designed in Ansoft HFSS) serves as a basis for the

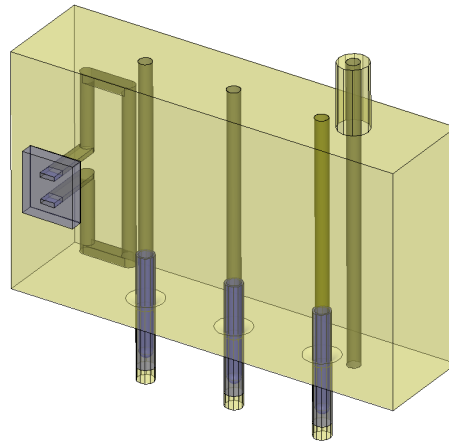


Figure 4.3.13: The HFSS sketch of a coaxial third-order BICLF with an electrically-long input loop.

current design. The modelling process and simulation modes in HFSS software having been described above, only certain specific design features are described here. The electro-magnetic input loop is connected to the final stage through the PTFE window in the top wall of the filter housing, as illustrated in Fig. 4.3.13. Because of its length ($l_{loop} = 134 \text{ mm}$) and positioning, the input loop is coupled with the first resonator by both electric and magnetic fields. The E-field strength along the first resonator changes in a sinusoidal manner, as seen in Fig. 4.3.14,

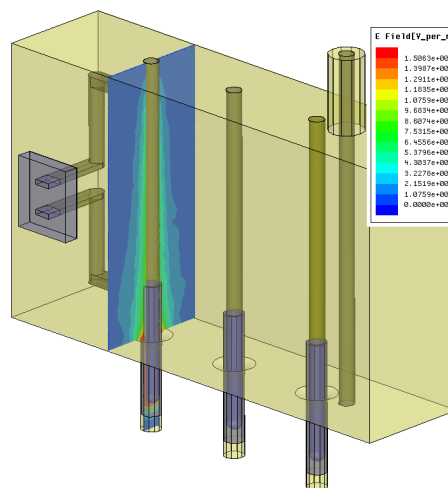


Figure 4.3.14: The HFSS sketch of a third-order BICLF with an electrically-long loop. There is a visualisation of the E-field strength pattern along the first resonator.

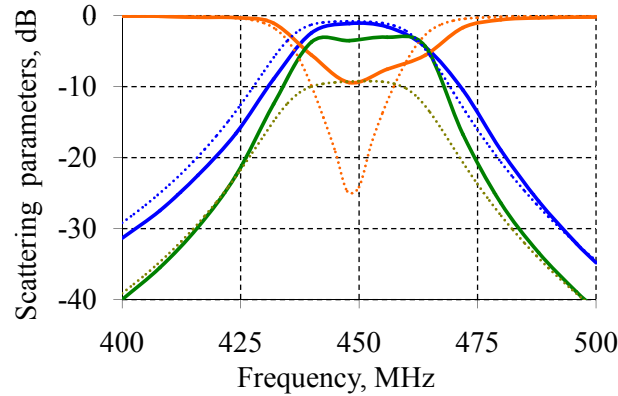


Figure 4.3.15: The measurement (solid lines) and EM-simulation results (dotted lines) of the BICLF with electrically long loop: S_{D1} - blue curve, S_{DD} - orange curve and S_{C1} - green curve.

and may lead to poor suppression of the common mode S_{C1} . The degree of this asymmetry directly depends on the electrical length of the input loop. However, it is possible to obviate this shortcoming by loading the first resonator symmetrically [109], or by modifying the filter as in [110], or by reducing the electrical length of the input loop.

Interestingly, when EM-simulation was carried out, it indicated that the shunt capacitor might shift the self-resonances of the loop, if excitation is in differential mode, though not in common mode; moreover, the higher value of this capacitor would provide the short-circuiting at higher frequencies. In EM-simulation, the shunt capacitor was set at 2.2 pF. At the same time, the periodic behaviour of the common-mode input impedance out-of-band depends on the electrical length of the loop only. Therefore, in the filter design, there is a trade-off between the length of the input loop and shunt capacitor setting, because they both influence the input impedance of the loop in-band. The EM-simulation results are represented by dotted lines in Figs. 4.3.15-4.3.16. The filter with differential-mode input impedance of 68Ω has an insertion loss of less than 0.3 dB, and a return loss better than 30 dB. As was expected, the common mode is suppressed in-band by 10 dB only. The filter being doubly terminated, it has a pronounced maximum in the differential input impedance at 400 MHz. To analyse the out-of-band behaviour: under DC the filter has zero impedance

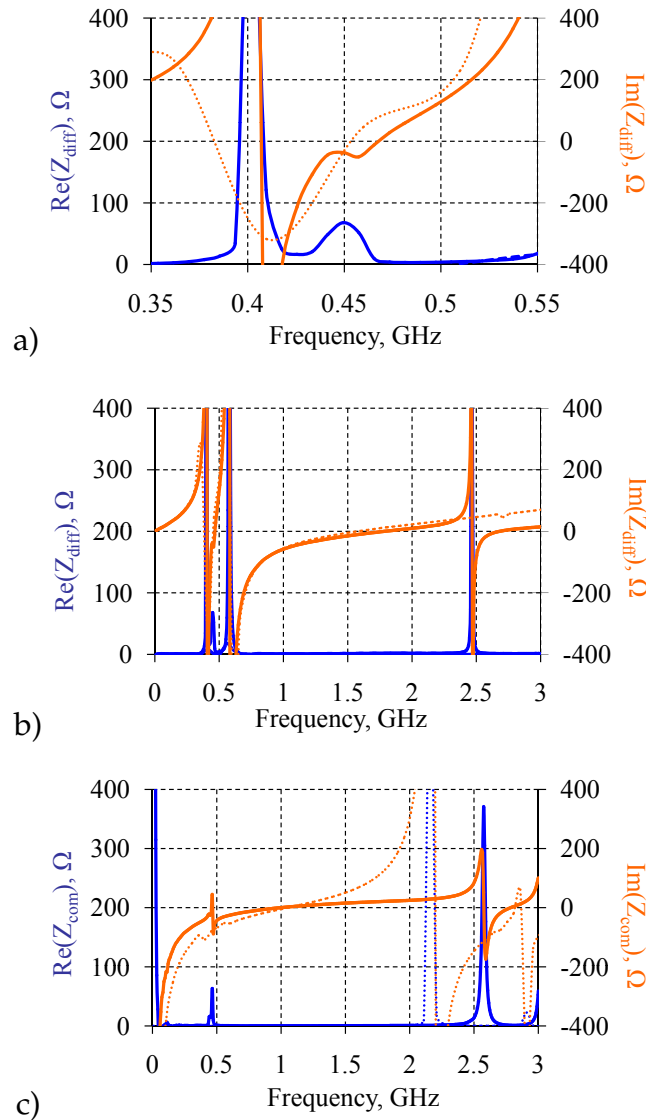


Figure 4.3.16: The measurement (solid lines) and EM-simulation results (dotted lines) of the BICLF with an electrically-long loop: real and imaginary parts of the differential-mode impedance (in panels a and b) and common mode impedance (in panel c).

for the differential mode and high-ohmic impedance for the common mode. As was expected, the electrically-long input loop (which is in parallel to the shunt capacitor) exhibits periodic behaviour. The filter has low-ohmic differential-mode input impedance and, at the same time, high-ohmic common-mode im-

pedance over the frequency range from 1.6 GHz to 2.2 GHz (see Fig. 4.3.16), fulfilling the requirements out-of-band. If this frequency range is to be extended, there are two degrees of freedom, i.e. the electrical length of the loop and the shunt capacitor.

The BICLF as designed up to this point was manufactured and experimentally investigated. The filter housing was fabricated from brass, measuring $105\text{ mm} \times 78\text{ mm} \times 30\text{ mm}$ in size, as shown in Fig. 4.3.17. The input loop and the output line, and the three resonators were copper rods with a radius of 1.5 mm. The material used for both the dielectric window in the top wall and the isolating rings at the ends of resonators was PTFE. The insertion loss of the filter is 1 dB, return loss 10 dB, and suppression of the common mode is poor. In comparison with the simulation, the quality of the filter characteristics is less satisfactory, which is probably the effect of the physical elements utilised. It is necessary to increase the common-mode impedance out of band as it will currently satisfy the requirements only at DC.

This section has presented a novel architecture for a BICLF, involving an electrically-long loop, which has properties of both a CLF and a balun. The main advantage of this architecture is that the floating loop provides the short-circuit at the DC, so that galvanic isolation is no longer required. Because it is possible to design the input loop so that it shorts the harmonics of the drain currents discretely, this architecture can fulfil the requirements of a CMCS PA

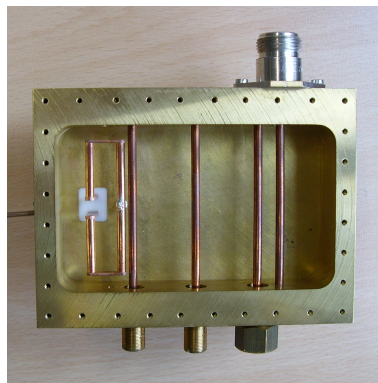


Figure 4.3.17: Photograph of the BICLF with an electrically-long loop (inside view).

system when driven by signals with discrete spectra, e.g., a PLM or a BP-PLM, but not when driven by a $\Delta\Sigma\text{M}$. Further investigation will still, however, be required if the filter is to be adapted to any specific modulator scheme.

B. ST BICLF with an electrically-long input loop

To consider now the same architecture, but this time singly terminated; certain features of the present design require separate treatment. Firstly, to provide suppression in the common mode of excitation for the singly terminated version, the first resonator was loaded by the lumped capacitances at the both ends, as was proposed in [109]. For the same reason, the input loop was designed as a high-ohmic suspended microstrip line so as to eliminate the capacitance against ground and, thereby, suppress the common mode. It was nonetheless impossible to isolate the input loop from the common ground completely, because at high frequencies the input loop is grounded through the first resonator. Secondly, the singly terminated filter was designed so that it was possible to eliminate a shunt capacitor at the filter input and to provide the short-circuiting of the drain currents through the input loop only. In the filter design there was again a trade-off, this time between the electrical length of the loop and critical coupling between the loop and the first resonator.

For test purposes, an ST BICLF with an electrically-long input loop was implemented in microstrip technology on a Rogers substrate RO4003 ($\epsilon_r = 3.55$

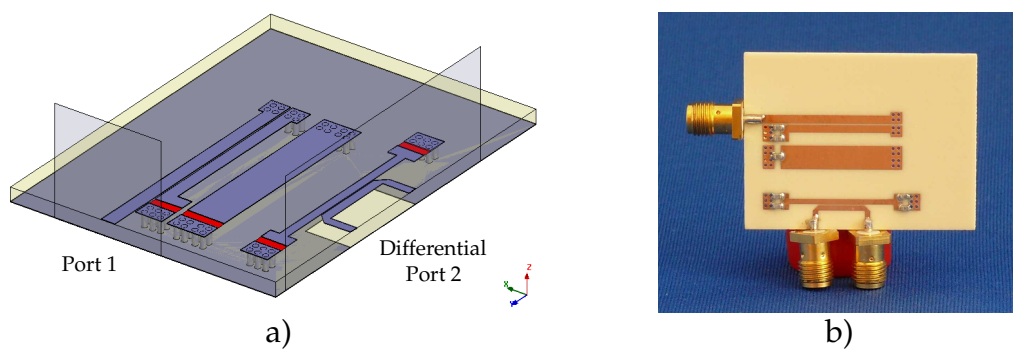


Figure 4.3.18: The HFSS sketch (in panel a) and a photograph (in panel b) of the microstrip third-order ST BICLF with an electrically-long input loop.

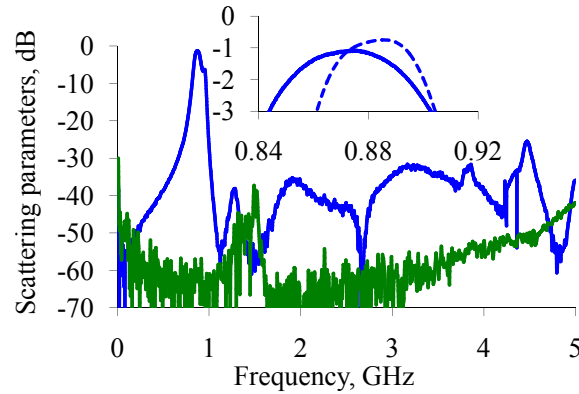


Figure 4.3.19: The measurement (solid lines) and EM-simulation (dotted lines) results of the ST BICLF: S_{D1} - blue and S_{C1} - green curves.

and $\tan(\delta) = 0.0027$) with a thickness of 1.524 mm . The filter was designed for a centre frequency of 900 MHz and input impedance of $\text{Re}(Z_{diff}) = 130 \Omega$. Fig. 4.3.18,a displays an HFSS sketch of a BICLF in which the electrical length of the resonators is $\lambda/12$ and which measures $40 \text{ mm} \times 30 \text{ mm} \times 1.524 \text{ mm}$. The suspended microstrip line used for the input loop had high impedance and was positioned in 5 cm away from the next grounded planes. The EM simulation results are the dotted lines in Figs. 4.3.19-4.3.20. The filter exhibits a differential input resistance of 130Ω and an insertion loss of 0.8 dB over a 3-dB pass-band $885 \pm 20 \text{ MHz}$. The differential mode resistance is less than 13Ω , as shown in Fig. 4.3.20,b, and remains almost constant from DC up to around 5.7 GHz . At the same time, the common-mode input reactance takes high-ohmic values in DC and drops to zero at around 3 GHz . This result thus approximates very closely to the mixed-mode S-matrixes of Eqs. 3.2.5-3.2.8.

For the purposes of the current study this device too was manufactured and experimentally investigated: there is a photograph of it in Fig. 4.3.18,b. The lumped-elements DLI high-voltage capacitors (C06-CF) were mounted on the filter surface. For the final tuning, high-quality Tecelec trimmers (27281SL) at the ends of the resonators were used. In order to maintain the simulation conditions, it was necessary to measure the filter, when it was positioned at a distance from the common ground. The experimental results are presented in

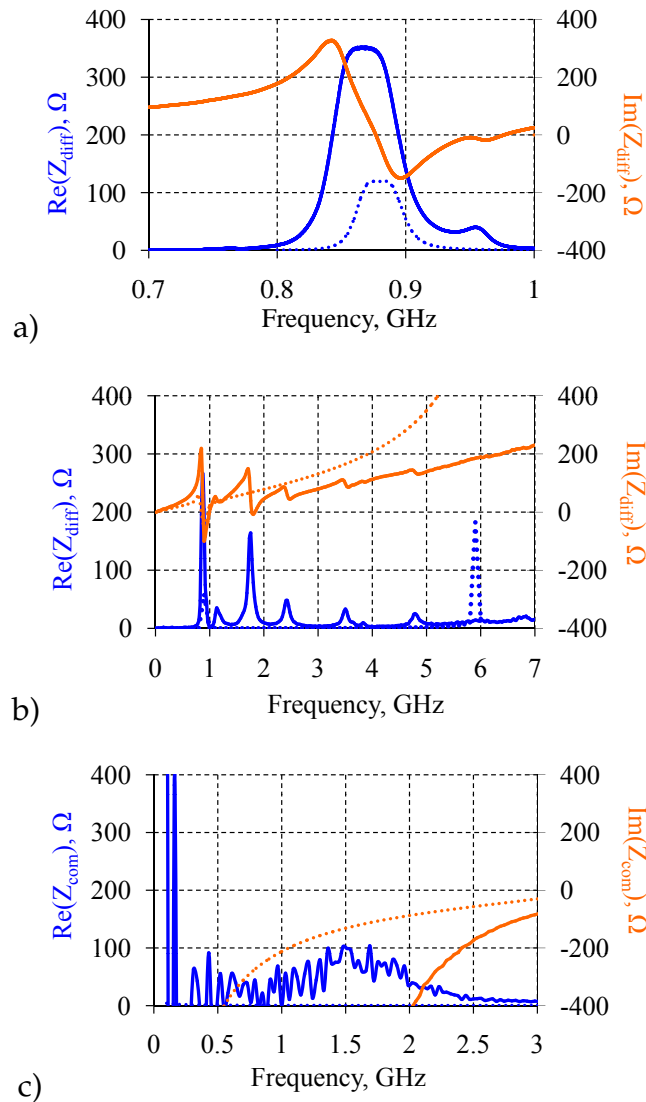


Figure 4.3.20: The measurement (solid lines) and EM-simulation (dotted lines) results of the ST BICLF: real and imaginary parts of the differential-mode impedance (in panels a and b) and common mode impedance (in panel c).

Fig. 4.3.19. Owing to the low dielectric losses of the substrate and the high quality of the SMD components, a low insertion loss, of 1 dB, was achieved. The filter provides a 3-dB bandwidth of 60 MHz and a broad stop-band up to 20 GHz with suppression of 20 dB. The input impedance in-band is 350 Ω , which is higher than it was in simulation. The common mode transmission remains below 55 dB in-band, sufficiently low to meet the requirements of switched mode

power amplifiers. In the pass-band, as is typical of ST filters, the BICLF exhibits a flat input resistance, as shown in Fig. 4.3.20 [105]. To analyse the filter characteristics out-of-band: although the differential-mode input reactance linearly increases as frequency grows, the differential-mode filter resistance is low-ohmic up to 7 GHz excluding the frequencies where the input loop has self-resonances. At the same time, the common-mode reactance is high-ohmic up to 3 GHz. Although the differential-mode input impedance is higher than it was in EM-simulation, the BICLF demonstrated several valuable features: the good measurement results out-of-band, flat in-band resistance and a very broad stop-band.

This section has presented the ST BICLF with an electrically-long loop combining the properties of both a CLF and a balun. The floating input loop will provide the short-circuit of the drain currents not only in DC, but also at higher frequencies. The filter demonstrates high suppression of the common mode in-band, achieved by symmetrical loading of the first resonator. From the analysis carried out it can be concluded that this architecture is capable of fulfilling the requirements of a CMCS PA system.

4.3.4 Alternative design with an electrically-short input loop

To take now the last architecture for balanced input reconstruction filters: the circuit layout of a BICLF with an electrically-short input loop is presented in Fig. 4.3.21. It consists of a parallel capacitor C_{SH} and a CLF, connected to the amplifier stage through the floating input loop, which is represented by its equivalent inductance L_{loop} in Fig. 4.3.21. The key factor is that the input loop here is electrically short and at the centre frequency acts as a line element to excite the first resonator; it has self-resonances at frequencies higher than $5f_0$. In this architecture it is possible to eliminate asymmetry, to suppress common-mode and to minimise losses. Out-of-band, as in previous architectures, the floating loop provides the short-circuiting between the filter pins in DC; and the shunt capacitor C_{SH} shorts the harmonics at higher frequencies. A coaxial DT BICLF with an electrically-short input loop was designed with the aid of HFSS soft-

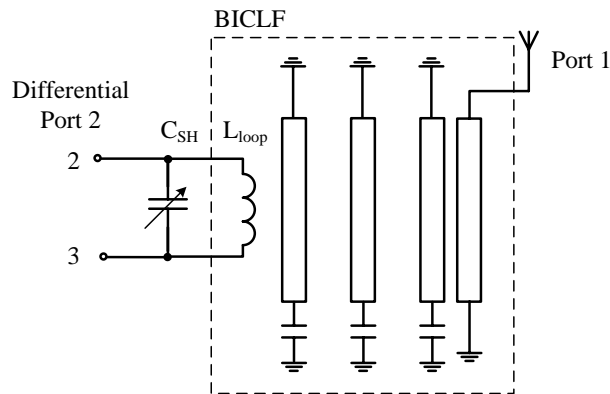


Figure 4.3.21: A third-order BICLF with an electrically-short input loop consisting of a CLF with a tunable shunt capacitor. The electrically-short input loop is represented by its equivalent inductance L_{loop} .

ware. The sketch is shown in Fig. 4.3.22. The device as now designed operates at a centre frequency of 900 MHz, and so the physical length of the resonators was shortened to 28 mm. In order to realise impedance transformation from the differential port with an input impedance of 130 Ω to the antenna port, the resonators were designed with unequal radii. Although the input loop and the first resonator should logically have smaller radius reflecting the higher input impedance, the effect would be that current density increased, with an insertion loss. For this reason, the radius of the first resonator was increased, and

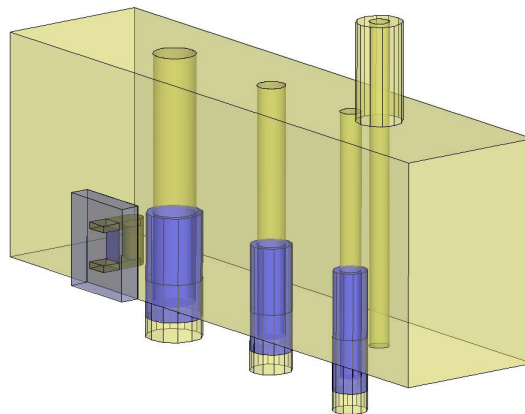


Figure 4.3.22: The HFSS sketch of a coaxial third-order BICLF with an electrically-short input loop.

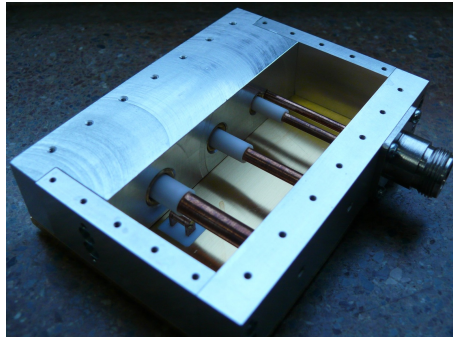


Figure 4.3.23: Photograph of the BICLF with an electrically-short input loop (inside view).

this step impedance was compensated by the lumped capacitance at the end of the first resonator. Next, the loop was placed in the area with the highest E-field strength along this resonator, in order to achieve the critical electro-magnetic coupling. As before, the input loop is split by a 50Ω coupled line and connected to the final stage through a PTFE window in the top wall. The length of the input loop was reduced to 21 mm at most, so that it has its first self-resonance at around 7.15 GHz (see Eq.4.3.2). At this length the input loop can be represented up to 3 GHz by its equivalent inductance $L_{loop} = 4.26 \text{ nH}$. The filter was manufactured and experimentally investigated. Fig. 4.3.23 is a photograph of the BICLF, the dimensions are $105 \text{ mm} \times 78 \text{ mm} \times 30 \text{ mm}$. (The filter

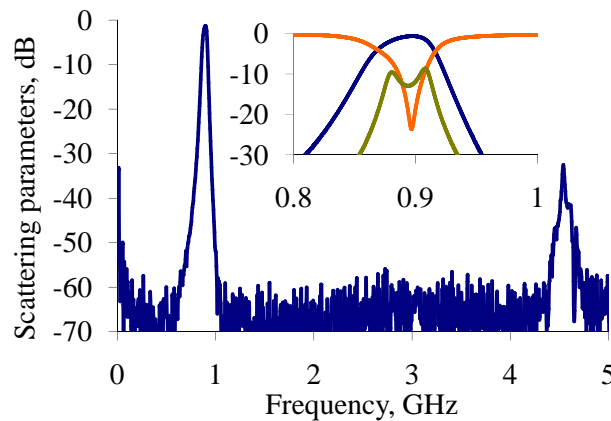


Figure 4.3.24: The measurement results of the BICLF with an electrically-short loop: S_{D1} - blue, S_{DD} - orange and S_{C1} - green curves.

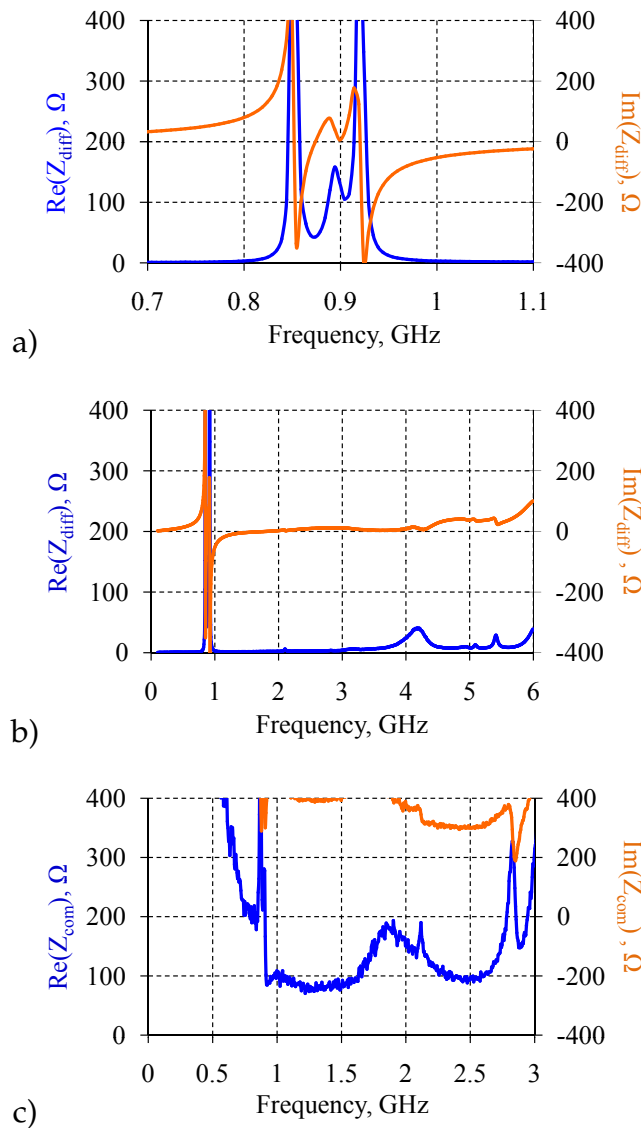


Figure 4.3.25: The measurement of the BICLF with an electrically-short input loop: real and imaginary parts of the differential-mode impedance (in panels a and b) and common-mode impedance (in panel c).

interface has been kept so as to remain compatible with different generations of the CMCS PAs.) The lumped-element DLI high-voltage capacitor (C06-CF) was mounted close to the amplifier stage. As shown in Fig. 4.3.24, the filter provides a measured insertion loss of 0.54 dB, a 3-dB-bandwidth of 46 MHz, and a second pass-band at 4.5 GHz [104]. The common-mode was suppressed

by 13 dB. In-band the BICLF exhibits maxima in the differential mode impedance, which are explained by the doubly terminated filter design. Out of band the filter demonstrates impressive results, depicted in Fig. 4.3.25. In DC the input loop provides the short-circuiting for the differential mode and high-ohmic impedance for the common mode. The differential-mode impedance reaches a value of less than 13Ω at only ± 112 MHz offset from the centre frequency, remaining at a low-ohmic level from the DC up to the second pass-band. The common mode impedance takes a high-ohmic value over the frequency range from the DC up to 3 GHz. Thus, in- and out-of-band characteristics correspond well to the filter requirements expressed by Eqs. 3.2.5-3.2.8. Nevertheless, stronger common mode suppression and single termination would serve to improve the filter characteristics in-band.

This section has presented the BICLF with an electrically-short input line which will have a wide stop-band, high power capability, narrow bandwidth, and low insertion loss, as is typical of CLFs. At the same time, this architecture has advantages over those described earlier in this dissertation, because the floating electrically-short input loop provides short-circuiting of the drain currents in DC, and does not involve periodicity out of band.

4.4 Conclusion of the design and implementation of reconstruction filters

This chapter has presented the design and implementation of reconstruction filters for a CMCS PA system, which can be described in summary as follows.

1. The electrical and geometrical constraints found on analysis for the reconstruction filter in a CMCS PA system for BTS application can be satisfied by a mechanically-tunable high-power coaxial CLF. In the filter design there will be a trade-off between the insertion loss, second pass-band, selectivity and degree of miniaturisation of the filter.
2. In contrast to DT filters, ST reconstruction filters will provide lower inser-

tion loss and at the same time will have constant in-band input resistance.

3. The BICLF with a straight loop, having the properties of a CLF and a balun, will succeed in fulfilling all the requirements for a CMCS PA system. However, galvanic isolation of the filter housing from the common ground will be required.
4. In order to obviate galvanic isolation, the BICLF has been developed with a PSN. As this device (BICLF with a PSN and final stage) can be mounted on the common ground, the architecture is an attractive candidate for a reconstruction filter for a CMCS PA system.
5. The BICLF with an electrically-long input loop combining properties of both a CLF and a balun is a version which has the main advantage of a galvanically isolated input loop. Because it is possible to design the input loop so that it shorts the harmonics of the drain currents discretely, this architecture can fulfil the requirements of a CMCS PA system when driven by signals with discrete spectra, e.g., a PLM or a BP-PLM, but not when driven by a $\Delta\Sigma\text{M}$.
6. The BICLF with an electrically-short input loop will have wide stop-band, high power capability, narrow bandwidth, and low insertion loss, as is typical of CLFs. At the same time, this architecture has advantages over the architectures presented above, because the floating electrically-short input loop provides short-circuiting of the drain currents in DC, and does not involve any periodicity out-of-band.

In order to complete the reconstruction filter analysis, the following chapter will present simulation and measurement of a CMCS PA system and a CMCD PA system, in which the filter architectures proposed are employed.

5 Influence of the reconstruction filter on the power amplifier performance

Various architectures of a reconstruction filter having been proposed, this chapter will now present an implementation and analysis of all the complete switching amplifier systems in which these architectures are employed. In order to evaluate the potential impact of the building blocks, the first section of this chapter will describe a class-D PA system simulated for conditions in which both the transistors and the filter circuit contain their parasitic elements. The second section will discuss the ADS simulation results of a class-S PA system under a variety of driving conditions. The measurement results of the class-S demonstrators will be discussed in the last section of this chapter and the filter architectures comprehensively analysed.

5.1 Simulation of reconstruction filters in class-D RF PA systems

A class-D PA being a particular case in class-S PA systems, its simulation can be considered as a necessary interim step taken in order to estimate the loss mechanisms in the switching transistors, to optimise the system for efficiency and output power, and to evaluate the impact of the filter termination on the PA performance. The class-D PA is a complicated system and requires detailed investigation because each of its blocks may have a similar distorting effect on the whole PA system. The various separate effects having been described in [55], certain of them will be reconsidered when the reconstruction filter is the focus of discussion.

5.1.1 Simulation engines in ADS software

There are various analysis techniques for simulating distortion in nonlinear circuits and systems in ADS software, some of which can be applied to the present analysis, e.g. harmonic balance, transient analysis, S-parameters, AC, and others [111, 112]. The circuit under analysis will be the deciding factor as to which simulation engine is chosen and which parameters used. As they are simulation engines in both frequency-domain and time-domain, the harmonic balance and the transient techniques will be described here in detail. To take the harmonic balance simulation engine first: the spectral content of voltages or currents in the circuit are calculated in steady-state conditions and then are converted in time-domain with the aid of the truncated Fourier series. A consequence of this engine is that it is possible to simulate a class-S PA system when driven by signals with discrete spectra, e.g., a PLM or a BP-PLM, but not when driven by a $\Delta\Sigma$ M. For the last case, the advanced time-domain transient simulation engine can be applied, which calculates integro-differential equations for the currents and voltages of the circuit at each moment of time. As it is not possible in this engine to compute the frequency-dependent distributed elements (microstrip elements, S-parameter blocks, and so on), it is necessary to replace them by their equivalent circuits. This section presents an analysis of a CMCD PA system in both simulation engines when the reconstruction filter is a lumped-element, balanced-input BPF.

5.1.2 Transistor model

Because they offer high breakdown voltage and handle high power density over the broad frequency range, the AlGaIn/GaN HEMTs are attractive candidates for BTS application [113]. Because they may reduce the performance of the modulated signals and thus of the whole amplifier system, it is necessary to take into account and simulate the parasitic elements in the transistors. For instance, the drain-source capacitance will influence the transition time, and the ON-resistance will increase dissipation losses in the transistors. Commercially

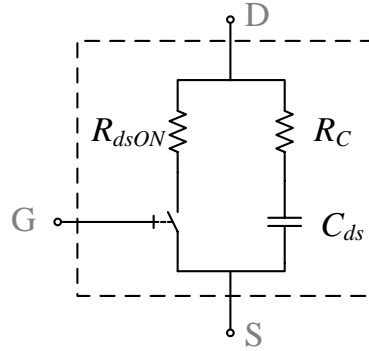


Figure 5.1.1: The simplified switch-based model of the GaN HEMT [3].

available $8 \times 250 \mu\text{m}$ AlGaIn/GaN HEMTs supplied by FBH in Berlin can be represented in ADS software by their large-signal Angelov model described in detail in [3]. The model used in the current study is the simplified switch-based type shown in Fig. 5.1.1. In the model, there are an ideal switch which has a drain-source ON-resistance of $R_{dsON} = 3 \Omega$ and a drain-source OFF-resistance of $R_{dsOFF} = 1 \text{ M}\Omega$; a parallel drain-source capacitance of $C_{ds} = 0.248 \text{ pF}$ and a conducting resistor of $R_C = 10.46 \Omega$. This simplified model has the advantage of being applicable in both simulation engines and under any driving conditions.

5.1.3 Power characteristics

A CMCD PA system, as shown in Fig. 5.1.2, consists of a 50% duty cycle square wave generator, a push-pull amplifier with the simplified switch-based transistor model, biasing network (RF chokes $L_{ch} = 1.1 \mu\text{H}$ and voltage supply V_{cc}), a reconstruction BPF, a balun and 50Ω load. In order to evaluate the impact of the filter termination on the power characteristics for the present purpose, two balanced input third-order BPFs with Butterworth transfer function were designed, doubly and singly terminated. The filters have differential-mode input impedance of 40Ω (optimal for a class-D PA in Eq. 2.3.11), a bandwidth of 26 MHz at a centre frequency of 450 MHz, an insertion loss of 0.5 dB, which would mark a degradation of the overall efficiency by a factor of 0.9. First, the

appropriate currents and voltages for the circuit have to be found. In order to not exceed the maximum available drain voltages and currents, it is necessary for the voltage supply to be limited to a maximum of [32]

$$\hat{V}_{cc} = \frac{V_{dmax}}{\pi} + \frac{R_{dsON} \cdot I_{dmax}}{2}, \quad (5.1.1)$$

which is 17.5 V for the present GaN transistors. This supply voltage was applied to the RF chokes, through which the currents flow:

$$I_0 = \left(\frac{2}{\eta_{pA_{class-D}}} \right)^2 \cdot \left(1 + \left(\frac{2}{\eta_{pA_{class-D}}} \right)^2 \cdot \frac{2 \cdot R_{dsON}}{R_l} \right)^{-1} \cdot \frac{V_{cc}}{R_l}, \quad (5.1.2)$$

where $\eta_{pA_{class-D}}$ is the peak amplitude coding efficiency of a class-D PA system and is equal to $\frac{4}{\pi}$ (see Eq. 2.3.13). For the system in question, the choke current I_0 is 0.75 A and the maximum drain currents are $I_1 = I_2 = 2 \cdot I_0 = 1.5$ A. The output current and voltage are:

$$\begin{aligned} I_l &= S_{D1}(\omega_0) \cdot I_0 \cdot \eta_{pA_{class-D}} \\ V_l &= S_{D1}(\omega_0) \cdot I_0 \cdot \eta_{pA_{class-D}} \cdot R_l, \end{aligned} \quad (5.1.3)$$

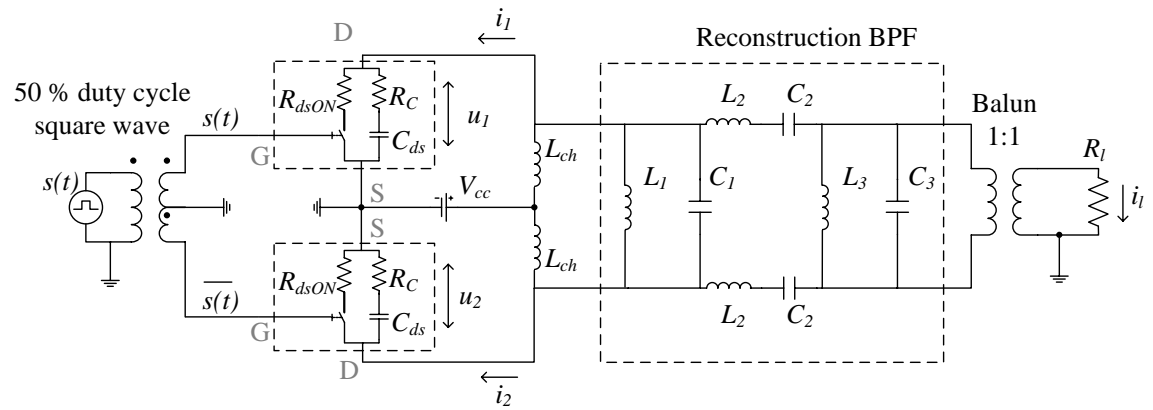


Figure 5.1.2: A CMCD PA system comprising a 50% duty cycle square wave generator, a push-pull amplifier on GaN transistor models, biasing network (RF chokes L_{ch} and voltage supply V_{cc}), a third-order lumped-element reconstruction BPF and a balun.

and are equal to 0.9 A and 41 V. Under such loading conditions the drain voltages reach the peak values:

$$V_1 = V_2 = V_l + R_{dsON} \cdot I_1, \quad (5.1.4)$$

and are equal to 45 V.

Following the calculation of circuit currents and voltages, the two PA systems were simulated for the purposes of the current study in both harmonic balance and transient regimes. The simulated waveforms, plotted in Fig. 5.1.3, agree with analytical results. In both simulation engines, the power characteristics are identical, as presented in Table 5.1.1. Although the maximum drain efficiency can theoretically reach 84% (see Eq. 2.3.12), in simulation it is 62% at most, which represents an "inaccessible upper limit" for the drain efficiency of a class-S PA. This low drain efficiency is a cumulative effect of the losses in the reconstruction filter and of the parasitic elements in a GaN transistors. There arises the question of which constituent has the most impact on the drain efficiency. In order to answer this question, it is necessary to simulate a CMCD PA system, in which all but one of these parasitic elements has been eliminated, the effect of which can then be evaluated. So far, it is only clear that both simula-

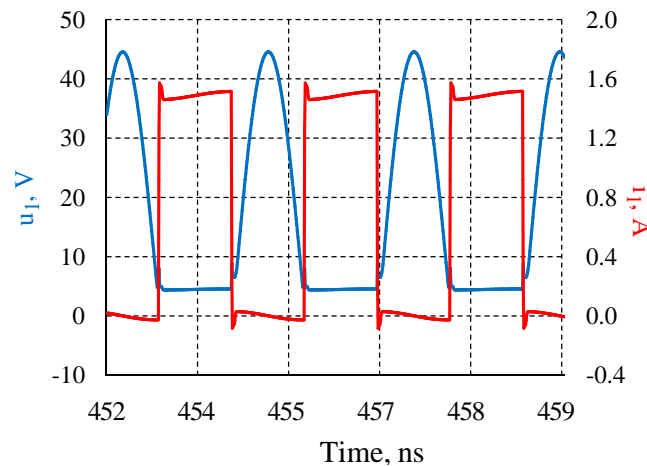


Figure 5.1.3: The simulated waveforms of the drain voltage and drain current in the CMCD PA system as shown in Fig. 5.1.2.

Table 5.1.1: The drain efficiency and output power of the CMCD PA system computed in different simulation engines.

Simulation engine	η_D (%)	$P_{RF_{out}}$ (W)
Transient analysis	62	16
Harmonic balance	65	17

tion engines show identical results and the filter termination has no influence on the PA characteristics at the centre frequency. For all ensuing simulations, one engine only is employed.

5.1.4 Impact of parasitic components in the GaN HEMTs

This section will analyse the potential impact of the parasitic components in the GaN HEMTs on the power characteristics of the system and on the waveforms of the drain currents. To consider the power characteristics first: as the sources of dissipative losses in transistors are R_{dsON} and R_C , the following four different CMCD PA systems will be analysed: with an ideal switch; with a switch including ON-resistance only; with the simplified switch-based model of the GaN HEMTs, as shown Fig. 5.1.1; and with the Angelov Model of the GaN HEMTs presented in [3]. The simulation results are presented in Table 5.1.2. Because of the losses in the reconstruction filter, it was possible to achieve a maximal drain efficiency of only 87% when the ideal switches were employed. The further drain efficiency drop to 64% (or by a factor of 0.74) was the effect of the ON-resistance only, while it was found that the elements $C_{ds}R_C$ do not affect the system characteristics at all. As can be seen, if the drain efficiency is to be improved, it is necessary to reduce the ON-resistance.

Turning to the parasitic components in the GaN transistors: in order to evaluate their impact on the shape of the drain currents, four designs of a CMCD PA system were again simulated: with an ideal switch and without filter; with the simplified transistor model and without filter; with both the sim-

Table 5.1.2: ADS simulation results of the CMCD PA with different transistor models.

Transistor model	η_D (%)	$P_{RF_{out}}$ (W)
Ideal switch ($R_{dsON} = 0 \Omega$)	87	30
Lossy switch ($R_{dsON} = 3 \Omega$)	64	17
Simplified model from Fig. 5.1.1	62	16
Angelov Model	61	15

plified transistor model and the filter (for $Q=20$ and $Q=0.2$, where the quality factor Q has been calculated from $Q = \omega_0 R_l C$ [55]). In order to minimise its influence, the reconstruction filter was simplified to an LC parallel circuit, with a resonance frequency at f_0 and a variable Q-factor. The simulation results are presented in Fig. 5.1.4. The drain currents are rectangular in shape only when the switches are ideal, as represented by the dotted blue line in Fig. 5.1.4. Although there has been a claim that the losses in the C_{ds} are negligible in a CMCD PA system [114] (because the drain-source capacitance is shorted and cannot be discharged in on-state), the C_{ds} being parallel to the OFF-switch will have the

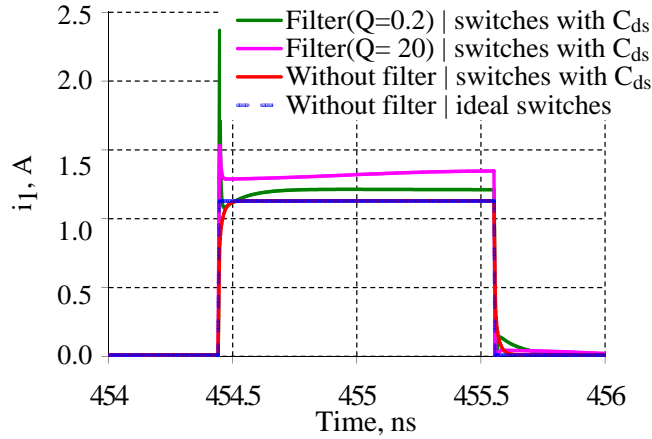


Figure 5.1.4: The shape of the drain current of the class-D PA in different driving conditions.

effect of increasing the rise time in the drain current pulses, as shown by the red curve in Fig. 5.1.4. Also, if the CMCD PA system employs both the transistor model and the filter circuit, which have been presented here, there will be damped oscillation in the drain currents in dependence on both the time constant $\tau_{RC} = C_{ds} \cdot R_C$ and the Q-factor of the filter (green and violet curves in Fig. 5.1.4). From the results presented, it can be concluded that the parasitic components in the GaN HEMTs may affect not only power characteristics of the PA system, but also the shape of the drain currents.

5.1.5 Effect of parasitic components in the filter

Because the actual reconstruction filters may contain also some parasitic elements, it is necessary to evaluate influence of these on the PA performance. It has been made clear above that it is necessary for the filter to have high-ohmic common-mode input impedance, which will at most be affected by capacitances against ground. It is important to note that because the reconstruction filters presented in the previous section were in the main doubly terminated, in this section the DT filter will be the focus of investigation. However, capacitances to ground will have the same effect out-of-band on either DT or ST filters. To facilitate investigation of how these capacitances to ground C_g affect the shape of the drain currents, they were positioned at the filter input, as shown

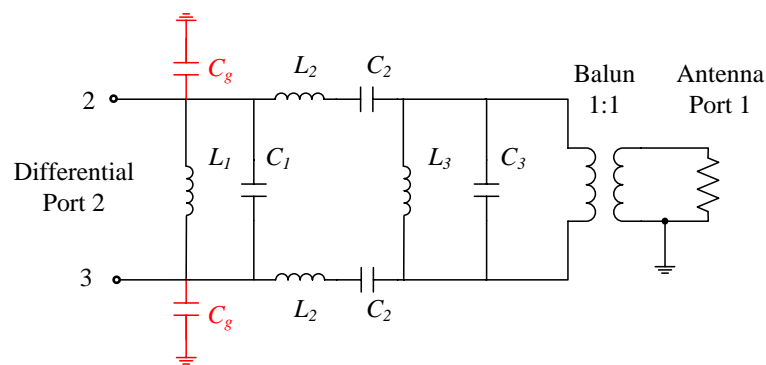


Figure 5.1.5: A balanced input BPF with parasitic capacitances to ground C_g at the filter input.

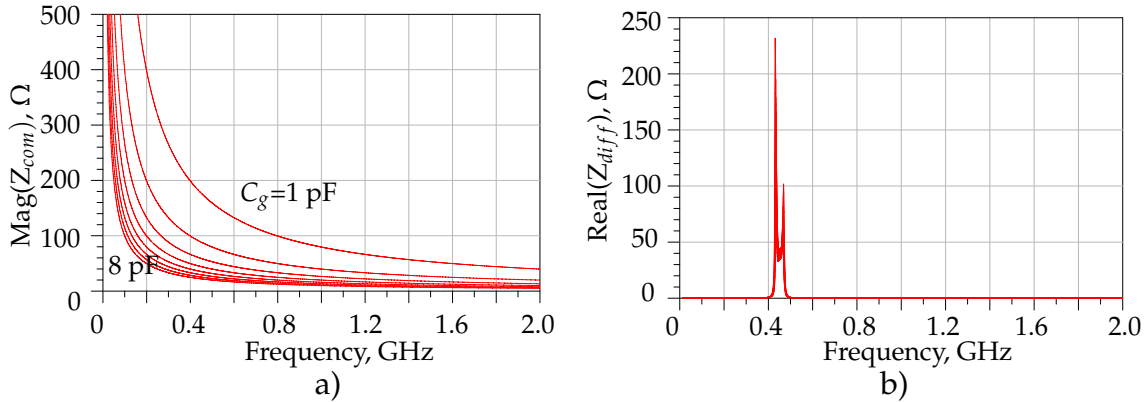


Figure 5.1.6: ADS simulation results of the balanced input BPF at 450 MHz with parasitic capacitances to ground: the magnitude of the input impedance for the common mode (in panel a) and the input resistance for the differential mode of excitation (in panel b). The common-mode input magnitude is infinite when $C_g = 0$ pF.

in Fig. 5.1.5. The input impedance for both modes of excitation was simulated with varying capacitances, from 0 pF to 8 pF. The simulation results are presented in Fig. 5.1.6,a-b. The effect of these capacitances on the differential-mode input impedance out-of-band is nil, because of the maintenance of the symmetrical filter structure. The capacitances to ground have a major influence on the common-mode input impedance out-of-band, which diminishes as C_g rises. Because the filter here is a floating device, the input impedance for the common mode will depend on the ground capacitance only, $Z_{com} = \frac{1}{2\pi f 2C_g}$. There arises the question of what effect this diminished common-mode impedance has on the power characteristics and on the shape of the drain currents. In order to answer this question, the CMCD PA system from Fig. 5.1.2 using the filter circuit from Fig. 5.1.5 was simulated in ADS software. The results are presented in Figs. 5.1.7 - 5.1.8. The first of these two figures illustrates how the capacitance to ground at different values from 0 pF to 8 pF may change the shape of the drain currents (shown by the arrows). As can be seen, these ground capacitances have a similar effect to that of the drain-source capacitance in the transistors; the only difference is that C_g affects the drain currents in the ON-state only, whereas C_{ds} does so in both the ON-state and the OFF-state. From the analysis depicted in the figure, it can be taken that it is not possible to compensate the drain-source

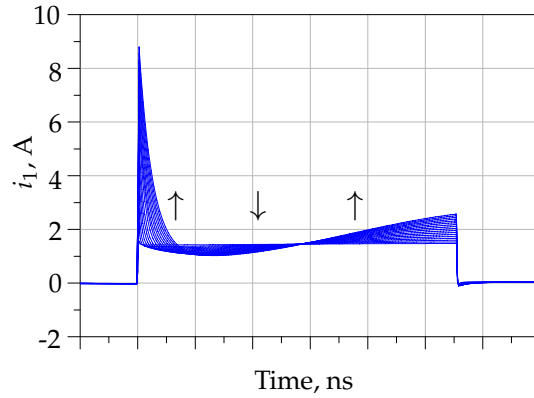


Figure 5.1.7: The ADS simulation results: change of the shape of the drain currents (shown by the arrows) when the capacitance to ground grows (the shape close to rectangular corresponds to $C_g = 0$).

capacitance C_{ds} in the first resonator of a reconstruction filter.

The power characteristics of the amplifier system in Fig. 5.1.2 are also affected by these capacitances, as shown in Fig. 5.1.8,a. Because the reactive currents flow through the capacitances to ground, the currents through the switches rise as C_g grows, which results in increased dissipating power in the switch ($\frac{1}{2}I_1^2 R_{dsON}$), as shown in Fig. 5.1.8,a. At the same time, output power is constant, because it is compensated by the diminishing output voltage. The diminished drain efficiency becomes potentially significant at 45% when C_g is 8 pF, and negligible when C_g is less than 2 pF (the total capacitance to ground is then 4 pF), which corresponds to common-mode impedance of less than 40 Ω at 2 GHz. Because the impact of these capacitances depends on the operation frequency, simulation of a CMCD PA system was repeated, but this time 900 MHz. The common-mode impedance of the filter for 900 MHz is identical to that for 450 MHz, as shown in Fig. 5.1.6,a. The simulation results are presented in Fig. 5.1.8,b. The degradation of drain efficiency will be significant at 30% when C_g is 8 pF, and can be taken as negligible when C_g is less than 2 pF (the total capacitance to ground is then 4 pF), again corresponding to common-mode impedance of less than 40 Ω at 2 GHz. As can be seen, the CMCD PA system operating at 900 MHz is more affected by these capacitances to ground, because all the higher harmonics of the drain currents are now shorted to ground which

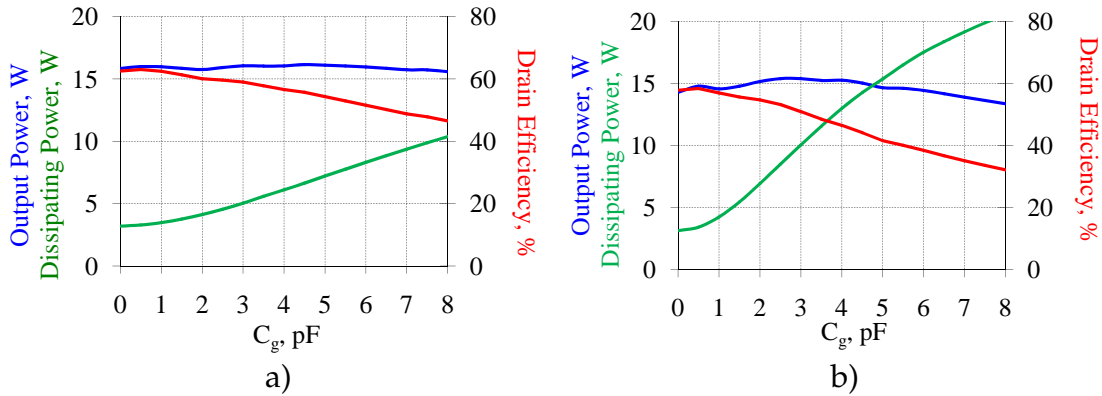


Figure 5.1.8: The ADS simulation results of the CMCD PA system operating at 450 MHz (in panel a) and the CMCD PA system operating at 900 MHz: drain efficiency (red curve), output power (blue curve) and dissipating power in the switch, $\frac{1}{2} I_1^2 R_{dsON}$, (green curve) as functions of the parasitic capacitance to ground C_g .

increases the current through the switches and thus the dissipating power in these. It can, however, be concluded that because the filter architectures presented in the previous chapter, for example, the BICLF with an electrically short loop (see Fig. 4.3.25) and the ST BICLF (see Fig. 4.3.20), demonstrated even better characteristics out-of-band, they will not significantly affect the PA performance. Nonetheless, it is necessary to reduce these capacitances to ground as much as possible, for they may occur not only in a reconstruction filter, but also in a mounting board, in biasing networks, or in MMICs, are thus a challenge not to be neglected.

5.1.6 Influence of the filter termination

Another potential source of distortion is the filter termination. In order to assess the impact of type of filter termination on the PA performance in-band, ADS simulation of the CMCD PA system from Fig. 5.1.2 was repeated, sweeping the centre frequency of the RF signal, and the results are shown in Fig. 5.1.9. It was necessary first to simulate both filters in S-parameter simulation engine to establish their basic characteristics. As can be seen, the both filters have a flat transfer function over the bandwidths, as shown in Fig. 5.1.9,a. The difference in

the filter terminations is visible only from the simulated reflection coefficients, and the Smith Chart is used in Fig. 5.1.9,b to show this. The analysis which now follows was carried out in the transient simulation engine and all the PA characteristics were computed for each frequency point. Fig. 5.1.9,c shows the output power for both cases. As was expected, the double termination results in pronounced maxima in the output power. In contrast, it was found that the ST filter provides constant output power. (It is important to note that in order to simulate here the ideal current source, it was necessary to choose a suitable value of the RF chokes.) The drain efficiency is illustrated in Fig. 5.1.9,d. For both cases the drain efficiency has a similar shape, with the minimum at the centre frequency. The significant differences become apparent when frequency rises. This effect can be explained by the analysis of the peak drain voltage in Fig. 5.1.9,e, where it is seen to grow rapidly at the edges of the pass-bands and overdrive the transistors. In practice, such high drain voltages will damage GaN transistors and operation in back-off will be required. Because the drain voltages out-of-band are tripled, the DT filter represents a more critical case. At the same time, the dissipating power in the switch ($\frac{1}{2}I_1^2R_{dsON}$) in both cases, seen in Fig. 5.1.9,f to grow in offset from the centre frequency, is mainly caused by high drain voltages. It is important to note that the PA characteristics also depend on the filter structure.

This section has presented the effect of the filter termination on the PA performance. It was found that the DT filters will result in pronounced maxima in drain voltages, in drain efficiency, and in output power. In order to provide constant output power, it is necessary not only that the reconstruction filter be singly terminated, but also that the final stage act as an ideal current source.

5.2 Simulation of reconstruction filters in class-S PA systems

The CMCD PA system having been analysed in terms of different aspects, it was taken in this piece of research as the basis for the design and simulation

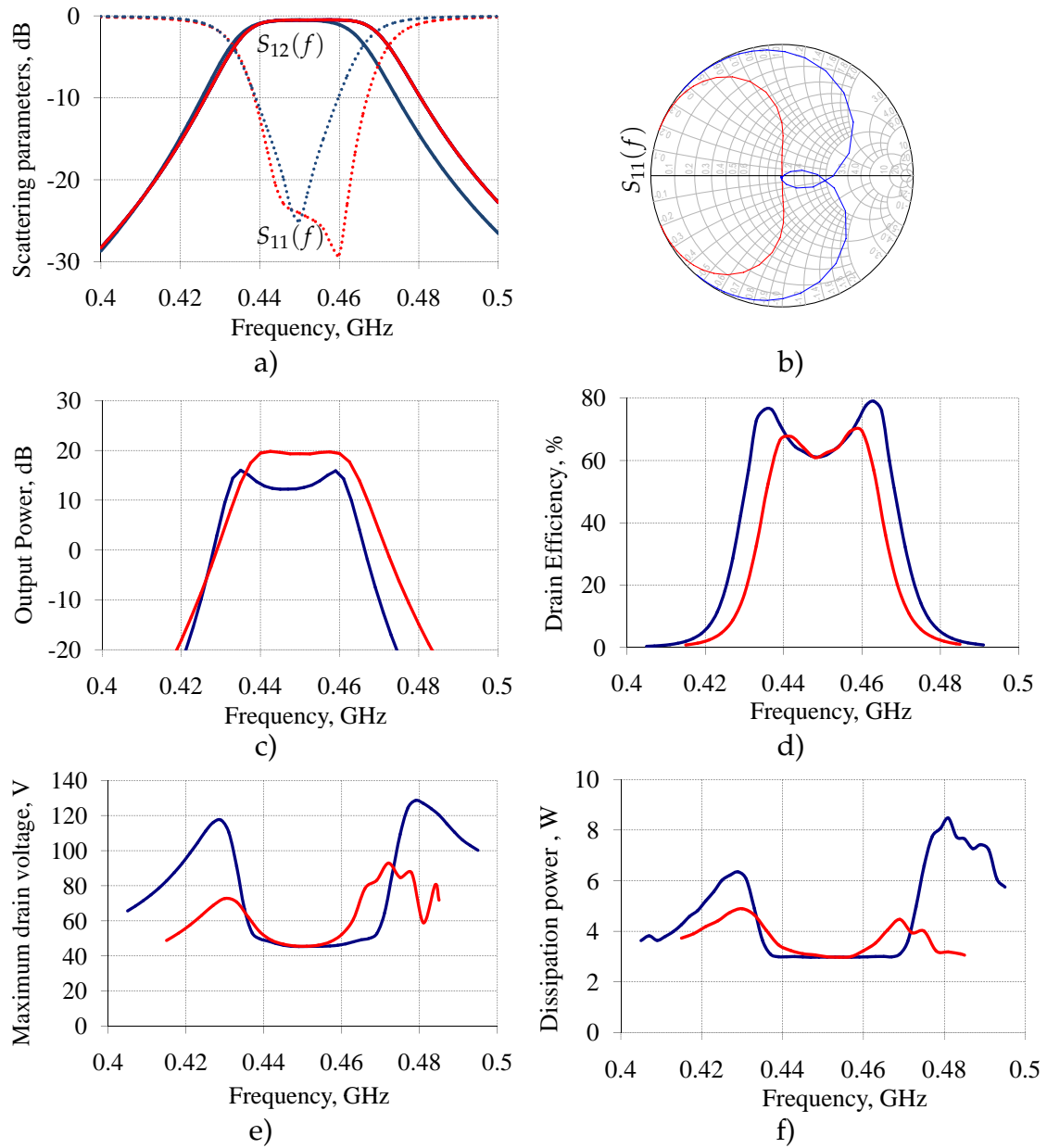


Figure 5.1.9: ADS simulation results of the class-D PA with the ST filter (red curves) and the DT filter (blue curves) as functions of sweeping centre frequency: a) - scattering parameters, b) - Smith chart, c) - output power, d) - drain efficiency, e) - maximum drain voltage, f) - dissipating power in the switch, $\frac{1}{2}I_1^2 R_{dsON}$.

of a CMCS PA system. For clarity, it is necessary at this stage to point out some features of the following analysis. Firstly, because negative drain voltages may occur in the OFF-switch and damage MMICs, in practice Schottky protection diodes are required in the drain path. In the current study, because the switches are somewhat simplified for simulation purposes and the third-quadrant effect cannot be observed, these diodes are eliminated. Secondly, because simulation in harmonic balance demonstrated an unexpected third-quadrant effect, only the transient simulation engine is employed for the ensuing analysis. Thirdly, because the GaN HEMTs demand deep negative swing drive voltage, which cannot be ensured by the modulator used, in practice there is a need for a pre-amplifier. Again, in the current study this pre-amplifier stage is eliminated. Finally, investigation of effect of the filter termination having revealed that it has no effect at the centre frequency, it proved to be sufficient to analyse a CMCS PA system for one type of the termination only, for example a DT filter. For the purposes of the current study, the choice fell on a DT, lumped-element, third-order balanced-input Butterworth BPF (designed for the purpose). This filter has a bandwidth of 26 MHz at a centre frequency of 450 MHz, input impedance of 65Ω , and insertion loss of 0.5 dB. Because the parasitic elements in the system blocks will have the same effect here as in a class-D PA system, this section will present only the power characteristics of a class-S PA system under a variety of driving conditions.

5.2.1 Class-S system with a pulse-length modulator

To take a CMCS PA system when driven by a PLM first: this system consists of a PLM, a push-pull amplifier on the GaN transistor models, a biasing network (RF chokes L_{ch} and voltage supply V_{cc}), a reconstruction filter, and a balun, all of which are shown in Fig. 5.2.1. The PLM was designed using RF voltage sources, a sawtooth signal generator and a comparator, as shown in Fig. 2.3.6.a. For the comparator, a symbolically-defined block in ADS software was used which specifies the algebraic relationships between the voltages.

First, it was necessary to find the appropriate currents and voltages for

the circuit mathematically. To take a CMCD PA system described in the previous section as a basis for the present system: if the supply conditions are maintained, all the currents and voltages entirely depend on the peak amplitude coding efficiency. For the PLM with $\eta_{P_{\text{sinus}}} = 0.447$ (see Table 2.3.2) and an one-tone RF signal with a crest factor of $c_f = \sqrt{2}$, the peak amplitude coding efficiency can be found from Eq. 2.3.10:

$$\eta_{pA} = \sqrt{\eta_{P_{\text{sinus}}}} \cdot c_f, \quad (5.2.1)$$

and is 0.95. The choke current, calculated from Eq. 5.1.2, is 0.85 A. The drain currents are then 1.7 A. Because the present peak amplitude coding efficiency is lower than $\eta_{pA_{\text{class-D}}} = 4/\pi$, both the DC current and the drain currents are lower than in a class-D PA system under the same supply conditions. On determining the output current and output voltage for the system in question using Eq. 2.3.3, they are found to be $I_l = 0.76$ A and $V_l = 38$ V. The peak drain voltage, calculated from Eq. 2.3.5, is limited to 54.5 V. In the present system design, it is theoretically possible for drain efficiency to reach a maximum of 57% (see Eq. 2.3.9).

Following the calculation of circuit currents and voltages, two designs

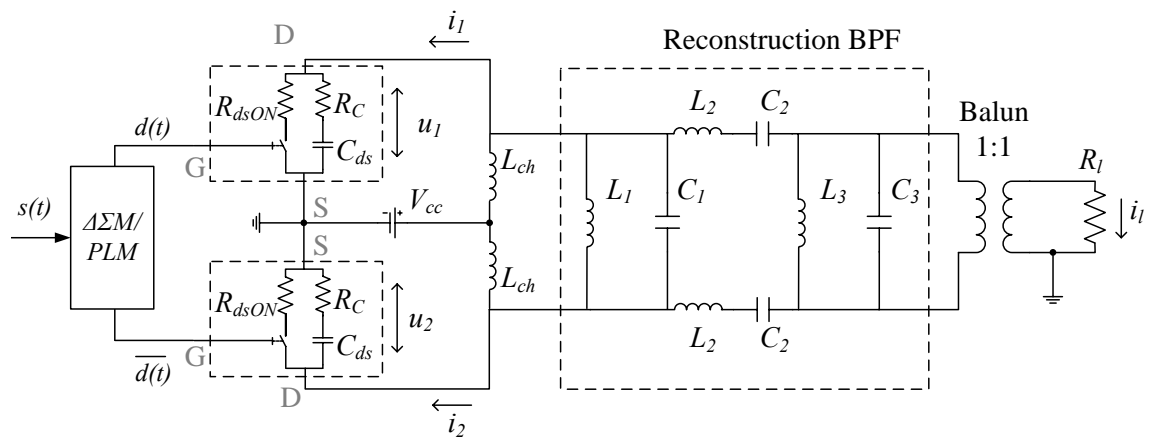


Figure 5.2.1: A CMCS PA system comprising a one-bit modulator, a push-pull amplifier on GaN transistor models, biasing network (RF chokes L_{ch} and voltage supply V_{cc}), a reconstruction band-pass filter, and a balun.

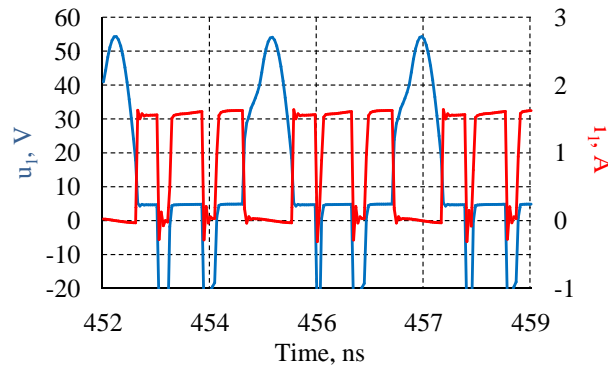


Figure 5.2.2: ADS simulation results: drain voltage and current of the CMCS PA when driven by the PLM one-tone signal.

of a CMCS PA system were simulated, one in which the switch was the simplified model (see Fig. 5.1.1) and the other in which the switch was an ideal type without resistive and capacitive losses. The simulation results for the first design are presented in Fig. 5.2.2. As can be seen, the shape of the drain current is distorted similarly to that shown in Fig. 5.1.3, a phenomenon caused by charging of the drain-source capacitances in the switch model. The simulation and calculation results agree quite well, excepting for higher load current and load voltage, $I_l = 0.83 \text{ A}$ and $V_l = 41.5 \text{ V}$. This slight disagreement is attributed to an effect of impedance transformation in the reconstruction filter, which was not taken into account in Eqs. 2.3.3-2.3.5. It is important to note that this simulation was repeated when the filter had both input and output impedances of 50Ω , and that the simulation then fully coincided with calculation results. The power characteristics for both systems are presented in Table 5.2.1. For the system in question, the drain efficiency of 60% is close to its theoretical maximum. From the analysis presented in the table, it can be concluded that the decrease in drain efficiency to 60% is an effect of the parasitic elements in the GaN transistors at most (by a factor of 0.7), and of insertion loss in the reconstruction filter (by the factor of 0.85, which is close to 0.9 as expected). Thus, the parasitic elements in the GaN transistors affect the performance of the system at most, as in the case of the class-D PA system.

Table 5.2.1: ADS simulation results: drain efficiency of the CMCS PA system when driven by the PLM.

Modulator	Transistor model	η_D (%)
PLM	Ideal switch	85
	Simplified model from Fig. 5.1.1	60

5.2.2 Class-S system using a delta-sigma modulator

Another possible realisation of a CMCS PA system would be to drive it by means of a $\Delta\Sigma$ M. The appropriate currents and voltages for the circuit first have to be found mathematically. If a class-D PA system from the previous section serves as a basis for the present amplifier system and if the supply conditions are maintained, all the currents and voltages will depend on the peak amplitude coding efficiency only. For an one-tone $\Delta\Sigma$ -modulated signal, the peak amplitude coding efficiency, calculated from Eq. 5.2.1, is equal to $\eta_{pA} = 0.97$. Because this is almost equal to the peak amplitude coding efficiency in case of the PLM from the previous section, and the same calculations are done, the currents and voltages can be expected to have the same peak values.

In ADS software it is possible to design a $\Delta\Sigma$ M as the circuit from Fig. 2.3.4, or as a "Data Access Component", which contains a data stream of a $\Delta\Sigma$ -modulated signal as simulated or as measured. In the current study, a data stream as measured will be used, one which was supplied by the IHP GmbH in Frankfurt/Oder, Germany. Due to the special interpolation mode in transient simulation engine, both systems (with a "Data Access Component" and with a $\Delta\Sigma$ M as a circuit), shown in Fig. 5.2.1, were investigated. The simulated waveforms of the drain voltage and drain current are shown in Fig. 5.2.3. In spite of the expectation, the peak values of the drain current and drain voltage, $I_1 = 3.8 A$, and $V_1 = 74 V$, are markedly higher than in case of the PLM. In contrast, the simulated load current and voltage, $I_l = 0.84 A$ and $V_l = 42 V$, are only half of the calculated values. It might be supposed that these high drain currents

and voltages are the effect of impedance transformation in the reconstruction filter. This assessment has not been confirmed, because the ADS simulation repeated for the filter without impedance transformation gave the same results. This uncertainty may be the effect either of incorrect calculation of either the peak amplitude coding efficiency, or of a calculation method which is no longer accurate. Both suppositions require further investigation. Although the drain efficiency can theoretically reach 57%, in simulation of both CMCS PA systems, it was only 27%. In order to estimate which constituent has the most impact on the drain efficiency, both PA systems were simulated with ideal switches and simplified switch-based models. Both implementations of the $\Delta\Sigma$ M showed similar low drain efficiency for both CMCS PA systems: these simulation results are presented in Table 5.2.2. As can be seen, this degradation in drain efficiency is the effect of insertion loss in the reconstruction filter, by a factor of 0.75, although a factor 0.9 was expected. The parasitic elements in the GaN transistors decrease drain efficiency by a factor of around 0.4.

In this section it has been shown that the one-bit modulator is a crucial element of a class-S PA system, because it has a strong impact on the performance of the whole PA system and may aggravate the impact of the other system elements. In a system with the present GaN transistors, the modulator will considerably decrease drain efficiency, and, at the same time, the impact of the insertion loss in the filter will be reinforced, so that it would be impossible in practice

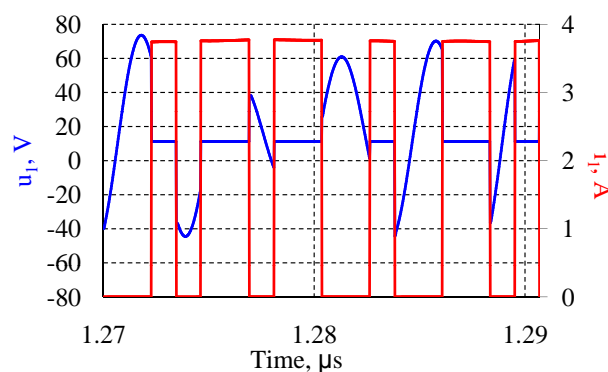


Figure 5.2.3: The ADS simulation results: drain voltage and current of the CMCS PA when driven by the $\Delta\Sigma$ M one-tone signal.

Table 5.2.2: ADS simulation results: drain efficiency of the CMCS PA system under a variety of driving conditions.

Modulator	Transistor model	η_D (%)
$\Delta\Sigma M$	Ideal switch	75
	Simplified model from Fig. 5.1.1	34
$\Delta\Sigma M$ ("Data Access Component")	Ideal switch	73
	Simplified model from Fig. 5.1.1	27

to estimate its actual influence. From the analysis presented it can be concluded that the $\Delta\Sigma M$, being the most critical element of the class-S PA system requires modification to improve coding efficiency and to avoid its aggravating effect on the impact of the other system elements.

5.3 Overview of class-S demonstrators

Both SMPA systems having been investigated by means of computer simulation, it is necessary for the purposes of the current study to analyse the measurement results of these systems. This section will analyse several CMCS PA systems which have been assembled and experimentally investigated in the context of work in the Mobile-GaN research program. There have been other power amplifier systems which engendered interest on the part of academic institutions. For instance, the CMCD PA system with EER technique was presented in a diploma thesis [115]; in that case, the BICLF was employed with an electro-magnetic input loop. Although this PA system has demonstrated good power characteristics, it required further improvements as to shape the time signals at drains.

5.3.1 Demonstrator for the TETRA frequency band

To take the demonstrator of a CMCS PA system for the TETRA frequency band at 450 MHz first: it employs GaN HEMT MMICs and GaAs Schottky diodes, which both are supplied by FBH in Berlin, Germany. The GaN HEMT MMICs were implemented on a resistively loaded $4 \times 125 \text{ mm}$ transistor stage and two $8 \times 250 \text{ mm}$ transistors in parallel, as illustrated in Fig. 5.3.1,a [13]. Fig. 5.3.1,b is a photograph of the MMIC chip, which measures $1.9 \times 2.7 \text{ mm}^2$. The pre-amplifier stage was realised on a commercial GaAs-MMIC chip. It was possible to assemble this GaAs-MMIC chip, the biasing network, and the GaN HEMT MMICs, on the Rogers substrate Ro4003, and the substrate was mounted on the coaxial reconstruction filter body, as shown in Fig. 5.3.2. For the present demonstrator the BICLF employed was that with a PSN from Fig. 4.3.11. It was necessary to mount the parallel resonant circuit of the PSN between the filter pins as close as possible to the final stage. The mechanically tunable trimmers in the PSN were used for the final tuning. Because a one-bit modulator and a pulse generator (for class-D testing) constituted optional external elements, it was possible to drive this demonstrator either in a class-S regime or in a class-D operation regime. For the class-D operation, two out-of-phase 50% duty cycle square waves which had an amplitude of 0.45 V and rise/fall time of 130 ps were generated. The final integration represented quite a challenge in view of

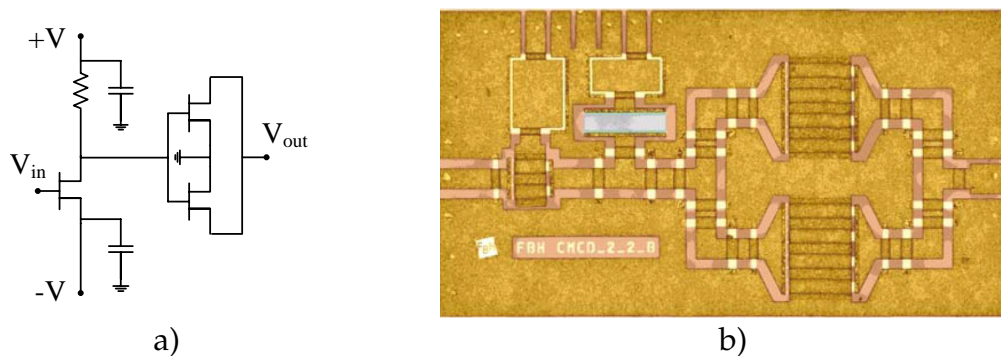


Figure 5.3.1: The schematic diagram (in panel a) and chip photograph of a 2-stage digital PA in $0.25 \mu\text{m}$ gate length technology (in panel b) [13] (source: FBH, Berlin, Germany).

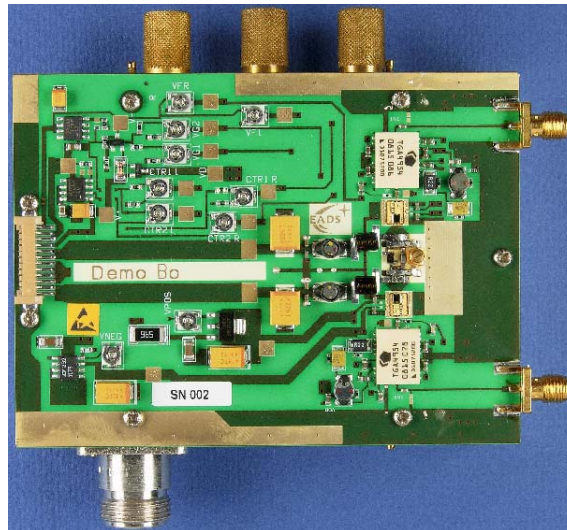


Figure 5.3.2: Photograph of the demonstrator of a CMCS PA for the TETRA frequency band. There are the high speed digital driver amplifiers, the GaN HEMT MMICs, the GaAs Schottky diodes, the biasing network, and the control circuitry. The BICLF with a PSN on the rear side serves as mounts for the PA circuitry [14].

critical heat sensitivity of the MMICs and numerous technologies needing to be assembled together. This problem was confronted by the cooperation partner of the Mobile-GaN research program, EADS Deutschland GmbH in Ulm, Germany. The integration aspects has been described in detail in [14,17].

5.3.2 Demonstrators for the GSM frequency band

The demonstrator of a CMCS PA system for the GSM frequency band was designed for a centre frequency of 900 MHz. There are three versions of this demonstrator, each implemented using different MMICs and reconstruction filters.

1. Version 1 employs GaN HEMT MMICs, supplied by FBH, and the coaxial DT BICLF with an electrically-short input loop (see Fig. 4.3.23). This demonstrator was described in [14];
2. Version 2 was implemented with GaN HEMT MMICs, supplied by IAF, and the coaxial DT BICLF with an electrically-short input loop. The demon-

strator was presented for the first time in [16];

3. Version 3 utilises GaN HEMT MMICs, supplied by IAF, and the microstrip ST BICLF.

The fact that the first version of this demonstrator differs from the demonstrator for the TETRA band only in the reconstruction filter means that the impact of the filter architecture can be evaluated here.

For the second and the third versions, the GaN HEMT MMICs were supplied by IAF in Freiburg. Because in these MMICs the depletion mode transistor and resistive load are used (see Fig. 5.3.3,a), it has proved to diminish static losses in the driver and to increase switching speed [15, 31], suggesting that the driver concept has good potential for the present application on account of the high power efficiency and high transit frequency. Fig. 5.3.3,b is a chip photograph of these MMICs, which were designed with a $0.25\ \mu\text{m}$ GaN HEMT technology and a transit frequency of 32 GHz. A photograph of the second version of the demonstrator for the GSM band is shown in Fig. 5.3.5, where the high speed digital driver amplifiers, the GaN HEMT MMICs, the GaAs Schottky diodes, the biasing network, and the control circuitry can be seen. These demonstrators were assembled similarly to the demonstrator for the TETRA frequency band. The BICLF with an electro-magnetic input loop

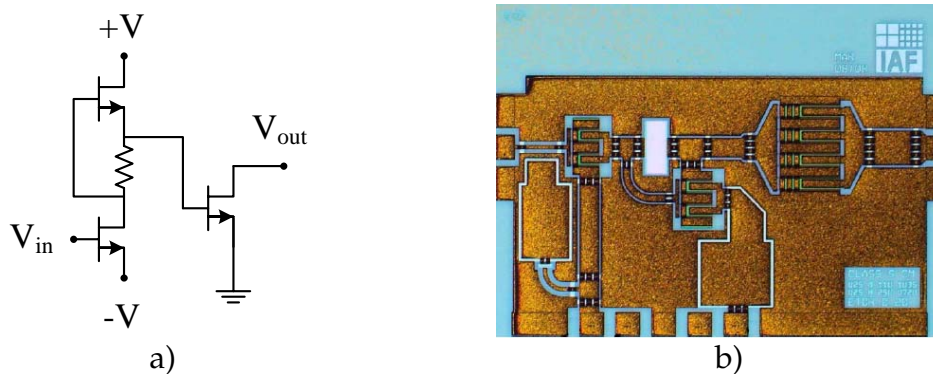


Figure 5.3.3: The schematic diagram (in panel a) and chip photograph (half area of a symmetrical chip) of a 2-stage digital PA in $0.25\ \mu\text{m}$ gate length technology (in panel b) [15] (source: IAF, Freiburg, Germany).

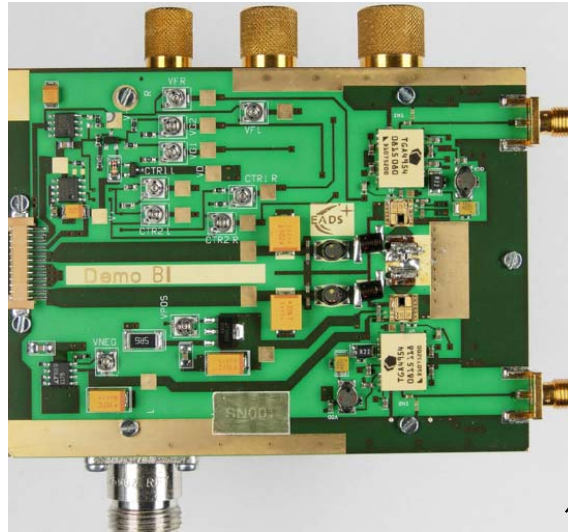


Figure 5.3.4: Photograph of the demonstrator of a CMCS PA for the GSM frequency band (version 1). There are the high speed digital driver amplifiers, the GaN HEMT MMICs, the GaAs Schottky diodes, the biasing network, and the control circuitry. The BICLF with an electro-magnetic input loop on the rear side serves as mounts for the PA circuitry [16].

(see Fig. 4.3.23) on the rear side serves as the mount for the PA circuitry [16]. Because the first and the second versions differ in their MMICs only, it will be possible to evaluate here the impact of these MMICs.

To take now the third version of this demonstrator: Fig. 5.3.5 is a photograph of it, showing the high speed digital driver amplifiers, the GaN HEMT MMICs, the GaAs Schottky diodes, the biasing network, and the control circuitry. In order to minimise parasitic capacitances to ground and to achieve compatibility with the demonstrator, the microstrip ST BICLF was mounted perpendicularly to the board. For the final tuning it was necessary to use a dielectric material, and two trimmers at the ends of the first resonator. In this demonstrator it was possible to evaluate the impact of the filter termination on the PA performance. The following section will present the measurement results for the demonstrators described.

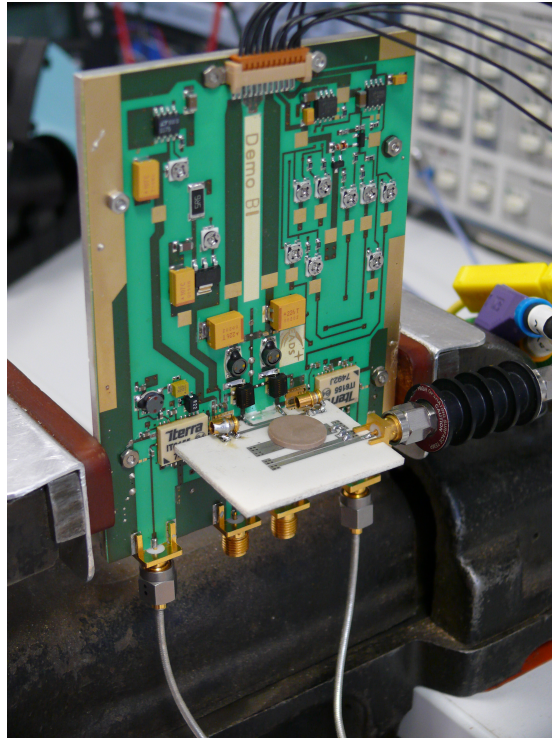


Figure 5.3.5: Photograph of the demonstrator of a CMCS PA for the GSM frequency band. There are the high speed digital driver amplifiers, the GaN HEMT MMICs, the GaAs Schottky diodes, the biasing network, the control circuitry, and the ST microstrip BICLF, which is mounted perpendicularly to the board.

5.4 Measurement results

The various demonstrators having been presented, it is necessary for the purposes of the current study to analyse their measurement results. The compatibility of the different modulation schemes with the BICLFs was investigated in [69], where the spectral measurement test procedure was proposed. In that study it was shown that it is possible for the BICLF to fulfil the requirements for frequency selectivity which were required by the conventional $\Delta\Sigma\text{M}$. This section will present the power characteristics of all the demonstrators. The broadband measurements carried out for the evaluation of the impact of the filter termination were taken during the sweep of the centre frequency of the RF signal.

5.4.1 Demonstrator for the TETRA frequency band

The measurement of the demonstrators has to be carried out in two steps [17]. Firstly, in order to find the optimal bias points for the pre-amplifier and the final stage, the filter is tuned. The tuning procedure is carried out by means of a pseudo random bit sequence generated by a FPGA board. The broad noise spectrum of the sequence means that the output signal reflects the transfer function of the filter. Secondly, the demonstrator is tested in a class-D regime when driven by 50% duty cycle square waves. The measurement results of the present demonstrator have been published in [17]. At the maximum supply voltage of 19 V, it was possible for output power to exceed the peak values of 9 W. Importantly, drain efficiency remained constant as supply voltage grew from 3 V up to 19 V, which was construed as a possible solution to the back-off problem. The measured drain efficiency, 30% (see Fig. 5.4.1), is only half of the value expected. Also, the significant distortion in the drain currents and the drain voltages observed were thought to be the cumulative effect of the interaction between the driver stage and the final stage, of the GaN HEMT MMICs with frequency dispersion, and of the affected short-circuiting between the filter pins.

To enable the demonstrator to be subjected to measurements in a class-S

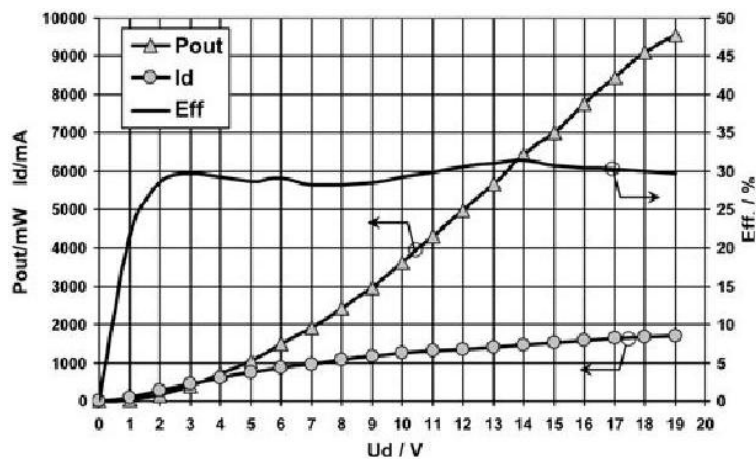


Figure 5.4.1: Typical measurement results of the class-S PA with a DT reconstruction filter operating for test purposes in a class-D regime (driven by a 50% duty cycle square wave) [17].

operation regime [17], it was driven by a $\Delta\Sigma$ -modulated one-tone signal. The amplifier system yielded maximum output power of 5.8 W and drain efficiency of 18.5%, when drain voltage was 18 V. As can be seen, both the drain efficiency and the output power are significantly impaired. There arises the question of which constituent has the most impact on the drain efficiency in practice. In order to answer this question, it will be necessary to compare these results with measurement results of the demonstrator for the GSM band, which employs the same MMICs and the reconstruction filter for a centre frequency of 900 MHz.

5.4.2 Demonstrators for the GSM frequency band

The demonstrators for the GSM frequency band were experimentally investigated in the same way as is described above.

A. Version 1

To analyse version 1 of the demonstrator first: it was possible to achieve the maximum drain efficiency of 37% at a drain voltage of 3 V. In contrast to the previous demonstrator, drain efficiency here decreases as drain voltage grows [16]. The maximum output power was 5 W at a drain voltage of 16 V: in that instance, drain efficiency had already dropped to 17% [14]. However, drain efficiency is still very low, which is probably due to the GaN HEMT MMICs with a high ON-resistance. This supposition will be confirmed, if the current version is compared with the version 2. Because in a class-S regime it was possible to achieve output power of several mW only, the demonstrator in question was tested in a class-D regime only.

It was experimentally found that distortion in the time signal at the drains is the cumulative effect of the biasing conditions of the final stage and of the GaN HEMT MMICs utilised [14]. Because under these conditions it is not possible to evaluate the impact of the filter characteristics out-of-band only, this has to be found by comparing the demonstrator version in question with the demonstrator for the TETRA frequency band [14, 17]. Because these differ only in type of reconstruction filter the study concluded that the significant improve-

ment in shape of the drain currents in version 1 was the effect of the BICLF with an electrically-short input loop. So far, it is clear that, in contrast to the BICLF with a PSN, the coaxial BICLF with an electrically-short input loop has fulfilled the impedance requirements out-of-band under the given driving conditions.

In order to evaluate the impact of the filter termination, this demonstrator was measured by sweeping the centre frequency of the RF signal. The measured output power as a function of the centre frequency is depicted in Fig. 5.4.2. As can be seen, there are unacceptable 3-dB ripples in the pass-band [76], which are caused by the double termination of the BICLF with an electro-magnetic input loop. Whether this supposition is confirmed or can be dismissed will become apparent when version 1 and version 3, with the differently terminated reconstruction filters, are compared.

B. Version 2

Version 2 of the demonstrator for the GSM frequency band was presented in [14, 16]. It employs GaN HEMT MMICs supplied by IAF, and the coaxial DT BICLF with an electrically-short input loop. The maximum output power of 5 W was achieved when drain voltage was 20 V. Drain efficiency reached a nearly constant plateau of 65% as early as at 10 V (Fig. 5.4.3,a). Because of the constant drain efficiency, this amplifier system is very attractive for the BTS application,

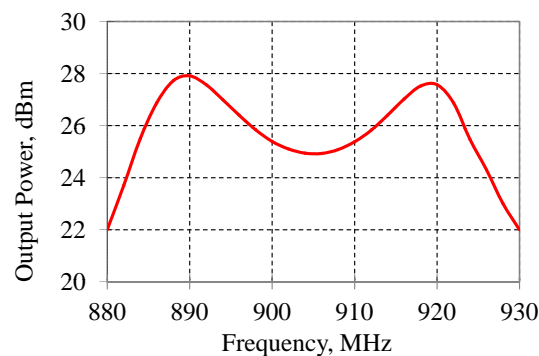


Figure 5.4.2: Typical result for the measured output power of the class-S PA with a DT reconstruction filter, operating for test purposes in a class-D regime (driven by a 50% duty cycle square wave) over the specified bandwidth around 900 MHz centre frequency.

which suffers from strongly varying data traffic. From the results obtained, it can be concluded that improvement in drain efficiency is the effect of the GaN HEMT MMICs (supplied by IAF), which have low ON-resistance.

This demonstrator was tested in a class-S operation regime in which it was driven by the $\Delta\Sigma$ -modulated one-tone signals at 900 MHz. Output power grows as drain voltage increases (the maximum, 2.4 W, is at 14 V). The maximum drain efficiency was 43% and it was found that it remains constant as drain voltage grows (Fig. 5.4.3,b) [14, 16]. In practice the system in question demonstrated even better power characteristics than in simulation, because the GaN HEMT MMICs have low ON-resistance.

C. Version 3

The last version of the demonstrator for the GSM frequency band was implemented with GaN HEMT MMICs supplied by IAF and the microstrip ST BICLF. The demonstrator was assembled by EADS Deutschland GmbH in Ulm, Germany and experimentally investigated in both class-D and class-S operation regimes at Ilmenau University of Technology, Germany.

There were two steps to the measurement procedure. The first step was filter tuning, in order to find the optimal bias points for the pre-amplifier and the final stages. The filter tuning step was concluded in a class-D regime so that

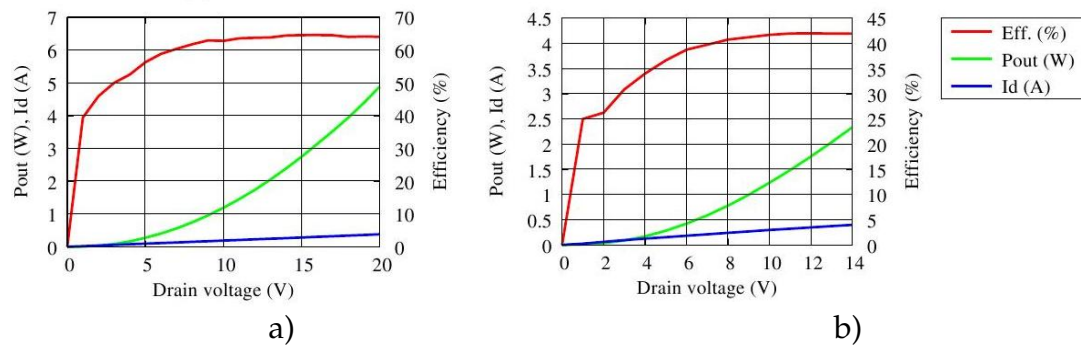


Figure 5.4.3: Typical measurement results of the class-D PA (a) and of the class-S PA (b) with a DT reconstruction filter [16]. There are output power (green curves), drain efficiency (red curves), and drain current (blue curves) as functions of the drain voltage.

the centre frequency of the RF signal was swept, and the shape of the output power curve was obtained. In order to get the constant output power in-band, it was necessary to tune the filter with the aid of both the trimmers at the ends of the first resonator and a dielectric material, which served to correct the coupling coefficient (seen in Fig. 5.3.5). The second step was to test the demonstrator in a class-D regime. The impact of the filter termination on the shape of the output power is presented in Fig. 5.4.4, where the three output characteristics correspond to the different biasing points (2 V, 7 V and 15 V). As can be seen, the filter results in the constant output power independently of the biasing conditions.

The measurement results in a class-D regime are presented in Fig. 5.4.5. The maximum output power achieved was 5 W (at drain voltage of 16 V). The maximum drain efficiency was 36%, which is only half of that in the previous version. Although the filter has relatively low insertion loss, 1 dB, this low drain efficiency may be the effect of the output circuit, which has too high an input impedance, 350 Ω , to provide the optimal power conditions for the MMICs. For the purposes of the current study this demonstrator was also tested in a class-S operation regime. The transistors were driven differentially with the BP-PLM-modulated QPSK signal at 900 MHz. The measurement results are presented in Fig. 5.4.6. In the present demonstrator, the maximum output power was 1.5 W

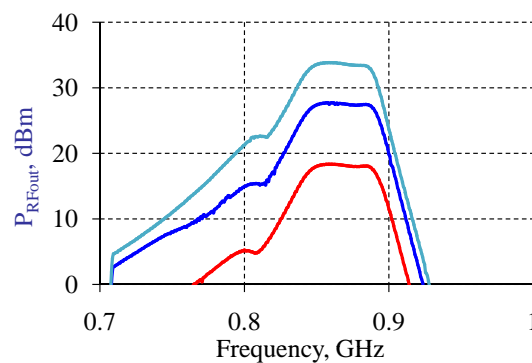


Figure 5.4.4: Typical result for the measured output power of the class-S PA with a ST reconstruction filter, operating for test purposes in a class-D regime (driven by a 50% duty cycle square wave) over the specified bandwidth around 900 MHz centre frequency: for different biasing voltages of 2 V (red curve), 7 V (blue curve) and 15 V (light blue curve).

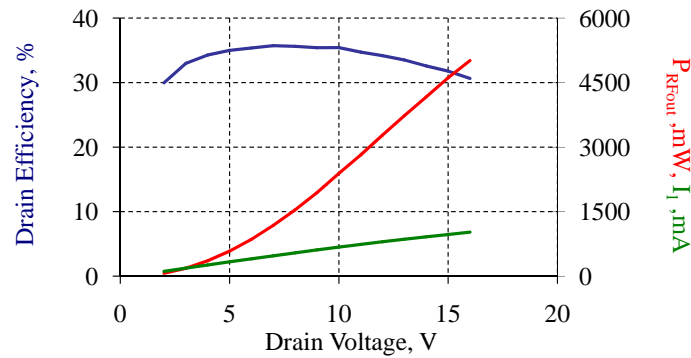


Figure 5.4.5: Measurement results of the class-S PA with a ST reconstruction filter, operating for test purposes in a class-D regime (driven by a 50% duty cycle square wave). There are output power (red curve), drain efficiency (blue curve), and drain current (green curve) as functions of the drain voltage.

at a drain voltage of 12 V. Drain efficiency reached a maximum value of 13.5% at 5 V. The measured EVM was about 13.5%, which is still below the standard limit of 17.5%. The system in question was also tested when driven by a 16-QAM-test signal: here, the measured drain efficiency was 11.5%, EVM 15.5% and ACPR -28 dB at an offset of 5 MHz. The performance figure obtained was expected because both modulator schemes have relatively low coding efficiency. It is clear that there is some room for further improvements to drain efficiency and system linearity.

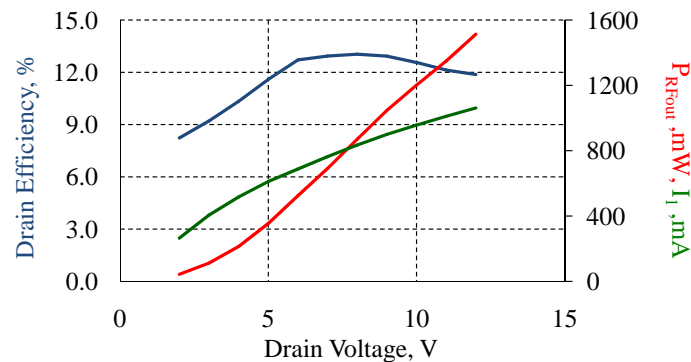


Figure 5.4.6: Measurement results of the class-S PA with a ST reconstruction filter, which is driven by a BP-PLM QPSK signal. There are output power (red curve), drain efficiency (blue curve), and drain current (green curve) as functions of the drain voltage.

5.5 Conclusion regarding implementation of switched-mode power amplifiers

This section has presented the implementation of various switched-mode power amplifiers, and a summary of the conclusions now follows.

1. In order to eliminate both the parasitic drain-source capacitance and the ON-resistance, it is necessary to improve the performance of GaN HEMTs. Their drain-source capacitance will have the effect of increasing the rise time in the drain current pulses; and their ON-resistance that of decreasing drain efficiency. Moreover, not only can the drain-source capacitance not be compensated in the reconstruction filter but, in combination with the filter, it aggravates the shape of the drain currents.
2. The one-bit modulator (especially a $\Delta\Sigma$ M) is a crucial element of a class-S PA system, whose coding efficiency needs improvement. Also, it is here shown by simulation that a $\Delta\Sigma$ M intensifies the negative effects of other elements of the PA system.
3. The parasitic capacitance to ground at the filter input has a similar effect to that of the drain-source capacitance in the transistors. This effect will be negligible if it is less than 2 pF, which corresponds to common-mode impedance of less than 40 Ω at 2 GHz. Because the filter architectures presented in this dissertation have demonstrated even better out-of-band characteristics, it can be taken that they will not significantly affect the PA performance. However, it is necessary to reduce the capacitances to ground as much as possible, because they may occur not only in a reconstruction filter, but also in the mounting board, in biasing networks, or in MMICs, which makes them a serious challenge.
4. It was experimentally found that distortion in the time signal at the drains is the cumulative effect of the biasing conditions of the final stage and of the GaN HEMT MMICs utilised. Under these conditions it is not possible

5.5 Conclusion regarding implementation of switched-mode power amplifiers

to evaluate the discrete impact of the filter characteristics out-of-band. It can, however, be found by the process of elimination on comparing the different demonstrator versions. The significant improvement in the shape of the drain signals was found by this method to be the effect of the BICLF with an electrically-short input loop, which thus clearly fulfils the requirements for the filter impedance out-of-band under the given driving conditions.

5. The impact of the filter termination on the shape of the output power was confirmed experimentally. A singly terminated filter will result in constant output power independently on biasing conditions, while doubly terminated filters will result in pronounced maxima in drain voltages, in drain efficiency, and in output power. In order to provide constant output power, it is necessary not only that the reconstruction filter be singly terminated, but also that the final stage act as an ideal current source.
6. Both the successful filter design and the GaN HEMT MMICs with low ON-resistance have meant that, to date, maximum power efficiency of 65% has been achieved in switched-mode power amplifier systems.

In the last chapter, which now follows, there will be a summary of the overall conclusions and an outlook on possible future work.

6 Conclusions

Today, because of the rapidly growing mobile communication industry and the extremely low power efficiency of the BTSs in current use, the energy efficiency has strategic priority. This work has, therefore, focused on a class-S power amplifier system with simplified transmitter architectures and increased power efficiency, which makes an attractive candidate for cellular phone BTS applications.

The class-S PA architecture and its building blocks have been considered in detail, together with the issues concerning each block and the potential influence of each block on a reconstruction output filter in particular. Besides the demands imposed by wireless BTSs in the 3G and 4G mobile telecommunication networks, there are numerous other demands on a reconstruction filter for a class-S PA system, some of which deserve special attention. Firstly, in order to shape the noise-like $\Delta\Sigma$ M spectrum or periodic parasitic harmonics in the PLM spectrum, the filter is required to have wide stop-band. Secondly, because the authors choice fell on a current-mode final stage configuration, a reconstruction filter is required with a balanced input. This balanced input can be excited either by differential mode or by common mode. In order to sustain the rectangular shape of the drain current, and, with it, high drain efficiency, the reconstruction filter should have low-ohmic input impedance for the differential mode and high-ohmic for the common mode. Thirdly, because the final stage of CMCS PAs acts like a current source with infinite internal impedance, a singly terminated (ST) filter is required. Only the ST filter can have a constant in-band input resistance and, consequently, enable the whole system to provide constant output power in-band. Under the same driving conditions a doubly terminated (DT) filter will have pronounced maxima in its input resistance, which can re-

sult in high drain voltages, potentially damaging the switching transistors. Finally, for the GaN HEMTs to have optimal power conditions, it is necessary for a reconstruction filter to have optimal input impedance in-band, transforming it to antenna impedance. Here, an ST filter with impedance transformation is required. A proposed novel approach for these filters has been vindicated by simulation in ADS.

The main focus of the research has been on the design of the reconstruction filter, with the finding that the electrical and geometrical constraints for the reconstruction filter can be satisfied by a mechanically-tunable high-power coaxial CLF which then serves as a basis for the further filter design. This study has presented several alternative architectures of a balanced input comb-line filter, all of which successfully combine the properties of a balun and a comb-line filter, and are compatible with the $\Delta\Sigma$ -modulated signals. One of the architecture, a BICLF with a straight loop, will succeed in fulfilling all the requirements for a CMCS PA system, given galvanic isolation of the filter housing from the common ground. In case it is necessary to obviate galvanic isolation, next architecture has been developed, a BICLF with a PSN. Yet another architecture, the BICLF with an electrically-short input loop will have advantages over the first two in that the floating electrically-short input loop provides short-circuiting of the drain currents in DC, and does not involve any periodicity out-of-band. The analysis of the reconstruction filter is completed by a presentation of simulation and measurement of a CMCS PA system and a CMCD PA system, in both of which the filter architectures proposed are employed. In this analysis it has been found that there are certain demands imposed on elements of the system when the reconstruction filter is the particular object of consideration. The first of those demands is that, in order to eliminate both the parasitic drain-source capacitance and the ON-resistance, it is necessary to improve the performance of GaN HEMTs. The drain-source capacitance will have the effect of increasing the rise time in the drain current pulses; and the ON-resistance of decreasing drain efficiency. This drain-source capacitance cannot be compensated for in the reconstruction filter and in combination with the filter it has a deleterious effect

on the shape of the drain currents. Secondly, the $\Delta\Sigma\text{M}$, being the most critical element of the class-S PA system, requires modification to improve its coding efficiency. Also, the $\Delta\Sigma\text{M}$ will intensify the negative effects of other elements of the PA system. In a system with the present GaN HEMTs, this modulator will considerably decrease drain efficiency, and, at the same time, the impact of the insertion loss in the filter will be reinforced. Thirdly, the impact of the filter termination on the shape of the output power has been confirmed experimentally. The singly terminated filter will result in the constant output power independently of biasing conditions, while the doubly terminated filters will result in pronounced maxima in drain voltages, in drain efficiency, and in output power. In order to provide constant output power, it is necessary not only that the reconstruction filter be singly terminated, but also that the final stage act as an ideal current source. The last of the demands comes from experimental finding that distortion in the time signal at the drains is the cumulative effect of the biasing conditions of the final stage and of the GaN HEMT MMICs utilised. Under these conditions it is not possible to evaluate the discrete impact of the filter characteristics out-of-band. This has to be found by comparing the different demonstrator versions. The significant improvement in the shape of the drain voltages is thus found to be the effect of the BICLF with an electrically short input loop, which thus clearly fulfils the requirements for the filter impedance out-of-band under the given driving conditions. Both the successful filter design and the GaN HEMT MMICs with a low ON-resistance mean that, to date, maximum power efficiency of 65% has been achieved in the switched-mode power amplifier systems.

This thesis has presented a complete analysis of reconstruction filters for current mode class-S power amplifier systems performed, as far as the author knows, for the first time. It reveals that future design of a class-S PA system must concentrate not only on optimising separate system blocks, but also on optimising complete system performance. Future work would be to design a singly terminated BICLF with an electrically short input loop and test it in a complete class-S PA system. A ferromagnetically-tunable CLF may also attract

interest for future scientific research. The architecture presented may serve as a basis for high-power RF power combiners, and is of potential value in a class-S PA system driven by a number modulators, each operating with its own RF signal.

Publications

1. E. Serebryakova, K. Blau, M. Hein. Mechanically tunable comb-line filters for switched-mode power amplifier systems. In *Proc. International Student Seminar on Microwave and Optical Applications of Novel Physical Phenomena*, pages 61–63, 2008.
2. E. Serebryakova, K. Blau, M. Hein. Miniaturisation of combline filters for switched-mode power amplifier systems. *Advances in Radio Science*, Vol. 6: pages 125–127, 2008, DOI: 10.5194/ars-6-125-2008.
3. E. Serebryakova, A. Samulak, K. Blau, M. Hein. Reconstruction filters for switched-mode power amplifier systems. In *Proc. European Microwave Conference*, pages 1453 – 1456, 2009, ISBN: 978-1-4244-4748-0.
4. A. Samulak, E. Serebryakova, G. Fischer, and R. Weigel. Modulation and filter test procedure for RF class-S power amplifier architecture. In *Proc. Asia-Pacific Microwave Conference*, pages 1104 – 1107, 2009, DOI: 10.1109/APMC.2009.5384386.
5. E. Serebryakova , J. Trabert , K. Blau and M. Hein. High-power filters for switched-mode power amplifier systems. In *Proc. IEEE Radio and Wireless Symposium*, pages 276–279, 2009, DOI: 10.1109/RWS.2009.4957332.
6. E. Serebryakova, K. Blau, M. Hein. Compact low-loss wideband-matched RF filters for class-S power amplifier systems. In *Proc. German Microwave Conference*, pages 198–201, 2010, ISBN: 978-1-4244-4933-0.
7. K. Blau, E. Serebryakova, M. Hein. Bandpass filter mit elektromagnetisch verkoppelten Resonatoren, 2010. German Patent DE102008053013A1.

8. E. Serebryakova, K. Blau, M.A. Hein. Singly and doubly terminated balanced input comb-line filters for current-mode class-S power amplifiers. In *Proc. International Conference on Telecommunications in Modern Satellite, Cable and Broadcasting Services, TELSIKS*, pages 230–233, 2011, DOI: 10.1109/TELSKS.2011.6112040.
9. E. Serebryakova, K. Blau, M.A. Hein. Singly terminated reconstruction filters for current-mode class-S power amplifiers. In *IEEE MTT-S International Microwave Symposium Digest*, pages 1–4, 2011, DOI: 10.1109/MWSYM.2011.5972705.

Bibliography

- [1] Mobile-GaN research program,
<http://www.pt-it.pt-dlr.de/de/1760.php>.
- [2] T. Miki, T. Ohya, H. Yoshino, N. Umeda. The overview of the 4th generation mobile communication system. *Proc. International Conference on Information, Communications and Signal Processing*, pages 1600 – 1604, 2005, DOI: 10.1109/ICICS.2005.1689329.
- [3] A. Samulak. *System analysis of class-S power amplifier*. PhD thesis, University of Erlangen-Nuremberg, 2009.
- [4] P. Ostrovskyy, H. Gustat , C. Scheytt and Y. Manoli. A 9 GS/s 2.1..2.2 GHz bandpass delta-sigma modulator for Class-S power amplifier. In *Proc. IEEE MTT-S International Microwave Symposium*, pages 1129–1132, 2009, DOI: 10.1109/MWSYM.2009.5165900.
- [5] Ch. Hartmann. Vergleich zwischen Pulslaengen-Modulator und Bandpass-Delta-Sigma-Modulator zur AD-Wandlung von Hochfrequenz-Signalen. Master's thesis, Technische Universitaet Ilmenau, 2005.
- [6] Third Generation Partnership Project, Technical Specification Group Radio Access Network, Universal Mobile Telecommunications System (UMTS); Base Station (BS) Radio Transmission and Reception (FDD), 3GPP TS 25.104, V8.6.0, Rel. 8, Mar. 2009, [Online]. Available: <http://www.3gpp.org>.

- [7] W. Eisenstadt, B. Stengel, and B.M. Thompson. *Microwave differential circuit design using mixed-mode S-Parameters*. Artech House Inc., 2006, ISBN: 1-580-53933-5.
- [8] J.L. Herrero and G. Willoner. *Synthesis of filters*. Prentice Hall, 1966, ISBN: 0138800057.
- [9] M. Hoeft. Dielectric TE dual-mode resonator filters. In *Proc. German Microwave Conference*, pages 206–209, 2010, ISBN: 978-1-4244-4933-0.
- [10] G. Shaik, G. Fischer, J. Detlefsen. Metamaterial based RF Tx-bandpass filter design for EGSM-900 base stations. In *IEEE National workshop on Metamaterials and special materials for electromagnetic applications and TLC*, pages 291–296, 2008.
- [11] S. Geelani. *High Q-factor Metamaterial Duplex Filters in Suspended Stripline Technology*. PhD thesis, University of Erlangen-Nuernberg, 2009.
- [12] G.L. Matthaei, E. L. Jones, L. Young. *Microwave filters, impedance-matching networks, and coupling structures*. Artech House Books., 1985, ISBN: 0-89006-099-1.
- [13] C. Meliani et al. Switch-mode amplifier ICs with over 90% efficiency for Class-S PAs using GaAs-HBTs and GaN-HEMTs. In *IEEE MTT-S International Microwave Symposium Digest*, pages 751–754, 2008, DOI: 10.1109/MWSYM.2008.4632941.
- [14] M. Oppermann et al. GaMoKOM - GaN-Module fuer Kommunikation-sapplikationen. Teilvorhaben. Projekt-Endbericht. Foerderschwerpunkt - mobileGaN. Technical report, European Aeronautic Defence and Space Company Deutschland, 2010.
- [15] O. Ambacher et al. Energieeffizienz linearer Leistungsverstaerker fuer Basisstationsanwendungen: ELBA; Abschlussbericht; Teilvorhaben: ELBATEC: GaN-Epitaxie und -Technologieentwicklung fuer zuverlaessige, energieeffiziente Basisstationsanwendungen. Technical report,

Fraunhofer-Gesellschaft Institut fuer Angewandte Festkoerperphysik (IAF), 2010.

- [16] U. Schmid, R. Reber, S. Chartier, W. Grabherr, R. Leberer, M. Oppermann. Advances on GaN based switch mode amplifiers for communication applications. In *Proc. European Microwave Conference*, pages 163–166, 2011, Print ISBN: 978-1-61284-235-6.
- [17] U. Schmid et al. GaN devices for communication applications: evolution of amplifier architectures. *International Journal of Microwave and Wireless Technologies*, Vol. 2, Issue 1: pages 85–93, 2010, DOI: 10.1017/S1759078710000218.
- [18] M. Haas-Zens, C. Hartmann, K. Blau, M.A. Hein. An integrated SiGe HBT bandpass-pulse length modulator for switch mode power amplifiers in the SHF range. In *Proc. International Conference on Microwave Radar and Wireless Communications*, pages 1–5, 2010, ISBN: 978-1-4244-5288-0.
- [19] GSM, www.gsmworld.com, 2011.
- [20] Technical specification, Universal Mobile Telecommunications System (UMTS); Base Station (BS) radio transmission and reception (FDD), 3GPP TS 25.104 version 8.6.0 Release 8, ETSI TS 125 104 V8.6.0 (2009-03).
- [21] 3GPP Wireless Technologies Pass 5 Billion Global Connections. Technical report, 4G Americas, 2011.
- [22] Mobile Broadband Explosion: 3GPP Broadband Evolution to IMT-Advanced. Technical report, Rysavy Research/4G Americas, Sep. 2011.
- [23] A. Birafane, M. El-Asmar, A.B. Kouki, M. Helaoui, F.M. Ghannouchi. Analyzing LINC systems. *IEEE Microwave Magazine*, Vol. 11, Issue 5: pages 59 – 71, 2010, DOI: 10.1109/MMM.2010.935774.
- [24] 49 Commercial LTE Networks Confirmed by GSA, www.gsacom.com, January 2012.

- [25] O. Blume, D. Zeller, U. Barth. Approaches to energy efficient wireless access networks. In *Proc. International Symposium on Communications, Control and Signal Processing, ISCCSP*, pages 1–5, 2010, DOI: 10.1109/ISCCSP.2010.5463328.
- [26] Mobile’s Green Manifesto. Technical report, GSM World in collaboration with the Climate Group and Irbaris, 2009.
- [27] Climate change: Commission welcomes final adoption of Europe’s climate and energy package. Technical report, EC press release Dec. 2008.
- [28] Green Touch Initiative, <http://www.greentouch.org>.
- [29] G. Schmitt. The green base station. In *Proc. International Telecommunication Energy Special Conference*, pages 1–6, 2009, ISBN: 978-3-8007-3162-6.
- [30] Ch. Hartmann, K. Blau, M.A. Hein. An integrated SiGe HBT pulselength modulator for class-S power amplifiers in the UHF range. *IEEE Transactions on Circuits and Systems-I: Analog and Digital Signal Processing*, Vol. 58, Issue 1: pages 62–69, 2009, DOI: 10.1109/TCSI.2010.2071510.
- [31] S. Maroldt et al. High efficiency digital GaN MMIC power amplifiers for future switch-mode based mobile communication systems. In *Proc. IEEE Compound Semiconductor Integrated Circuit Symposium, CISC*, pages 1–4, 2009, DOI: 10.1109/csics.2009.5315720.
- [32] A. Grebennikov, N.O. Sokal. *Switchmode RF Power Amplifiers*. Elsevier Science & Technology Books, 2007, ISBN: 978-0-7506-7962-6.
- [33] S.C. Cripps. *RF Power Amplifiers for Wireless Communications*. Norwood, MA: Artech House, 2006, ISBN: 1-596-93018-7.
- [34] B. Kim, I. Kim, J. Moon. Advanced Doherty architecture. *IEEE Microwave Magazine*, Vol. 11, Issue 5: pages 72 – 86, 2010, DOI: 10.1109/MMM.2010.937098.

- [35] F.H. Raab et al. RF and microwave power amplifier and transmitter technologies – part 2. *High Frequency Electronics*, pages 22–36, 2003.
- [36] K. Kang et al. Class-D audio amplifier using 1-bit fourth-order delta-sigma modulation. *IEEE Transactions on Circuits and Systems-II*, Vol. 55, Issue 8: pages 728–732, 2008, DOI: 10.1109/TCSII.2008.922457.
- [37] J. Varona, A.A. Hamoui, K. Martin. A low-voltage fully-monolithic $\Delta\Sigma$ -based class-D audio amplifier. In *Proc. European Solid-State Circuits Conference*, pages 545–548, 2003, DOI: 10.1109/ESSCIRC.2003.1257193.
- [38] F.A. Himmelstoss and K.H. Edelmoser. High dynamic class-D power amplifier. *IEEE Transactions on Consumer Electronic*, Vol. 44, Issue 4: pages 1329 – 1333, 1998, DOI: 10.1109/30.735834.
- [39] Texas Instruments. <http://www.ti.com/>.
- [40] M. Iwamoto et al. Bandpass delta-sigma class-S amplifier. *Electronics Letters*, Vol. 36, Issue 12: pages 1010 – 1012, 2000, DOI: 10.1049/el:20000794.
- [41] M. Iwamoto, J. Hinrichs, J. Arun, L.E. Larson, and P.M. Asbeck. A push-pull bandpass $\Delta - \Sigma$ class-S amplifier. In *IEEE Topical Workshop on Power Amplifiers for Wireless Communications, San Diego, CA*, 2000.
- [42] A. Jayaraman, P.F. Chen, G. Hanington, L. Larson and P. Asbeck. Linear high-efficiency microwave power amplifiers using bandpass delta-sigma modulators. *IEEE Microwave and Guided Wave Letters*, Vol. 8, Issue 3: pages 121 – 123, 1998, DOI: 10.1109/75.661135.
- [43] J. Keyzer, J. Hinrichs, A. Metzger, M. Iwamoto, I. Galton, P.M. Asbeck. Digital generation of RF signals for wireless communications with bandpass delta-sigma modulation. In *Proc. IEEE MTT-S International Microwave Symposium*, pages 2127–2130, 2001, DOI: 10.1109/MWSYM.2001.967334.

- [44] T. Johnson, S. Stapleton. Available load power in a RF class D amplifier with a sigma-delta modulator driver. In *Proc. IEEE Radio and Wireless Conference*, pages 439 – 442, 2004, DOI: 10.1109/RAWCON.2004.1389171.
- [45] T. Johnson, S. Stapleton. RF class-D amplification with bandpass sigma delta modulator drive signals. *IEEE Transactions Circuits Systems*, Vol. 53, Issue 12: pages 2507 – 2520, 2006, DOI: 10.1109/TCSI.2006.885980.
- [46] T. Johnson, R. Sobot, S. Stapleton. Measurement of bandpass sigma-delta modulator coding efficiency and pulse transition frequency for RF class d power amplifier applications. In *Proc. Canadian Conference on Electrical and Computer Engineering, CCECE*, pages 2314 – 2317, 2006, DOI: 10.1109/CCECE.2006.277768.
- [47] T. Johnson, R. Sobot, S. Stapleton. CMOS RF class-D power amplifier with band-pass sigma-delta modulation. *Microelectronics Journal*, Vol. 38, Issue 3: pages 439–446, 2007, DOI: 10.1016/j.mejo.2007.01.009.
- [48] T. Johnson, S. Stapleton. Comparison of bandpass formula delta sigma modulator coding efficiency with a periodic signal model. *IEEE Transactions on Circuits and Systems*, Vol. 55, Issue 11: pages 3763–3775, 2008, DOI: 10.1109/TCSI.2008.927219.
- [49] S. Ralph, and R. Farrell. Using high pass sigma-delta modulation for class-S power amplifiers. In *Proc. European Conference on Circuit Theory and Design, ECCTD*, pages 707–710, 2007, DOI: 10.1109/ECCTD.2007.4529694.
- [50] J. Dooley , T. Podsiadlik , A. Canniff , and R. Farrell. Reconfigurable Class-S power amplifiers at RF and microwave frequencies. In *Proc. Workshop on Integrated Nonlinear Microwave and Millimetre-Wave Circuits*, pages 43–46, 2008, DOI: 10.1109/INMMIC.2008.4745710.
- [51] J. Dooley and R. Farrell . A practical class-S power amplifier for high frequency transmitters. In *Proc. Colloquium on Wireless Communications*, 2008, ID Code:1409.

- [52] T. Podsiadlik, J. Dooley, A. Canniff, R. Farrell. Pulse width modulation of multilevel delta-sigma output for class-S power amplifier. In *Proc. European Conference on Circuit Theory and Design*, pages 457–460, 2009, DOI: 10.1109/ECCTD.2009.5275017.
- [53] J. Dooley, G. Corley, T. Podsiadlik, R. Farrell. Reconfigurable high frequency class S power amplifier demonstrator. In *Proc. Workshop on Integrated Nonlinear Microwave and Millimetre-Wave Circuits, INMMIC*, pages 1–4, 2011, DOI: 10.1109/INMMIC.2011.5773308.
- [54] S.A. El-Hamamsy. Design of high-efficiency RF class-D power amplifier. *IEEE Transaction on Power Electronics*, Vol. 9, Issue 3: pages 297 – 308, 1994, DOI: 10.1109/63.311263.
- [55] T.P. Hung, A.G. Metzger, P.J. Zampardi, M. Iwamoto, and P.M. Asbeck. Design of high-efficiency current-mode class-D amplifiers for wireless handsets. *IEEE Transactions on Microwave Theory and Techniques*, Vol. 53, Issue 1: pages 144 – 151, 2005, DOI: 10.1109/TMTT.2004.839327.
- [56] J. Sommarek, A. Virtanen, J. Vankka, K. Halonen. Comparison of different class-D power amplifier topologies for 1-bit band-pass delta-sigma D/A converters. In *Proc. Norchip Conference*, pages 115–118, 2004, DOI: 10.1109/NORCHP.2004.1423836.
- [57] T.P. Hung, J. Rode, L.E. Larson, and P.M. Asbeck. Design of H-Bridge class-D power amplifiers for digital pulse modulation transmitters. *IEEE Transactions on Microwave Theory and Techniques*, Vol. 55, Issue 12: pages 2845 – 2855, 2007, DOI: 10.1109/TMTT.2007.909881.
- [58] A. Wentzel et al. Design and realization of an output network for a GaN-HEMT current-mode class-S power amplifier at 450MHz. In *Proc. German Microwave Conference*, pages 1–4, 2009, DOI: 10.1109/GEMIC.2009.4815892.

- [59] A. Wentzel, F. Schnieder, C. Meliani, W. Heinrich. A simplified switch-based GaN HEMT model for RF switch-mode amplifiers. In *Proc. European Microwave Integrated Circuits Conference*, pages 77–80, 2009, ISBN: 978-1-4244-4749-7.
- [60] A. Wentzel, C. Meliani, W. Heinrich. RF class-S power amplifiers: State-of-the-art results and potential. In *IEEE MTT-S International Microwave Symposium Digest*, pages 812–815, 2010, DOI: 10.1109/MWSYM.2010.5517402.
- [61] W. Heinrich, A. Wentzel, and C. Meliani. Advanced switch-mode concepts using GaN: The class-S amplifier. In *Proc. International Conference on Microwave Radar and Wireless Communications, MIKON*, pages 1–6, 2010, ISBN: 978-1-4244-5288-0.
- [62] A. Wentzel, C. Meliani, W. Heinrich. A voltage-mode class-S power amplifier for the 450 MHz band. In *Proc. European Microwave Conference*, pages 640 – 643, 2010, ISBN: 978-1-4244-7232-1.
- [63] A. Wentzel, C. Meliani, W. Heinrich. Optimized coding scheme for class-S amplifiers. In *Proc. European Microwave Conference*, pages 329–332, 2011, Print ISBN: 978-1-61284-235-6.
- [64] A. Wentzel. *Klasse-S Mikrowellen-Leistungsverstaerker mit GaN-Transistoren*. PhD thesis, Technische Universitaet Berlin, 2011.
- [65] A. Samulak , G. Fischer and R. Weigel. Demonstrator of class-S power amplifier for base stations based on GaN technology. In *Proc. International Conference on Microwaves, Radar and Wireless Communications, MIKON*, pages 1–4, 2008, ISBN: 978-83-906662-8-0.
- [66] A. Samulak, G. Fischer, R. Weigel. Demonstrator of class-S power amplifier based on GaN transistors. In *Proc. German Microwave Conference*, pages 1–4, 2008, ISBN: 978-3-8007-3086-5.

- [67] A. Samulak, G. Fischer and R. Weigel. Basic nonlinear analysis of class-S power amplifiers based on GaN switching transistors. In *Proc. German Microwave Conference*, pages 1–4, 2009, DOI: 10.1109/GEMIC.2009.4815900.
- [68] A. Samulak, G. Fischer and R. Weigel. Optimized delta sigma modulation for class-S power amplifiers based on GaN switching transistors. In *Proc. IEEE Radio and Wireless Symposium*, pages 546–549, 2009, DOI: 10.1109/RWS.2009.4957409.
- [69] A. Samulak, E. Serebryakova, G. Fischer, and R. Weigel. Modulation and filter test procedure for RF class-S power amplifier architecture. In *Proc. Asia-Pacific Microwave Conference*, pages 1104 – 1107, 2009, DOI: 10.1109/APMC.2009.5384386.
- [70] R. Leberer, R. Reber, and M. Oppermann. An AlGaIn/GaN class-S amplifier for RF-communication signals. In *Proc. IEEE MTT-S International Microwave Symposium*, pages 85–88, 2008, DOI: 10.1109/MWSYM.2008.4633109.
- [71] D. Wiegner et al. Energieeffizienz linearer Leistungsverstaerker fuer Basisstationsanwendungen: Berichtszeitraum: 01.08.2006 - 31.07.2009; Abschlussbericht . Technical report, Alcatel-Lucent Deutschland AG, 2010.
- [72] F. Raab. Radio frequency pulsewidth modulation. *IEEE Transactions on Communications*, Vol. 21, Issue 8: pages 958 –966, 1973, DOI: 10.1109/TCOM.1973.1091763.
- [73] M. Nielsen, T. Larsen. A 2-GHz GaAs HBT RF pulsewidth modulator. *IEEE Transactions on Microwave Theory and Techniques*, Vol. 56, Issue 2: pages 300 – 304, 2008, DOI: 10.1109/TMTT.2007.913375.
- [74] E.A. Guillemin. *Synthesis of passive networks*. Willey, 1957.
- [75] C. Canuto, A. Tabacco, A. M. Tabacco Vignati. *Mathematical Analysis II*. Springer-Verlag Italia, Milano, 2010, ISBN: 978-88-470-1783-2.

- [76] E. Serebryakova, K. Blau, M.A. Hein. Singly terminated reconstruction filters for current-mode class-S power amplifiers. In *IEEE MTT-S International Microwave Symposium Digest*, pages 1–4, 2011, DOI: 10.1109/MWSYM.2011.5972705.
- [77] Inc. Coilcraft. <http://www.coilcraft.com/>.
- [78] Kendall L. Su. *Analog Filters*. Chapman & Hall, 1996, ISBN: 0-412-63840-1.
- [79] G.L. Matthaei. Tables of Chebyshev impedance-transforming networks of low-pass filter form. In *Proc. of the IEEE*, pages 939–963, 1964, DOI: 10.1109/PROC.1964.3185.
- [80] E.G. Cristal. Tables of maximally flat impedance-transforming networks of low-pass-filter form. *IEEE Transaction on Microwave Theory and Techniques*, Vol. 13, Issue 3: pages 693–695, 1965, DOI: 10.1109/TMTT.1965.1126064.
- [81] E.G. Cristal, G.L. Matthaei. A technique for the design of multiplexers having contiguous channels. *IEEE Transactions on Microwave Theory and Techniques*, Vol. 12, Issue 1: pages 88 – 93, 1964, DOI: 10.1109/TMTT.1964.1125756.
- [82] L. Weinberg. Additional tables for design of optimum ladder networks. *Journal of the Franklin Institute*, Vol. 264, Issue 1: pages 7–23, 1957, DOI: 10.1016/0016-0032(57)90843-8.
- [83] R.R. Mansour. Filter technologies for wireless base stations. *IEEE Microwave Magazine*, Vol. 5: pages 68 – 74, 2004, DOI: 10.1109/MMW.2004.1284945.
- [84] M. Memarian and R.R. Mansour. Dual-mode half-cut dielectric resonator filters. In *Proc. IEEE MTT-S International Microwave Symposium*, pages 1465–1468, 2009, DOI: 10.1109/MWSYM.2009.5165984.

- [85] V.G. Veselago. The electrodynamics of substances with simultaneously negative values of ϵ and μ . *Sov. Phys.-Usp.*, Vol. 10: pages 509–514, 1968.
- [86] M.S. Heutmaker. The error vector and power amplifier distortion. In *Proc. Wireless Communications Conference*, pages 100–104, 1997, DOI: 10.1109/WCC.1997.622256.
- [87] R. Levy, H.-W. Yao, K.A. Zaki. Transitional combline/evanescent-mode microwave filters. *IEEE Transactions on Microwave Theory and Techniques*, Vol.45, Issue 12: pages 2094–2099, 1997, DOI: 10.1109/22.643743.
- [88] R. Levy, R.V. Snyder, G. Matthaei. Design of microwave filters. *IEEE Transactions on Microwave Theory and Techniques*, Vol.50, Issue 3: pages 783 – 793, 2002, DOI: 10.1109/22.989962.
- [89] J.L. Altman. *Microwave circuits*. D.Van Nostrand company Inc., 1964.
- [90] R.M. Kurzrok. Design of comb-line bandpass filters. *IEEE Transactions on Microwave Theory and Techniques*, Vol. 14: pages 351–353, 1966, DOI: 10.1109/TMTT.1966.1126269.
- [91] S.B. Cohn. Dissipation loss in multiple-coupled resonators filters. *Proc. of the Institute of Radio Engineers*, Vol. 47, Issue 8: pages 1342 – 1348, 1959, DOI: 10.1109/JRPROC.1959.287201.
- [92] E. Serebryakova, K. Blau, M. Hein. Miniaturisation of combline filters for switched-mode power amplifier systems. *Advances in Radio Science*, Vol. 6: pages 125–127, 2008, DOI: 10.5194/ars-6-125-2008.
- [93] J. Uher, W.J.R. Hofer. Tunable microwave and millimeter-wave bandpass filters. *IEEE Transactions on Microwave Theory and Techniques*, Vol. 39, Issue 4: pages 643 –653, 1991, DOI: 10.1109/22.76427.
- [94] E. Serebryakova, K. Blau, M. Hein. Mechanically tunable comb-line filters for switched-mode power amplifier systems. In *Proc. International Student*

Seminar on Microwave and Optical Applications of Novel Physical Phenomena, 2008.

- [95] S.B. Cohn. Rounded corners in microwave high-power filters and other components. *IRE Transactions on microwave theory and techniques*, Vol. 9 , Issue 5: pages 389–397, 1961, DOI: 10.1109/TMTT.1961.1125359.
- [96] J.H. Vogelman. High-power microwave filters. *IRE Transactions on Microwave Theory and Techniques*, Vol. 6 , Issue: 4: pages 429–439, 1958, DOI: 10.1109/TMTT.1958.1125220.
- [97] J.R. Whinnery , H.W. Jamieson , T.E. Robbins. Coaxial-line discontinuities. In *Proc. Institute of Radio Engineers, IRE*, pages 695 – 709, 1944, DOI: 10.1109/JRPROC.1944.234027.
- [98] E. Serebryakova , J. Trabert , K. Blau and M. Hein. High-power filters for switched-mode power amplifier systems. In *Proc. IEEE Radio and Wireless Symposium*, pages 276–279, 2009, DOI: 10.1109/RWS.2009.4957332.
- [99] W. Renbin, C. Mmasi, V. Govind, S. Dalmia, C. Ghiu, G. White. High performance and compact balanced-filter design for WiMAX front-end modules (FEM) using LCP-based organic substrates. In *Proc. IEEE/MTT-S International Microwave Symposium*, pages 1619 – 1622, 2007, DOI: 10.1109/MWSYM.2007.379996.
- [100] M.C. Park, B.H. Lee, and D.S. Park. A laminated balance filter using LTCC technology. In *Proc. Asia-Pacific Microwave Conference*, pages 1–4, 2005, DOI: 10.1109/APMC.2005.1606973.
- [101] D.-W. Yoo, E.-S. Kim, S.-W. Kim. A balance filter with DC supply for Bluetooth module. In *Proc. European Microwave Conference*, 2005, DOI: 10.1109/EUMC.2005.1610158.
- [102] J. Shi, Q. Xue. Balanced bandpass filters using center-loaded half-wavelength resonators. *IEEE Transactions on Microwave The-*

ory and Techniques, Vol. 58, Issue 4: pages 970 – 977, 2010, DOI: 10.1109/TMTT.2010.2042839.

- [103] E. Serebryakova, A. Samulak, K. Blau, M. Hein. Reconstruction filters for switched-mode power amplifier systems. In *Proc. European Microwave Conference*, pages 1453 – 1456, 2009, ISBN: 978-1-4244-4748-0.
- [104] E. Serebryakova, K. Blau, M. Hein. Compact low-loss wideband-matched RF filters for class-S power amplifier systems. In *Proc. German Microwave Conference*, pages 198–201, 2010, ISBN: 978-1-4244-4933-0.
- [105] E. Serebryakova, K. Blau, M.A. Hein. Singly and doubly terminated balanced input comb-line filters for current-mode class-S power amplifiers. In *Proc. International Conference on Telecommunications in Modern Satellite, Cable and Broadcasting Services*, pages 230–233, 2011, DOI: 10.1109/TEL-SKS.2011.6112040.
- [106] W. Lifa, Y. Ruixia, and W. Jingfeng. A compact LTCC balun for Bluetooth/WLAN application. In *Proc. International Conference on Wireless Communications Networking and Mobile Computing, WiCOM*, pages 1–3, 2010, DOI: 10.1109/WICOM.2010.5601253.
- [107] S. Sakhnenko et al. LTCC balanced filter based on a transformer type balun for WLAN 802.11a application. In *Proc. European Microwave Conference*, pages 434–437, 2007, DOI: 10.1109/EUMC.2007.4405220.
- [108] K. Blau, E. Serebryakova, M. Hein. Bandpass Filter mit elektromagnetisch verkoppelten Resonatoren, 2010. German Patent DE102008053013A1.
- [109] A.C. Guyette. Alternative architectures for narrowband varactor-tuned bandpass filters. In *Proc. European Microwave Conference*, pages 475–478, 2009, ISBN: 978-1-4244-4749-7.
- [110] H.L. Lee, D. Kim, W.G. Lim, M.Q. Lee, and J.W. Yu. Miniaturized lumped-distributed wideband balun using double-sided cpw structure. In *Proc.*

European Microwave Conference, pages 1171–1174, 2009, ISBN: 978-1-4244-4748-0.

- [111] Agilent Technologies. *Guide to Harmonic Balance Simulation in ADS*, September 2004.
- [112] Agilent Technologies. *Transient and Convolution Simulation*, September 2004.
- [113] I. Khalil, E. Bahat-Treidel, F. Schnieder, and J. Wuerfl. Improving the linearity of GaN HEMTs by optimizing epitaxial structure. *IEEE Transactions on Electron Devices*, Vol. 56, Issue 3: pages 361–364, 2009, DOI: 10.1109/TED.2008.2011849.
- [114] H. Kobayashi, J.M. Hinrichs, and P.M. Asbeck. Current-mode class-D power amplifiers for high efficiency RF application. *IEEE Transactions on Microwave Theory and Techniques*, Vol. 49: pages 2480–2485, 2001, DOI: 10.1109/22.971639.
- [115] T. Cohrs. Entwurf, Aufbau und experimentelle Bewertung eines Schaltverstaerkers nach dem EER – Verfahren. Master’s thesis, Technische Universitaet Ilmenau, 2008.

List of Symbols and Acronyms

Symbols

Γ	Reflection coefficient
$\gamma(\omega)$	Complex propagation constant
$\tan(\delta)$	Loss tangent of the dielectric
Δf	3-dB bandwidth
Δf_{SH}	Offset from a centre frequency
ϵ	Ripple factor
ϵ_r	Dielectric permittivity
η_D	Drain efficiency
$\eta_{D_{VMCD}}$	Drain efficiency of a VMCD PA
$\eta_{D_{CMCD}}$	Drain efficiency of a VMCD PA
η_{pA}	Peak amplitude coding efficiency
$\eta_{pA_{class-D}}$	Peak amplitude coding efficiency of a 50% duty cycle square wave
η_P	Coding efficiency
$\eta_{P_{sinus}}$	Coding efficiency for a single-tone modulated signal
$\eta_{P_{class-D}}$	Coding efficiency of a 50% duty cycle square wave
θ	Electrical length
θ_0	Electrical length at the centre frequency
τ_0	Fixed phase offset of the signal before filtering
ϕ_0	Fixed delay value
κ	Constant for any given type of cavities resonator of the order 1500 .. 3600
λ	Wavelength

λ_0	Wavelength at the centre frequency
$\chi(Z_{EC})$	Parametrical coefficient
b	Linear dimension of a filter cavity
c_f	Crest factor
C_g	Parasitic capacitance to ground
C_{SH}	Shunt capacitance at the filter input
D	Outer diameter of coaxial line
d	Inner diameter of coaxial line
$d_n(\omega t)$	Normalised two-level modulated signal
$E(P)$	Even part of cumulant
E_g	Electromotive force of a generator
e_i	Node potential
\hat{E}_{air}	Peak electric field strength in air
$\hat{E}_{sim-air}$	Peak of electrical field strength in the filter
$F(P)$	Characteristic transfer function
f_0	Centre frequency
f_{max}	Oscillation frequency
f_T	Transit frequency
f_{SPB}	Second pass-band
g_0''	Finite g-parameter for a ST filter
g_{12}	Voltage gain
I_0	Electrical current through RF chokes
$i_{1,2}(t)$	Drain-source current
$I_{1,2}$	Amplitude of the drain-source current
I_{dmax}	Maximum available drain-source current
I_g	Amplitude of a generator current
i_i	Node current
$i_l(t)$	Load current
I_l	Amplitude of the load current
K	Coefficient taking into account the power transfer between generator and load

l	Physical length of a resonator
L_0	Insertion loss
L_{Ar}	Maximum attenuation in pass-band
N	Filter order
$O(P)$	Odd part of cumulant
p	Complex frequency
P	Normalised complex frequency
P_{aver}	Normalised average power
P_{DCt}	DC power
$P_{RF_{in}}$	Input power
$\hat{P}_{RF_{in}}$	Maximum input power
$P_{RF_{out}}$	Output power
Q	Quality factor
$QS(\theta)$	Normalized factor considering unloaded quality factor and stop-band of a CLF
Q_{UL}	Unloaded quality factor
Q_{UL-eff}	Unloaded Q-factor of the shortened resonator
r	Impedance transformation ratio
R_C	Parasitic conducting resistor in transistors
R_{dsON}	Drain-source ON-resistance
R_{dsOFF}	Drain-source OFF-resistance
R_g	Internal generator resistance
R_l	Load resistance
$R_{IOpt class-S}$	Optimal load resistance for a CMCS PA
$R_{IOpt class-D}$	Optimal load resistance for a CMCD PA
S_{C1}	Transmission coefficient of common mode of excitation
S_{D1}	Transmission coefficient of differential mode of excitation
S_{ij}	Scattering parameters matrix
S_{ij}^M	Mixed-mode scattering parameters matrix
$u_{1,2}(t)$	Drain-source voltage
$u_l(t)$	Load voltage

$V_{1,2}$	Amplitude of a drain-source voltage
V_{cc}	Supply voltage
V_{dmax}	Maximum available drain-source voltage
y_i	Partial immittance
(y_1, \dots, z_n)	Cumulant
z_{11}	Input impedance of a two-port network
z_{12}	Transfer impedance
Z_{com}	Impedances of common mode of excitation
Z_{diff}	Impedance of differential mode of excitation
Z_{EC}	Impedance of a TEM-element of distributed end capacitance
z_i	Partial immittance
Z_{loop}	Characteristic impedance of the loop
Z_p	Shunt impedances of PSN
Z_s	Series impedances of PSN

Acronyms

$\Delta\Sigma M$	Delta-Sigma Modulator
1G	First Generation
2G	Second Generation
3G	Third Generation
3GPP	3G Partnership Project
4G	Fourth Generation
8-PSK	Octagonal Phase Shift Keying
ACPR	Adjacent Channel leakage Power Ratio
ADS	Advanced Design System (Software)
BICLF	Balanced Input CLF
BPF	Band-Pass Filter
BP-PLM	Band-Pass Pulse-Length Modulator
BTS	Base Transceiver Station
CDMA	Code Division Multiple Access

CLF	Comb-Line Filter
CMCD	Current-Mode Class-D
CMCS	Current-Mode Class-S
DT	Doubly Terminated
EER	Envelope Elimination and Restoration
EDGE	Enhanced Data rates for GSM Evolution
EM	Electromagnetic
EVM	Error Vector Magnitude
FBH	in Berlin, Germany Ferdinand-Braun-Institut Leibniz-Institut für Höchstfrequenz- technik
FDD	Frequency Division Duplex
FET	Field Effect Transistor
FPGA	Field Programmable Gate Array
GaN	Gallium Nitride
GMSK	Gaussian Minimum Shift Keying
GPRS	General Packet Radio Service
GSM	Global System for Mobile Communications
HEMT	High Electronic Mobility Transistor
HFSS	High Frequency Structural Simulator (Software)
HSPA	High-Speed Packet Access
HSPA+	Evolved High-Speed Packet Access
IAF	Fraunhofer Institute Applied Solid-State Physics in Freiburg, Germany
LPF	Low-Pass Filter
LTE	Long Term Evolution
MESFET	Metal-semiconductor FET
MIMO	Multiple Input Multiple Output
MMIC	Monolithic Microwave Integrated Circuit
OFDM	Orthogonal Frequency Division Multiplexing
PA	Power Amplifier

PAPR	Peak to Average Power Ratio
PLM	Pulse-Length Modulator
PTFE	Polytetrafluoroethylene
PSN	Pulse Shaping Network
PSD	Power Spectral Density
QAM	Quadrature Amplitude Modulation
QL Δ Σ M	Quasi Lowpass Δ Σ Modulator with Manchester encoder
QPSK	Quadrature Phase Shift Keying
RF	Radio Frequency
RMS	Root Mean Square
SNR	Signal-to-Noise Ratio
SMPA	Switched-Mode Power Amplifier
SMD	Surface Mount Device
ST	Singly Terminated
TEM-mode	Transverse ElectroMagnetic mode
TDMA	Time Division Multiple Access
TETRA	TErrestrial TRunked RAdio
UMTS	Universal Mobile Telecommunications System
VMCD	Voltage-Mode Class-D
VMCS	Voltage-Mode Class-S
W-CDMA	Wideband Code Division Multiple Access
WiMAX	Worldwide Interoperability for Microwave Access